Heat transfer in stratified flow.

Author:
Pleasance, G. E.

Publication Date:
1974

DOI:
https://doi.org/10.26190/unsworks/5252

HEAT TRANSFER IN STRATIFIED FLOW

by

G.E. Pleasance Dip.M.E., B.E.

A dissertation submitted in partial fulfilment of the requirements for the degree of Master of Engineering in the University of New South Wales

June, 1974.

I hereby certify that the work presented in this thesis is the result of original research and has not been submitted for a higher degree to any other University or Institution.

SYNOPSIS:

When water is drawn from a cooling pond, heated by some industrial process and discharged back into the pond to dissipate its heat load to the atmosphere an orderly motion is generated within the pond. This motion and the subsequent heat transfer from the surface of the pond is governed by the inlet Densimetric Froude Number, the inlet Reynolds Number, and the rate of heat transfer from the surface.

In this dissertation, a two-dimensional cooling pond has been studied. The heated water is discharged onto the surface of the pond and, after losing heat at the surface, is eventually withdrawn from the bottom of the pond. The laminar equations of motion and the boundary conditions describing the problem have been approximated using finite differences and the equations have been solved using a numerical technique. The results of this mathematical model have been compared with the results of a laboratory-scale experimental investigation of the problem. The experimental results have also been compared with those obtained from a modified form of the mathematical model proposed by Koh and Fan for surface buoyant jets.

Under steady state conditions the flow consists of a surface layer entraining fluid from below and losing heat at the surface. This layer subsides at the downstream boundary of the

pond and passes through the pond outlet. A recirculation eddy is formed under the surface flow to replenish fluid entrained into the surface layer.

ACKNOWLEDGEMENTS:

The work described in this thesis was carried out at the University of New South Wales Water Research Laboratory under a State Electricity Commission of Victoria post-graduate scholarship. I am extremely grateful to the Commission for the award of this scholarship.

To the following people, I would like to extend my sincere thanks:

Professor I.R. Wood for his guidance during the formulation of the project;

Dr. B. Jenkins and Professor G. de Vahl Davis for their supervision throughout the project;

G.D. Mallinson for his assistance with the numerical work and for his computer program which was used as a basis for the solution of the mathematical model;

the staff of the Water Research Laboratory for their assistance in building the experimental apparatus;

the Electricity Commission of New South Wales for assistance in the purchase of experimental equipment;

the Herman Central Scientific Laboratory of the State Electricity Commission of Victoria for the use of temperature measurement and recording equipment.

Finally I would like to thank my wife, Lorraine, for her encouragement and assistance during the whole of the research project.

TABLE OF CONTENTS

LIST OF TABLES:

LIST OF FIGURES:

NOMENCLATURE:

Note

1. Certain symbols which have limited use and are defined in the text are not mentioned here.

2. Distinction is made in the text where the same symbol is used to define dimensional and non-dimensional parameters.

Roman Symbols

Cf Local shear stress coefficient.

Cp Specific heat of the fluid.

d Depth of the cooling pond.

D Dimensionless depth of the cooling pond.

DT Stability ratio for numerical solution.

e Entrainment coefficient.

F Densimetric Froude Number = $\dfrac{V}{\sqrt{\frac{\Delta\rho}{\rho}\, gh}}$.

Fi Densimetric Froude Number at the inlet.

F_{cr} Critical Densimetric Froude Number.

g Acceleration due to gravity.

h Interfacial depth.

hi Inlet depth of the cooling pond.

ho Outlet depth of the cooling pond.

Hi Dimensionless inlet depth = 1.0.

Ho Dimensionless outlet depth.

Ha Overall heat transfer coefficient.

k	Coefficient of thermal conductivity.
K	Dimensionless heat transfer coefficient.
l	Length of the cooling pond.
L	Dimensionless length of the cooling pond.
M	Number of mesh points in the vertical direction.
N	Number of mesh points in the horizontal direction.
Nu	Nusselt Number $= \frac{hal}{k}$
P	Pressure.
Pr	Prandtl Number $= \frac{\rho_o C p \nu}{k}$
Re	Reynolds Number $= \frac{Vh}{\nu}$
R	Reynolds Number $= \frac{Vh}{\varepsilon}$
Ri	Richardson Number $= F^{-2}$.
T	Temperature.
Ti	Temperature at the inlet.
To	Temperature at the outlet.
Tcw & T_∞	Temperature of the heat sink.
t	Time.
u	Vertical velocity.
Ue	Entrainment velocity.
V	Mean horizontal velocity.
VH	Flow rate per unit width.
v	Horizontal velocity.

v_i Horizontal velocity at the inlet.

v_o Horizontal velocity at the outlet.

w Width of the test flume.

X Vertical co-ordinate in the transformed solution region.

x Vertical co-ordinate.

Y Horizontal co-ordinate in the transformed solution region.

y Horizontal co-ordinate.

Greek Symbols

α False transient coefficient.

β Coefficient of thermal expansion.

∇^2 Laplacian operator = $\left| \frac{\partial^2}{\partial x^2} + \frac{\partial^2}{\partial y^2} \right|$

ε Eddy viscosity.

ζ Vorticity.

θ Dimensionless temperature.

θ_i Dimensionless inlet temperature = 1.0.

θ_o Dimensionless outlet temperature.

θ_∞ Dimensionless heat sink temperature.

$\bar{\theta}$ Stability parameter for the interface.

ν Kinematic viscosity.

ρ Density.

ρ_o Reference density.

ψ Stream function.

τ Shear stress.

Subscripts

i Denotes the ith grid point in the vertical direction.

j Denotes the jth grid point in the horizontal direction.

Superscripts

n Denotes the nth time step in the progression through time.

1. INTRODUCTION AND LITERATURE SURVEY:

1.1 General

Stratified flow is defined as the flow, under the action of gravity, of a fluid over, under or through a second fluid which is of a different density. The density difference may be due to a temperature difference, dissolved compounds or particles in suspension. The present study has been confined to stratified flow in water where the density difference is due to a temperature difference caused by the disposal of low grade waste heat from industrial processes.

This particular research project was initiated as the result of the State Electricity Commission of Victoria's desire to be able to predict the temperature distribution in cooling ponds and estuaries where future power stations might dispose of waste heat. Thermal power stations require a large quantity of water to condense exhaust steam from their turbines. The waste heat, taken from the condenser, is disposed of to the atmosphere either via cooling towers or by discharging it into adjacent cooling ponds or waterways. Systems employing the latter method of disposal can be divided into two classes -

(a) The once-through system where the cooling water is taken from the ocean or a river, passed through the condensers and discharged, at a higher temperature, at a point where recycling to the inlet is unlikely.

(b) The closed system where the water is taken from a cooling pond or lake, passed through the condensers and discharged, at a higher temperature, remote from the inlet. Heat transfer to the atmosphere reduces the temperature of the water before it is recycled through the condensers.

The efficiency of the power station is partly dependent upon the temperature to which the steam is condensed by the cooling water and hence is a function of the temperature of the cooling water. It is therefore desirable to draw the coldest water available into the condensers. For the once-through system this involves ensuring that only water at ambient temperature is drawn into the power station inlet and that no short circuiting from the outlet occurs. In the closed cooling pond it involves maximising the heat transfer to the atmosphere to obtain the coolest water possible at the power station inlet for a given heat transfer area.

With the increasing demands for power, the thermal loads imposed on available cooling water resources will be increased. It therefore becomes increasingly important to be able to predict the behaviour of heated water discharged into the environment.

1.2 The Cooling Cycle

1.2.1 Terminology

Up to this point the centre of discussion has been the industrial process. To discuss the motion of water within the external environment it is necessary to define some general terms which will be adhered to for the remainder of this report -

(a) Inlet: The position where the water, heated by the industrial process, is discharged into the environment.

(b) Outlet: The point where the cool water is drawn into the industrial process.

(c) Cooling Pond: An enclosed lake or man-made pond where the only significant fluid transfer across the boundaries takes place at the inlet and outlet.

(d) Temperature Excess: The temperature difference between the heated water and the water below the interface.

(e) Heat Transfer Region: The region of the receiving waters where the temperature excess is reduced due to heat transfer to the atmosphere.

(f) Interface: The dividing line, normally taken as the position of maximum density gradient, between the buoyant and ambient fluid.

(g) Surface Flow: The fluid flow above the interface.

1.2.2 The Inlet

Heated water can either be discharged onto the surface of the receiving waters or discharged below the surface. Since water has a positive coefficient of thermal expansion, warm water tends to float on the surface of the receiving waters. If a submerged inlet is used, the heated water tends to rise towards the surface and in doing so mixes with the surrounding water, reducing its temperature excess. Alternatively, if the heated water is discharged at the surface it is possible to design an inlet structure such that minimal mixing occurs between the heated water and its surroundings. Under these conditions, the temperature excess will be greater than if mixing had occurred. This immediately suggests two design alternatives. With a submerged inlet, the temperature of the discharged water will be quickly reduced due to mixing. However, when the buoyant plume reaches the surface, the temperature difference between it and the atmosphere will also be decreased thus reducing the rate of heat transfer per unit area to the atmosphere. Hence a larger surface area will be required to dissipate the same heat input than would be required with a surface discharge scheme and the consequent higher heat transfer per unit area.

1.2.3 The Heat Transfer Region

Away from the inlet the buoyant plume spreads over the surface of the lake and loses heat to the atmosphere. The prediction of the temperature distribution in this region is dependent on a full knowledge of the past history of the fluid and the controls which govern its path. Wilkinson(23) found that the motion of a buoyant fluid discharged onto the surface of another was dependent on the downstream controls. In his experiments, he used an inverted broad crested weir as the downstream control and found that the position of this weir governed the conditions at the inlet, and hence governed the reduction of temperature excess which occurred in the inlet region. Koh and Fan(13) conducted a theoretical examination of a two-dimensional buoyant jet and found that both the heat transfer and the interfacial shear stress controlled the inlet flow conditions. Hence the inlet region and the heat transfer region are mutually dependent on one another.

The predominant mechanisms of heat transfer to the atmosphere are radiation, convection and evaporation. These are all a function of the atmospheric conditions which vary from day to day.

Evaporative water leaving the lake surface increases the vapour content of the air immediately above the water surface. Under certain conditions this air can become saturated preventing further evaporation. Air movement across the water surface scours away this saturated layer, bringing air of lower vapour content to replace it and at the same time reducing the thermal boundary layer thus also aiding convective heat transfer. Wind also imposes a shear stress on the water surface which, although small, can be of the same order of magnitude as the forces driving the plume. While conducting radioactive tracer tests on a cooling pond at Maitland, N.S.W., Ellis et. al.(6) found that winds with velocities of between 1 and 4 m/s blowing towards the inlet completely stopped the forward motion

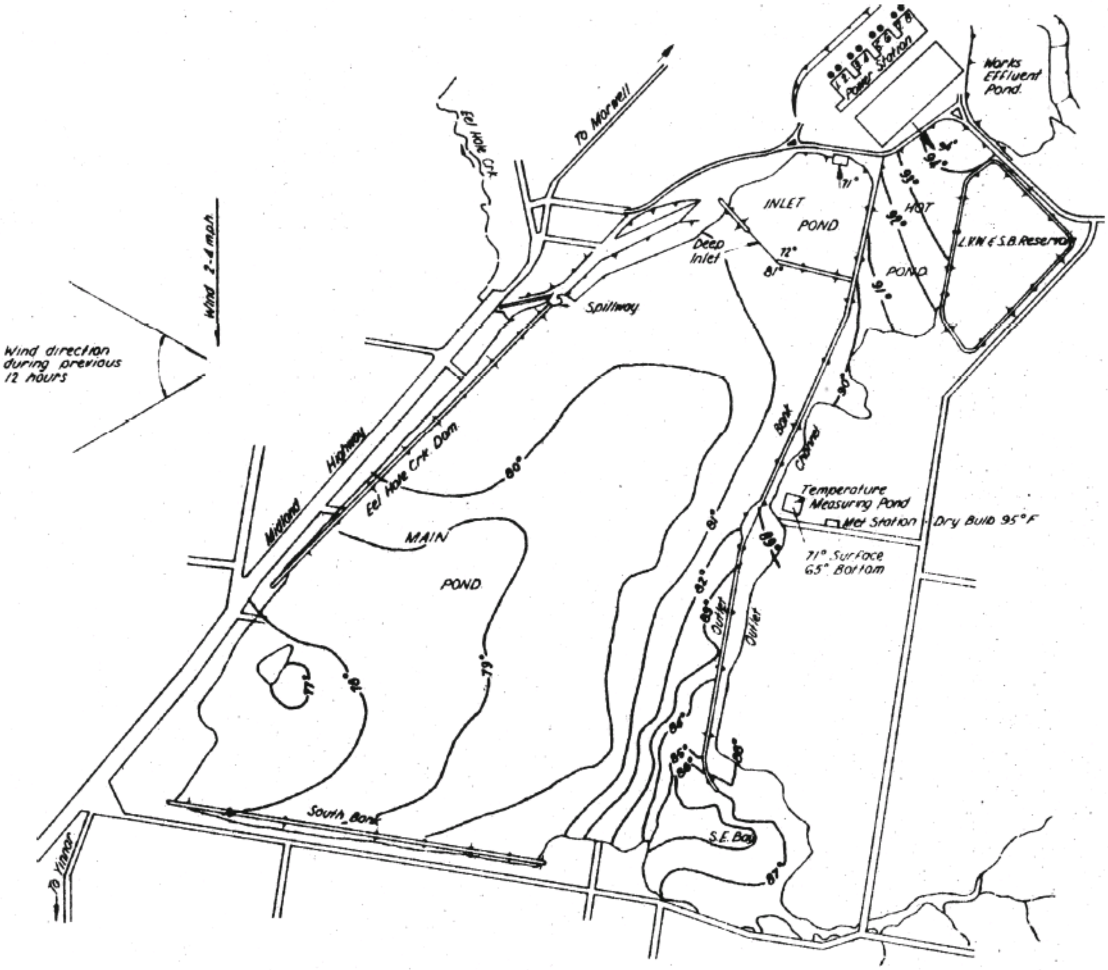

Figure 1.1 Surface temperature (^{o}F) survey at Hazelwood Power Station (Victoria) cooling pond (reprint from reference 21).

of the plume. Wind stresses on the water surface can therefore influence the motion of a buoyant plume and should be considered in the design of cooling systems.

1.2.4 The Outlet

Two types of outlet can be employed. In the open system, where adequate supplies of ambient-temperature water are available, the outlet can be directly connected to the pumping station for supply to the heat source. Where recycling of hot water to the inlet is likely, or in the closed circuit pond, advantage is taken of the stratification and a deep outlet is employed to selectively withdraw the colder water from below the interface. Figure 1.1 shows such a deep outlet employed in a closed circuit type cooling pond at Hazelwood Power Station (Victoria) during conditions of adverse wind direction. The submerged outlet prevents the hot surface water adjacent to the outlet retaining wall,from entering the recirculation pumps and draws off the colder sub-surface water instead.

1.3 Definition of the Problem to be Studied

In this dissertation it is proposed to study the closed circuit cooling pond. Heat transfer away from the surface is taken into account, and the heated water is assumed to be discharged onto the the surface of the cooling pond and withdrawn from a deep inlet structure. A further simplification is made by considering the cooling pond to be two-dimensional in the vertical and horizontal senses as shown in Figure 1.2.

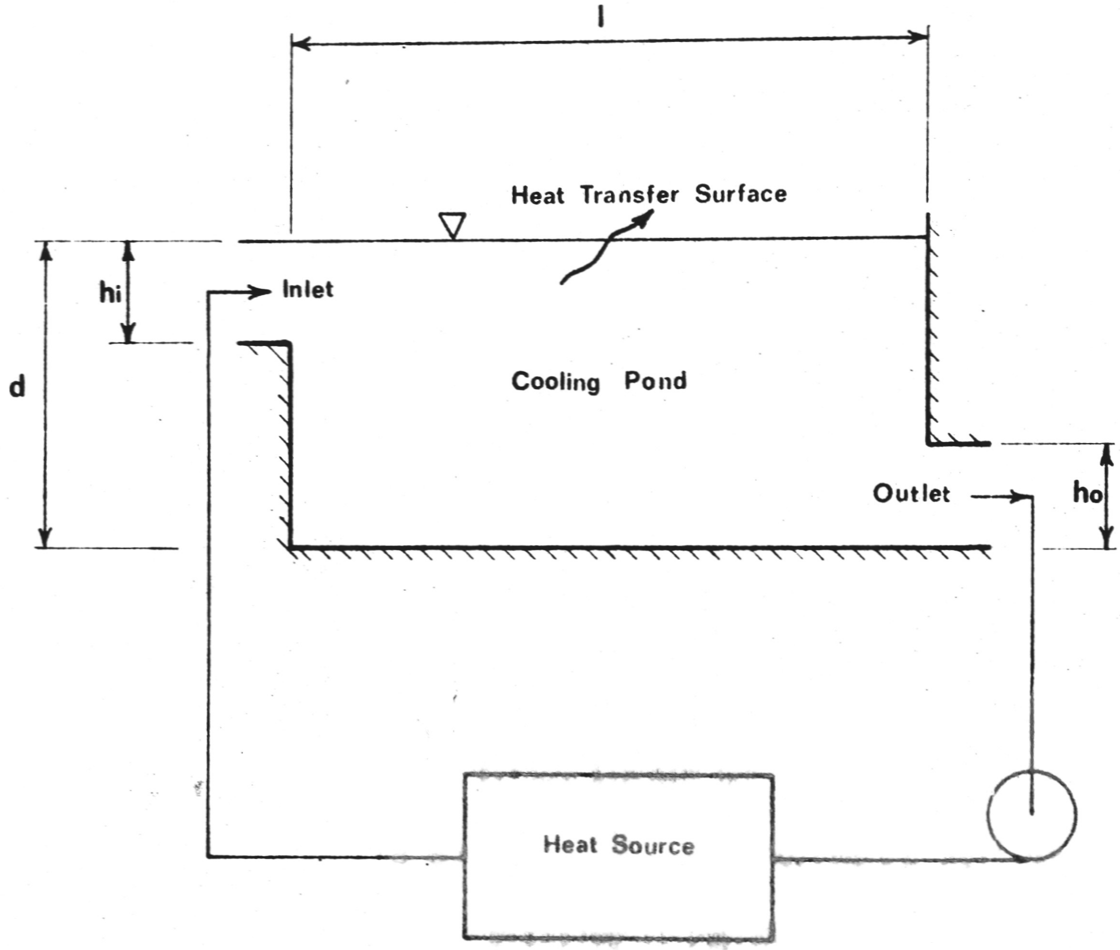

ELEVATION

Figure 1.2 Two-dimensional cooling pond.

1.4 Literature Review

An extensive review of the literature pertaining to stratified flow has been compiled by Jenkins(11). Hence, the following literature review has been confined to that concerning surface buoyant jets.

1.4.1 General Properties of Stratified Flow

Flow of a less-dense fluid over a denser fluid is characterised by a density change at the interface. In the ideal flow the interface is the position of the density discontinuity. In the real fluid the property causing the density difference is diffused through the fluid resulting in a density gradient across the interface. Hence the interfacial depth is defined as the distance from some datum (in this case the water surface) to the point of maximum density gradient. A parameter often used to describe the condition of the interface is

$$\overline{\theta} = F^2 Re \tag{1.1}$$

where F is the local Densimetric Froude Number, and

Re is the local Reynolds Number.

$\overline{\theta}$ can be regarded as a stability parameter for the interface, the higher the value of $\overline{\theta}$ the more unstable or disturbed is the interface. Sherenkov et. al.(19) classified the form of the interface in terms of $\overline{\theta}$ as follows:

$\overline{\theta} \lesssim 150$ Stable interface; viscous type flow with planar boundary or division at the interface.

$150 < \overline{\theta} \lesssim 500$ Stabilised wave flow (long regular waves).

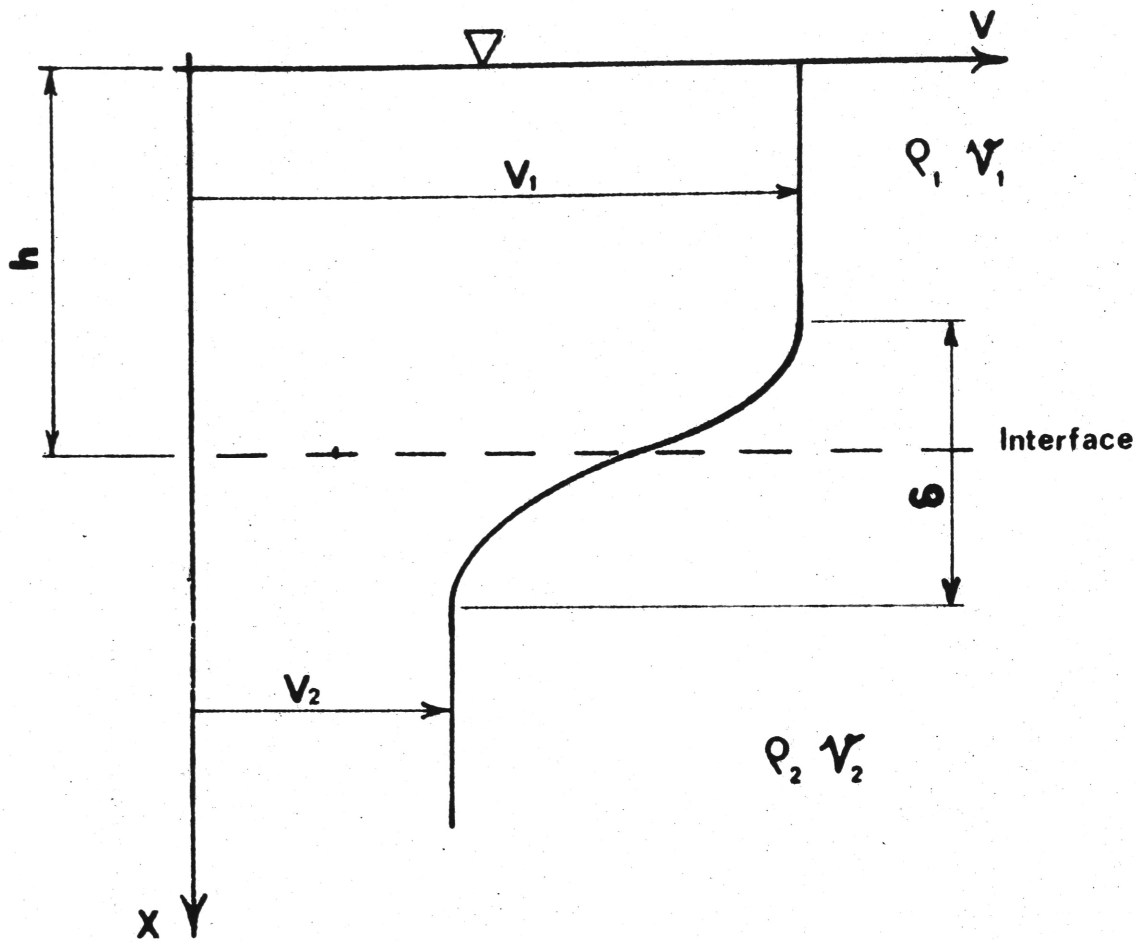

<u>Figure 1.3</u> Definition sketch for the stability parameter as defined by Sherenkov et al (19).

$500 < \bar{\theta} \leq 800$	Unstable waves.
$800 < \bar{\theta} \leq 1650$	Disruptive waves; i.e. internal waves breaking at the interface.
$1650 < \bar{\theta}$	Waveless mixing between the layers and development towards fully turbulent flow.

$\bar{\theta}$ was based on a characteristic boundary layer thickness δ as defined in Figure 1.3. The Densimetric Froude Number and the Reynolds Number were obtained using the mean fluid properties and were defined as

$$F_\delta = \frac{V_1 - V_2}{\sqrt{\frac{(\rho_2 - \rho_1)}{\rho_1} g\delta}}$$

$$Re_\delta = (V_1 - V_2)\delta / \frac{(\rho_1 V_1 + \rho_2 V_2)}{\rho_1 + \rho_2}$$

Other workers in this field have used various forms of the stability parameter to characterise the entrainment of ambient fluid into the flowing layer. In the case being considered here of a less-dense fluid flowing over a denser fluid, entrainment will be from the denser fluid to the surface layer causing a reduction in the temperature of the surface layer and a corresponding increase in the mass flow.

Ellison and Turner(7) defined an entrainment coefficient as

$$e = \frac{1}{h}\frac{d}{dy}(Vh)$$

$$= \frac{Ue}{V} \qquad (1.2)$$

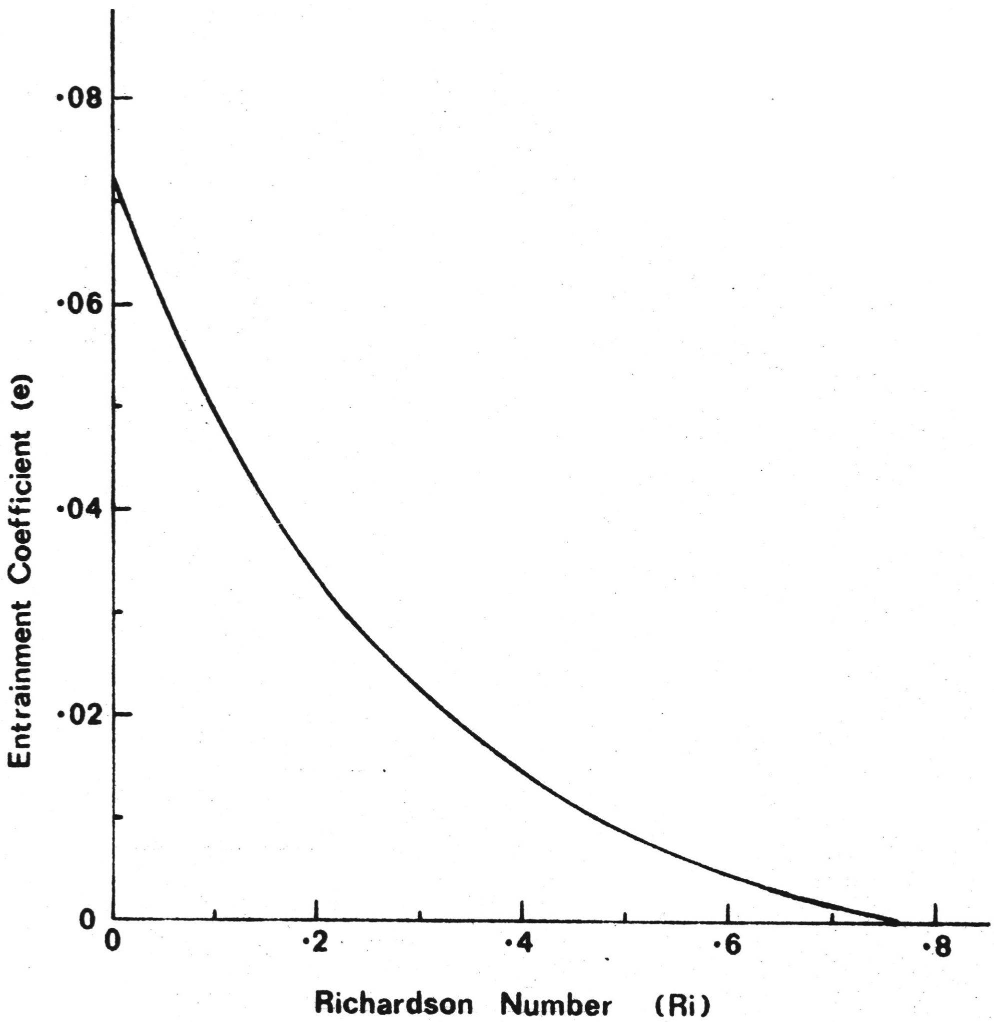

Figure 1.4 The entrainment coefficient (e) as a function of the Richardson Number (Ri) - Ellison & Turner (7).

where Ue is the velocity of inflow into the surface layer, and reasoned that the entrainment coefficient was a function of the local Richardson Number* (Ri) provided that the Reynolds Number was high enough for viscous effects to be negligible. They found that for Richardson Numbers above 0.83 the entrainment of ambient fluid across the interface was negligible. Their experimental results for the relationship between the entrainment coefficient and the Richardson Number are shown in Figure 1.4 and may be approximated by the relationship

$$e = 0.075\left[\frac{2}{1+Ri/0.85} - 1\right]^{1.75} \qquad (1.3)$$

or alternatively

$$e = 0.075\ \exp(-5\ Ri).$$

Keulegan (12B) found that the critical velocity for mixing depended on whether the surface flow was laminar or turbulent. For turbulent flow he found that the critical velocity above which mixing would occur was given by the relationship

$$\left[\frac{1}{F^2 R_e}\right]^{1/3} = 0.178 \qquad (1.4)$$

This relationship was later confirmed by Lofquist(15). Lofquist's experimental results for Reynold Numbers greater than 1000 confirmed that the entrainment coefficient was dependent on the

* *The Richardson Number is the reciprocal of the Densimetric Froude Number squared* $Ri = (F)^{-2}$.

Densimetric Froude Number but he found that entrainment can exist down to very low Densimetric Froude Numbers.

The discontinuity in velocity at the interface implies that shear stresses act in opposition to the surface flow. The shear stress (τ) acting on a fluid can be related to the local Reynolds Number by the relationship

$$\tau = \frac{1}{2}\, Cf\, \rho U^2 \qquad \text{and} \tag{1.5}$$

$$Cf = \text{const} \times (Re_y)^n$$

where Cf is the local shear stress coefficient,

n is a constant, and

$$Re_y = \frac{Vy}{\nu} \, .$$

For laminar flow over a flat plate the characteristic length for defining the Reynolds Number is taken as the distance from the leading edge and the solution as given by Blasius(18) for the local shear stress coefficient is

$$Cf_b = \frac{\tau}{\frac{1}{2}\rho U^2} = 1.33\ (Re_y)^{-\frac{1}{2}} \tag{1.6}$$

Bata(2) carried out a similar analysis to that of Blasius to determine the interfacial shear stress coefficient and found that the interface acted as a reverse boundary layer in which the local shear stress coefficient was given by

$$Cf_i = \frac{\tau i}{\rho Vi^2} = 0.44\ (Re_y)^{-\frac{1}{2}} \tag{1.7}$$

where τi is the interfacial shear stress, and

Vi is the interfacial velocity.

Keulegan (12A) found, using the Von Karman integral approach, that the interfacial shear stress depended upon the ratio $\rho_1 V_1/\rho_2 V_2$ where the subscripts 1 and 2 refer to the fluids above and below the interface respectively. For values of this ratio approximately equal to unity, he found that the interfacial shear stress coefficient was given by

$$Cf_i = \frac{\tau i}{\frac{1}{2}\rho V^2} = 0.39\ (Re_y)^{-\frac{1}{2}} \qquad (1.8)$$

and the interfacial velocity was

$$Vi = 0.59\ V$$

This is in good agreement with Bata's results as equation (1.7), when put into the same terminology, gives

$$Cf_i = 0.398\ (Re_y)^{-\frac{1}{2}} \qquad (1.9)$$

The interfacial shear stress is also affected by the presence of any near boundary or externally applied shear stress (e.g. wind over the surface). Ippen and Harleman(10) found that for a fluid flowing under a less-dense one and over a solid boundary, the total shear stress coefficient was given by

$$Cf = (0.114\ Re)^{-1} \qquad (1.10)$$

where $Re = \frac{Vh}{\nu}$, and

h = depth from the interface to the solid boundary.

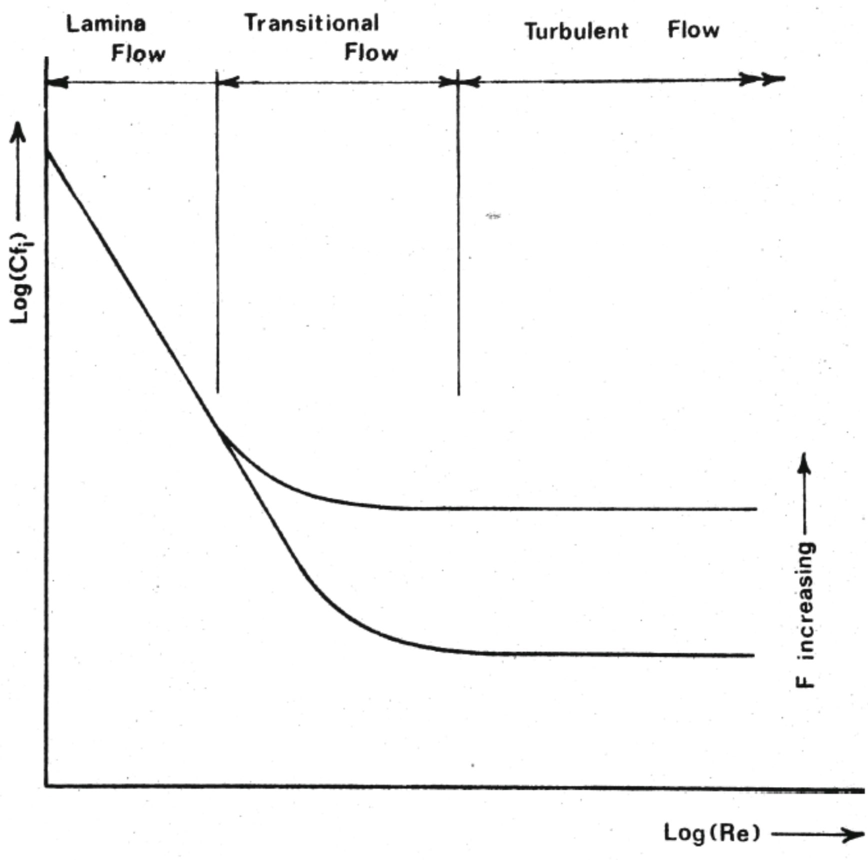

Figure 1.5 The form of the relationship between the interfacial shear stress coefficient and the Reynolds Number - Abraham & Eysink (1).

This formulation is more useful for practical problems as it gives the local shear stress coefficient in terms of the local depth.

For non-buoyant flows, as the Reynolds Number of the flow increases, the shear stress coefficient becomes independent of the Reynolds Number and becomes dependent upon the relative roughness of the external boundaries. An effect similar to that of boundary roughness has been observed in the presence of waves on the interface at higher values of the stability parameter described earlier. Abraham and Eysink(1) reasoned that the presence of these interfacial waves has the same effect as the roughness in the normal Moody diagram.

An increase in the density difference across the interface has a stabilising effect on the interface and tends to damp out interfacial waves, reducing the roughness and hence reducing the shear stress coefficient. They found that the shear stress coefficient became independent of the Reynolds Number for turbulent flows and was only dependent on the Densimetric Froude Number. This general concept is shown in Figure 1.5. Abraham and Eysink's experimental results supported this concept and they concluded that the interfacial shear stress coefficient was independent of the Reynolds Number for turbulent flow.

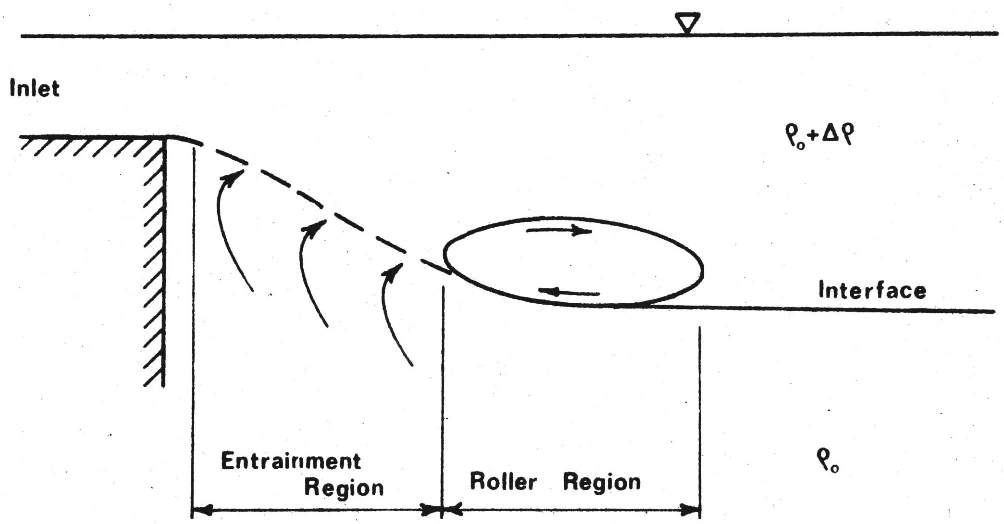

Figure 1.6 Classification of the Internal Hydraulic Jump - Wilkinson (23).

1.4.2 Flow Conditions Near the Inlet

Stratified flow, like open channel flow, can be subcritical or supercritical. It is not uncommon for the flow at the cooling pond inlet to be supercritical (i.e. to have a Densimetric Froude Number greater than unity). Wilkinson(23) showed that under certain conditions, supercritical density flows were unstable at the inlet and changed to subcritical flow by means of a density jump (referred to here as an internal hydraulic jump). This, he found, was usually associated with a decrease in density due to part of the upstream energy being dissipated in entraining ambient fluid. Wilkinson separated the density jump into two parts, an entrainment region and the roller region (Figure 1.6) and he classified the flow according to the existence of these regions as follows:

(a) Fully entraining jump ..... no roller region.

(b) Partially entraining jump ..... roller and entraining region both present.

(c) Flooded jump ..... no entrainment region.

Wilkinson found that the existence of these regions depended upon the downstream control. In his experiments he used an inverted broad crested weir as the downstream control but reasoned that heat transfer away from the surface and interfacial shear can also act as the control.

Koh and Fan(13) formulated a mathematical model to describe the temperature distribution and depth of flow for the two dimensional surface buoyant jet. The model takes into account heat transfer away from the surface, entrainment of ambient fluid, and the interfacial shear. Like Wilkinson, they found that the flow conditions at the inlet could be classified in three ways, which they described as

(a) Inundation (flooded jump).

(b) Internal hydraulic jump.

(c) Jet-like (maximum entraining jump).

The type of solution applicable to a particular situation depended upon

(a) the inlet Densimetric Froude Number,

(b) the non-dimensional heat transfer coefficient, and

(c) the Reynolds Number, which determines the interfacial shear stress,

and these parameters acted as the downstream control referred to by Wilkinson.

Stolzenback and Harleman(20) present a mathematical model for the three dimensional surface buoyant jet. It incorporates the heat transfer from the surface, vertical entrainment from below, and horizontal entrainment into the plume as it spreads in the lateral direction. They consider the solution to be that of a normal surface jet with buoyancy forces superimposed on the flow. No evidence of an internal hydraulic jump was found in their solution but experimental verification of their model indicated that it was better suited to the high Densimetric Froude Number condition corresponding to the 'jet-like' solution described by Koh and Fan.

For subcritical flows at the inlet ($Fi < 1$) it has been found that a cold water wedge penetrates into the inlet resulting in a reduction of the interfacial depth. Harleman(9) found the reduced interfacial depth was that which gave $F = 1$ at the inlet.

1.4.3 The Overall Cooling Pond

A steady state solution cannot be found to the cooling pond problem without considering heat transfer away from the surface. For the closed cooling pond (Figure 1.2) the hotter fluid from the inlet will flow along the surface, losing heat to the surface boundary until it reaches the downstream vertical boundary where the fluid must subside. Hence the temperature of the fluid at the downstream vertical boundary will be the ambient or minimum pond temperature. It is this temperature which determines the reduction in the surface layer temperature when ambient fluid is entrained into the surface flow.

The flow pattern below the interface for a submerged outlet has not been reported in the literature to the author's knowledge.

In their experiments with the outlet at the surface, Lean and Willock(14) reported a slight backflow to replenish the fluid entrained at the inlet. A "snaking" flow pattern has been observed by the author during the establishment of steady-state conditions (this flow pattern is discussed later in this report). Under these conditions, the entire surface flow moves back under the interface towards the inlet. Upon reaching the solid boundary below the the interface, it again reverses direction. Flow to the outlet occurs as a series of layers, alternate layers flowing in opposite directions. Such a flow pattern will increase the interfacial shear stress and affect the stability of the interface.

As the surface flow approaches the downstream boundary so the density difference across the interface decreases and consequently the Densimetric Froude Number, defined as

$$F = \frac{V}{\sqrt{\frac{\Delta\rho}{\rho} gh}} \qquad (1.11)$$

would tend to increase unless the decrease in $\Delta\rho$ is compensated for by an increase in depth and a corresponding decrease in velocity. For the two dimensional case the velocity can be represented by

$$V = \frac{Q'}{h}$$

where Q' is the volume flow rate/unit width, and equation (1.11) becomes

$$F = \frac{Q'}{\sqrt{\frac{\Delta\rho}{\rho} gh^3}}$$

If the inlet is inundated or an internal hydraulic jump forms, the interfacial depth must increase to compensate for the decrease in density difference for the surface flow to remain subcritical.

1.5 Aims of this Study

The aims of the work presented in this dissertation were to investigate the overall flow and temperature fields in the two-dimensional cooling pond under steady state operating conditions. Steady state conditions were achieved in both the theoretical and experimental investigations by including the heat transfer away from the surface of the pond.

(a) Theoretical Investigation

The laminar equations of motion and the appropriate boundary conditions for the two-dimensional cooling pond are formulated in Chapter 2 and a numerical technique (Chapter 3) has been used to solve these equations. The results of this model are presented in Chapter 4.

(b) Experimental Investigation

The experimental apparatus used is described in Chapter 5 and the results of the experimental investigation are given in Chapter 6.

The mathematical model of the two-dimensional surface buoyant jet proposed by Koh and Fan has been modified to account for the finite length of the cooling pond and the results of this modified model, using the values of the entrainment coefficient obtained in the experimental investigation, are compared with the experimental results in Chapter 7.

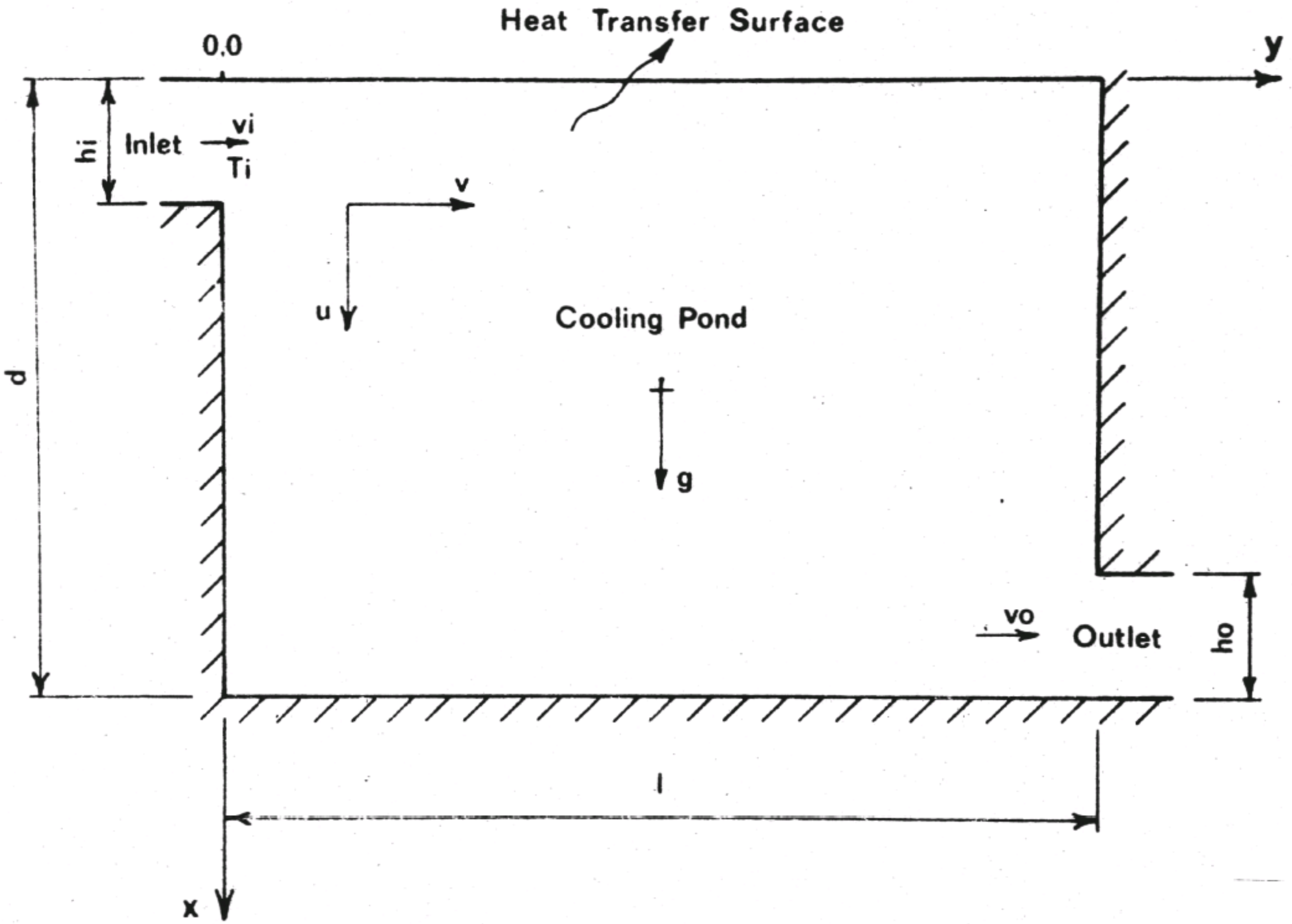

Figure 2.1 Definition sketch of the two-dimensional cooling pond.

2. THE COOLING POND PROBLEM AND GOVERNING EQUATIONS:

2.1 Formulation of the Mathematical Model

The problem to be modelled (Figure 2.1) is a two-dimensional cooling pond, the space dimensions being depth (d) and length (l). The inlet to the pond is situated at the surface and is of depth hi. The outlet, of depth ho, is in the diagonally opposite corner. These are the only regions where mass transfer occurs across the boundary. Heat is convected into the model at the inlet and lost by conduction away from the free surface (x = o) and by convection from the outlet, all other boundaries being adiabatic.

The aim of the model is to produce a mathematical representation of the overall flow pattern imposed upon an otherwise quiesent system, by the introduction of a buoyant plume at the inlet. For most practical cooling ponds the flow at the inlet, and in the subsequent plume, is turbulent and as such can not be mathematically modelled without certain assumptions regarding the characteristics of this turbulence. The experimental investigation showed that the flow in the buoyant plume is influenced by the convection of heat from the body of the plume to the top surface, resulting in a uniform velocity and temperature distribution across the surface layer, and a discontinuity at the interface with the underlying velocity distribution resembling that of laminar flow (see Figure 2.2).

The turbulent flow could be modelled by assuming that the fluid was laminar and introducing false diffusion into the governing

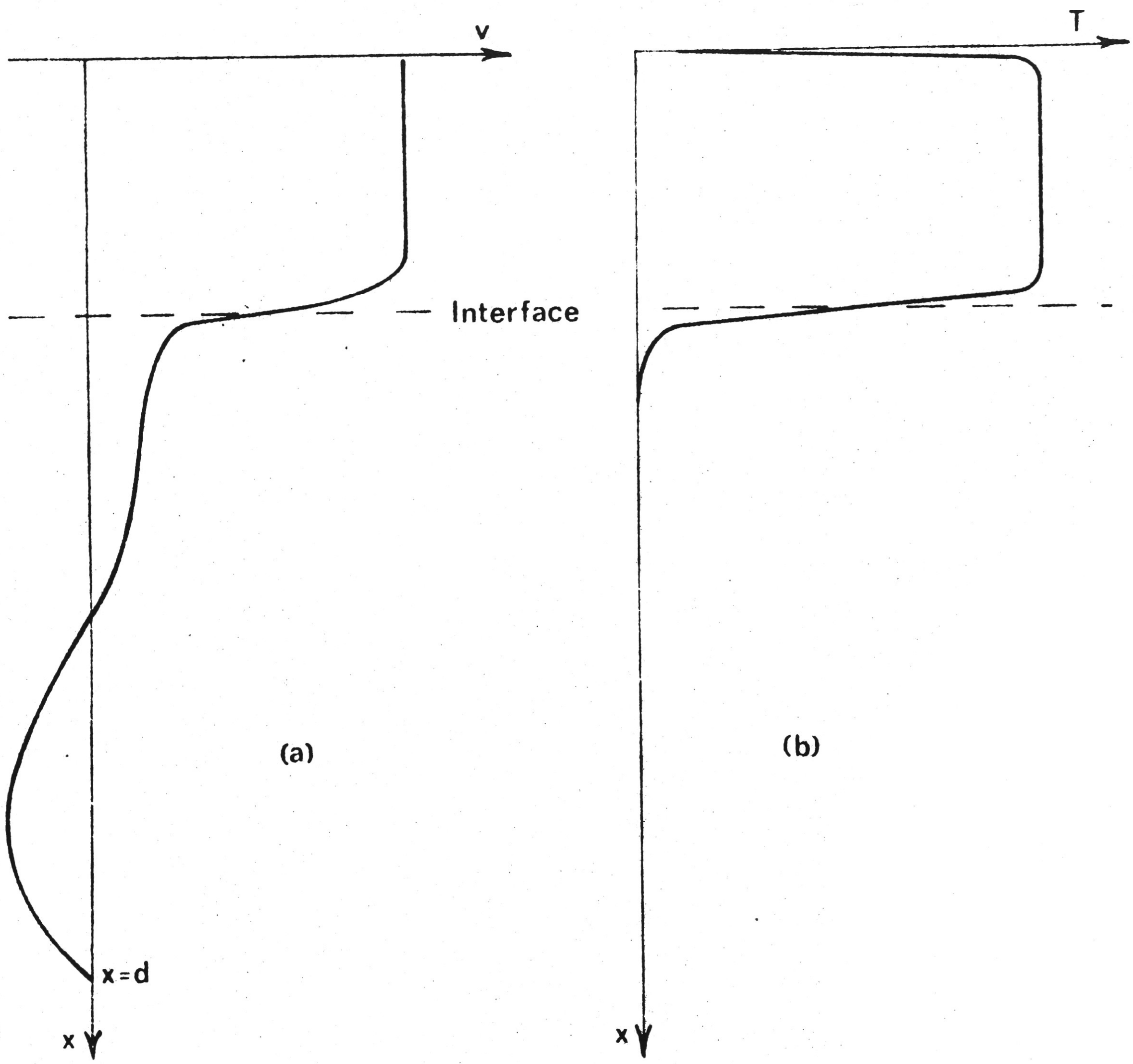

Figure 2.2 Typical vertical profiles of (a) velocity and (b) temperature from the experimental investigation.

equations. At best this is a first order approximation to the physical process and in this case becomes less appropriate because of the discontinuity in velocity and temperature at the interface. The mathematical model proposed by Koh and Fan(13) overcomes this problem by assuming the form of the temperature and velocity distribution within the surface layer and integrating the equations of motion in the vertical plane to obtain a system of one dimensional equations describing the flow. However this approach does not give any information on the resultant flow below the interface. It is therefore proposed to study the laminar equations of motion in an attempt to obtain a better understanding of the overall flow phenomena.

In the formation of the governing equations the following assumptions were made:

(a) The variations in temperatures throughout the model are sufficiently small that the corresponding changes in density have negligible effect on the inertia forces, and only become important when associated with the gravity vector. This is commonly referred to as the Boussinesq assumption.

(b) No internal energy is generated within the model.

(c) Heat generation due to friction is negligible.

(d) The free surface elevation remains constant.

(e) Evaporation from the free surface is negligible.

(f) Surface tension forces are negligible.

(g) The fluid is incompressible.

2.2 The Governing Equations

The steady state equations describing the fluid motion are those expressing conservation of mass, momentum and energy and may be expressed for the two dimensional cartesian co-ordinate scheme defined in Figure 2.1 as -

$$\frac{\partial u}{\partial x} + \frac{\partial v}{\partial y} = 0 \qquad (2.1)$$

$$u\frac{\partial u}{\partial x} + v\frac{\partial u}{\partial y} = \frac{Fx}{\rho_o} - \frac{1}{\rho_o}\frac{\partial P}{\partial x} + \nu\nabla^2 u \qquad (2.2)$$

$$u\frac{\partial v}{\partial x} + v\frac{\partial v}{\partial y} = -\frac{1}{\rho_o}\frac{\partial P}{\partial y} + \nu\nabla^2 v \qquad (2.3)$$

$$u\frac{\partial T}{\partial x} + v\frac{\partial T}{\partial y} = \frac{k}{\rho_o Cp}\nabla^2 T \qquad (2.4)$$

where u and v are the velocity components in the x and y directions respectively,

T is the fluid temperature,

P the pressure,

ρ_o the density of the fluid at the outlet, and

ν, k, and Cp are the kinematic viscosity, thermal conductivity, and specific heat of the fluid respectively.

The operator ∇^2 is defined by -

$$\nabla^2 = \frac{\partial^2}{\partial x^2} + \frac{\partial^2}{\partial y^2}$$

Fx is the body force acting on the fluid due to gravity and can be expressed as -

$$Fx = \rho g \tag{2.5}$$

where $\rho = \rho_o - \Delta\rho$ ($\Delta\rho$ being the density difference), and

g is the acceleration due to gravity.

The pressure term may be represented as -

$$P = Ps + Pd$$

where Pd is the dynamic pressure, and

Ps is the hydrostatic pressure given by $Ps = \rho_o gx$

hence,

$$\frac{\partial P}{\partial x} = \rho_o g + \frac{\partial Pd}{\partial x} \tag{2.6}$$

The momentum equations (2.2) and (2.3) therefore become

$$u\frac{\partial u}{\partial x} + v\frac{\partial u}{\partial y} = -\frac{\Delta\rho g}{\rho_o} - \frac{1}{\rho_o}\frac{\partial Pd}{\partial x} + \nu\nabla^2 u \tag{2.7}$$

$$u\frac{\partial v}{\partial x} + v\frac{\partial v}{\partial y} = -\frac{1}{\rho_o}\frac{\partial Pd}{\partial y} + \nu\nabla^2 v \tag{2.8}$$

Assuming that the density variation is small and is only a function of temperature, the density ρ may be expressed as -

$$\rho = \rho_o - \Delta\rho$$

$$= \rho_o - \left.\frac{\partial\rho}{\partial T}\right|_o (T - To)$$

therefore

$$\frac{\rho_o - \rho}{\rho_o} = \frac{1}{\rho_o}\frac{\partial\rho}{\partial T}(T - To)$$

$$\therefore \quad \frac{\Delta\rho}{\rho_o} = -\beta\,(T - To) \qquad (2.9)$$

where $\beta = -\frac{1}{\rho_o}\frac{\partial\rho}{\partial T}$ is the coefficient of thermal expansion of the liquid and is assumed to be constant over the range of temperatures encountered in the model.

Hence, the vertical momentum equation (2.7) becomes

$$u\frac{\partial u}{\partial x} + v\frac{\partial u}{\partial y} = \beta g\Delta T - \frac{1}{\rho_o}\frac{\partial Pd}{\partial x} + \nu\nabla^2 u \qquad (2.10)$$

Differentiating equations (2.8) with respect to x and (2.10) with respect to y, subtracting to eliminate the pressure term and invoking the continuity equation (2.1) results in the vorticity transport equation (2.11).

$$u\frac{\partial\zeta}{\partial x} + v\frac{\partial\zeta}{\partial y} = g\beta\frac{\partial\Delta T}{\partial y} + \nu\nabla^2\zeta \qquad (2.11)$$

where ζ is the vorticity defined by

$$\zeta = \frac{\partial v}{\partial x} - \frac{\partial u}{\partial y} \qquad (2.12)$$

Expressing the velocity components in terms of the stream function ψ so that the continuity equation is satisfied gives

$$u = \frac{\partial\psi}{\partial x} \quad \text{and} \qquad (2.13)$$

$$v = -\frac{\partial\psi}{\partial y}$$

The vorticity can then be expressed in terms of the stream function as

$$\zeta = -\nabla^2\psi \tag{2.14}$$

Hence, the governing steady state equations become

$$u \frac{\partial\zeta}{\partial x} + v \frac{\partial\zeta}{\partial y} = g\beta \frac{\partial(\Delta T)}{\partial y} + \nu\nabla^2\zeta \tag{2.15}$$

$$u \frac{\partial T}{\partial x} + v \frac{\partial T}{\partial y} = \frac{k}{\rho_o Cp} \nabla^2 T \tag{2.16}$$

$$\zeta = -\nabla^2\psi \tag{2.17}$$

2.3 Non-Dimensionalisation of the Equations

The governing equations can be non-dimensionalised in terms of the mean inlet velocity (Vi), the inlet depth (hi) and the temperature excess at the inlet (Ti - To). Usually stratified flows of this nature are characterised by the density difference between the inlet and the ambient fluid below the interface which implies that the temperature of the ambient fluid should be selected as the reference temperature. However, as mentioned in Chapter 1, the ambient fluid temperature depends upon the previous history of the fluid in the cooling pond and hence is not known prior to the solution. This can be shown from an overall heat balance on the pond. For steady state conditions

the rate of heat inflow	=	rate of heat outflow	+	rate of heat loss from the surface

Assuming that heat is only convected across the inlet and outlet boundaries this can be expressed as -

$$\dot{M}Cp\ (Ti - To) = \int_0^{l} ha\ (Tu - Ta)\ dy$$

where $\dot{M}$ is the mass flow rate per unit width,

ha is the overall heat transfer coefficient between the fluid surface and the ambient air,

Tu is the surface temperature, and

Ta is the ambient air temperature.

Selecting the outlet temperature (To) as the reference temperature requires that the surface temperature be chosen to satisfy the above equation. This becomes difficult as the distribution of the surface temperature depends on the solution within the cooling pond. It is therefore more convenient to choose the ambient air temperature as the reference temperature.

The primary non-dimensional terms are defined as

$$u^* = \frac{u}{Vi} \qquad v^* = \frac{v}{Vi}$$

$$x^* = \frac{x}{hi} \qquad y^* = \frac{y}{hi}$$

$$\theta^* = \frac{(T - Ta)}{(Ti - Ta)}$$

where the starred quantities represent the non-dimensional variable. The non-dimensional stream function (ψ^*) and vorticity (ζ^*) expressed in terms of these primary variables using equations (2.13) and (2.12) are

$$\psi^* = \frac{1}{Vihi}\,\psi$$

$$\zeta^* = \frac{hi}{Vi}\,\zeta$$

Applying these non-dimensional quantities to equations (2.15) to (2.17) they reduce to

$$u^* \frac{\partial \zeta^*}{\partial x^*} + v^* \frac{\partial \zeta^*}{\partial y^*} = hig\,\frac{\beta(Ti - Ta)}{Vi^2}\,\frac{\partial \theta^*}{\partial y^*} + \frac{\nu}{Vihi}\,\nabla^2 \zeta^*$$

$$u^* \frac{\partial \theta^*}{\partial x^*} + v^* \frac{\partial \theta^*}{\partial y^*} = \frac{k}{\rho_o CpVihi}\,\nabla^2 \theta^*$$

$$\zeta^* = -\nabla^2 \psi^*$$

The non-dimensional coefficients of these equations can be expressed in terms of familiar non-dimensional numbers

$$\frac{Vihi}{\nu} = Re$$

where Re is the Reynolds Number based on the inlet depth.

Utilising equation (2.9) the coefficient of $\frac{\partial \theta^*}{\partial y^*}$ reduces to

$$\frac{Vi^2}{g\beta\,(Ti - Ta)\,hi} = \frac{Vi^2}{g\,\frac{\Delta\rho}{\rho}\,hi}$$

$$= Fi^2$$

where Fi is the ideal Densimetric Froude Number and identical to the Densimetric Froude Number at the inlet should the fluid cool to ambient air temperature, i.e. Ta = To. The remaining dimensionless coefficients reduce to

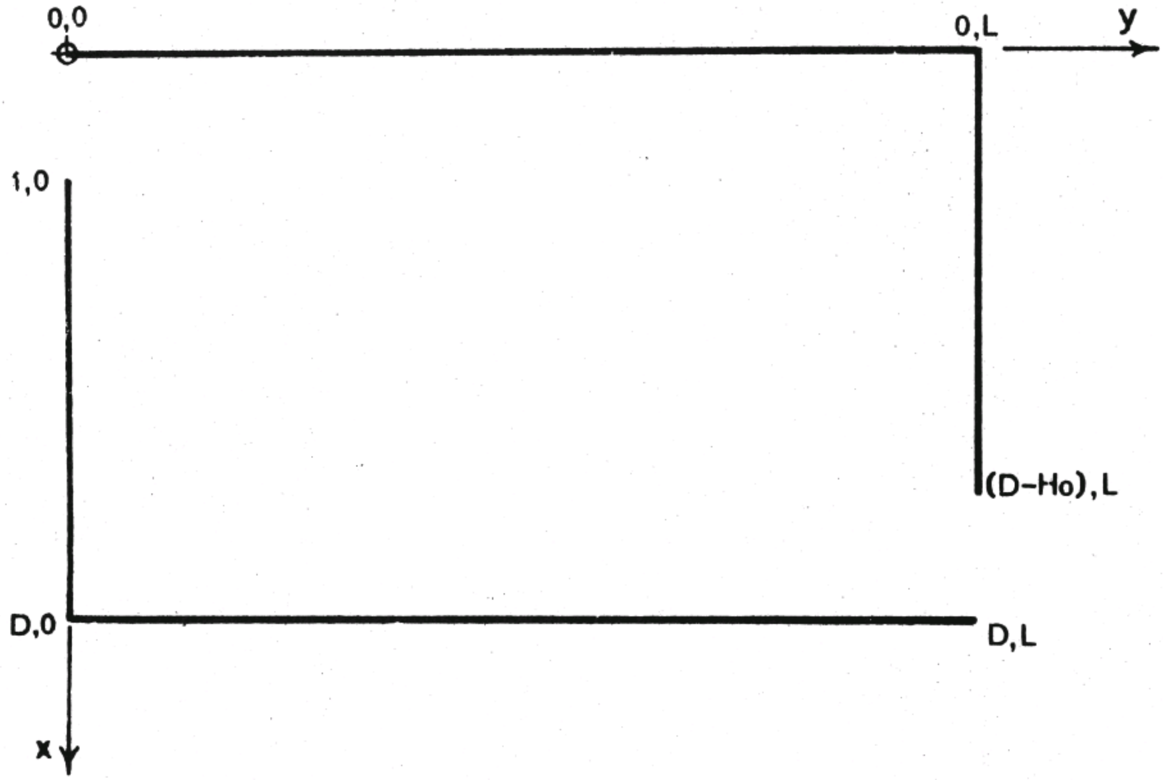

Figure 2.3 Dimensionless cooling pond geometry.

$$\frac{\rho_o CpVihi}{k} = \frac{\rho_o Cp\nu}{k} \cdot \frac{Vihi}{\nu}$$

$$= PrRe$$

where Pr is the Prandtl Number.

The geometric configuration defined in Figure 2.1 can be non-dimensionalised in terms of the inlet depth as follows:

$D = \dfrac{d}{hi}$ the non-dimensional depth,

$L = \dfrac{l}{hi}$ the non-dimensional length,

$Hi = 1.0$ the inlet depth,

$Ho = \dfrac{ho}{hi}$ the outlet depth,

and are shown diagramatically in Figure 2.3. The non-dimensional steady state equations (dropping the starred superscript) therefore are

$$u \frac{\partial \zeta}{\partial x} + v \frac{\partial \zeta}{\partial y} = \frac{1}{Fi^2} \frac{\partial \theta}{\partial y} + \frac{1}{Re} \nabla^2 \zeta \tag{2.18}$$

$$u \frac{\partial \theta}{\partial x} + v \frac{\partial \theta}{\partial y} = \frac{1}{RePr} \nabla^2 \theta \tag{2.19}$$

$$\zeta = -\nabla^2 \psi \tag{2.20}$$

where $u = \dfrac{\partial \psi}{\partial y}$, and

$v = - \dfrac{\partial \psi}{\partial x}$

2.4 Boundary Conditions

(a) Rigid Non-Slip Boundaries

For the rigid non-slip boundaries ($1 < x < D$, $y = 0$;

$0 < y < L$, $x = D$; and $y = L$, $0 < x < (D - Ho)$) the non-dimensional velocity is zero

$$u = v = 0 \tag{2.21}$$

which implies that

$$\frac{\partial^2\psi}{\partial^2 s} = \frac{\partial\psi}{\partial s} = 0$$

where s is the spacial component parallel to the boundary. Hence, the stream function is constant along the non-slip boundaries

$$\psi = \text{constant} \tag{2.22}$$

and the definition of vorticity (equation (2.20)) reduces to

$$\zeta = -\frac{\partial^2\psi}{\partial n^2} \tag{2.23}$$

where n is the spacial component normal to the boundary.

The rigid non-slip boundaries are adiabatic and therefore the temperature boundary condition is

$$\frac{\partial\theta}{\partial n} = 0 \tag{2.24}$$

(b) Surface Boundary ($x = 0$, $0 < y < L$)

On the assumption of a horizontal free surface the vertical velocity (u) is zero, hence

$$\frac{\partial^2\psi}{\partial y^2} = \frac{\partial\psi}{\partial y} = 0$$

and

$$\psi = \text{constant} \tag{2.25}$$

which is arbitrarily set at zero.

In the absence of wind stresses and assuming surface tension forces are negligible the vorticity along the free surface becomes

$$\zeta = -\frac{\partial^2\psi}{\partial x^2} = 0 \qquad (2.26)$$

and the horizontal velocity is given by

$$v = -\frac{\partial\psi}{\partial x} \qquad (2.27)$$

Heat is transferred across the air water interface of a cooling pond by conduction, radiation and evaporation. It is assumed that the mass transfer by evaporation is negligible and the subsequent heat loss, together with that due to radiation, can be represented by an overall heat transfer coefficient. Distinguishing dimensional quantities by primes, the rate of heat transfer from the water per unit width dq' is given by

$$dq' = k \left.\frac{\partial T'}{\partial x'}\right|_{x=0} dy'$$

where k is the thermal conductivity of the water. The rate of heat transfer to the air can be expressed as

$$dq' = ha\ (Tu - Ta)\ dy'$$

where ha is the overall heat transfer coefficient from the water surface to the air.

Hence, the temperature gradient at the surface is given by

$$\left.\frac{\partial T'}{\partial x'}\right|_{x=0} = \frac{ha}{k}\,(Tu' - Ta') \qquad (2.27)$$

Non-dimensionalising equation (2.27) gives

$$\frac{\partial\theta}{\partial x} = \frac{Nu}{L}(\theta u) \qquad (2.28)$$

where Nu is the Nusselt Number defined by

$$Nu = \frac{ha l}{k}$$

(c) Inlet Boundary Conditions ($0 < x < 1, y = 0$)

Heat and mass are transferred across the boundary at the inlet. The velocity at the inlet is assumed to be horizontal (i.e. $u = 0$) and the distribution across the inlet

$$vin' = f\ (x')$$

(is parabolic such that at $x = 0$.)

$v' = v'max$ and $\frac{\partial v}{\partial x} = 0$; at $x = 1$, $v = o$

Hence, the non-dimensional velocity distribution is given by

$$vin = \frac{3}{2}(1 - x^2) \quad \text{for} \quad 0 < x < 1 \qquad (2.29)$$

The temperature at the inlet is assumed to be uniform and hence the non-dimensional temperature is unity, i.e. $\theta = 1$ for $0 < x < 1$.

The stream function and vorticity distributions across the inlet are found from

$$v = -\frac{\partial\psi}{\partial x}$$

where $\psi = 0$ at $x = 0$ by definition, and

$$\zeta = -\frac{\partial^2\psi}{\partial x^2} = \frac{\partial v}{\partial x}$$

which for the velocity distribution assumed (2.29) give the following stream function and vorticity distributions:

$$\psi = \frac{x^3}{2} - \frac{3x}{2} \tag{2.30}$$

$$\zeta = -\ 3x \tag{2.31}$$

The stream function at x = 1 is given by equation (2.30) as

$$\psi = -1 \tag{2.32}$$

and by equation (2.22) ψ has this value along the boundaries $1 < x < D$, $y = 0$ and $x = D$, $0 < y < L$.

(d) <u>The Outlet Boundary Conditions</u>
<u>($(D - Ho) < x < D$, $y = L$)</u>

Conservation of mass implies that the mass flow across the outlet is the same as that across the inlet. Hence, assuming that the vertical velocity at the outlet is zero (i.e. u = 0), the mean velocity at the outlet is expressed as

$$\int_{D-Ho}^{D} \text{vout}\ dx = \int_{0}^{1} \text{vin}\ dx = 1.0$$

Assuming a parabolic velocity distribution at the outlet is similar to laminar flow between parallel plates, i.e. at x = D, v = 0 and at x = D - Ho, v = 0 the velocity distribution is given by

$$v = -\frac{6}{Ho^3}\left| x^2 - (2D - Ho)x + D^2 \ - D\ Ho \right| \tag{2.33}$$

for

$$(D - Ho) < x < D$$

and hence the stream function and vorticity distributions are

$$\psi = \frac{6}{Ho^3}\left|\frac{x^3}{3} - (D - \frac{Ho}{2})x^2 + D(D - Ho)x + \frac{HoD^2}{2} + \frac{Ho^3}{6} - \frac{D^3}{3}\right| \tag{2.34}$$

$$\zeta = -\frac{6}{Ho^3}\left| 2x - 2D + Ho \right| \tag{2.35}$$

Since no heat transfer occurs away from the system in the vicinity of the outlet, it can be assumed that heat is transferred across this boundary by convection alone and hence the temperature boundary condition is found from

$$\left.\frac{\partial\theta}{\partial y}\right|_{out} = 0 \tag{2.36}$$

The boundary conditions for the non-dimensional cooling pond shown in Figure 2.3 are summarised in Table 2.1.

TABLE 2.1

NON-DIMENSIONAL BOUNDARY CONDITIONS

Boundary	Velocity	Temperature	Stream Function	Vorticity
$y = 0$, $0 < x < 1$	$u = 0$, $v = \frac{3}{2}(1 - x^2)$	$\theta = 1.0$	$\psi = \frac{x^3 - 3x}{2}$	$\zeta = -3x$
$y = 0$, $1 < x < D$	$u = 0$, $v = 0$	$\frac{\partial\theta}{\partial y} = 0$	$\psi = -1$	$\zeta = \frac{\partial^2\psi}{\partial y^2}$
$0 < y < L$, $x = D$	$u = 0$, $v = 0$	$\frac{\partial\theta}{\partial x} = 0$	$\psi = -1$	$\zeta = -\frac{\partial^2\psi}{\partial x^2}$
$y = L$, $D - Ho < x < D$	$u = 0$, $v = f_1(x)$	$\frac{\partial\theta}{\partial y} = 0$	$\psi = f_2(x)$	$\zeta = f_3(x)$
$y = L$, $0 < x < D - Ho$	$u = 0$, $v = 0$	$\frac{\partial\theta}{\partial y} = 0$	$\psi = 0$	$\zeta = -\frac{\partial^2\psi}{\partial y^2}$
$0 < y < L$, $x = 0$	$u = 0$, $v = -\frac{\partial\psi}{\partial x}$	$\frac{\partial\theta}{\partial x} = \frac{Nu}{L}\theta$	$\psi = 0$	$\zeta = 0$

$$f_1(x) = -\frac{6}{Ho^3}\left| x^2 - (2D - Ho)x + D(D - Ho) \right|$$

$$f_2(x) = -\frac{6}{Ho^3}\left| \frac{x^3}{3} - (D - \frac{Ho}{2})x^2 + D(D - Ho)x + \frac{HoD^2}{2} + \frac{Ho^3}{6} - \frac{D^3}{3} \right|$$

$$f_3(x) = -\frac{6}{Ho^3}\left| 2x - 2D + Ho \right|$$

3. METHOD OF SOLUTION OF THE GOVERNING EQUATIONS:

3.1 Selection of Solution Technique

For most practical applications the equations describing fluid motion can not be solved analytically and numerical techniques must be employed in an effort to obtain a solution. The numerical technique used to solve the cooling pond problem was to approximate the governing equations (2.18, 2.19, 2.20) by finite differences derived from the Taylor's expansion(4). The resulting set of finite difference equations was solved at a series of mesh points superimposed on the solution region.

The steady state equations derived in Chapter 2 are a set of coupled non-linear elliptic equations and as such are difficult to solve numerically(4). The order of difficulty can be reduced by assuming that the steady state solution is unique and therefore can be reached by solving the time dependent governing equations from some initial condition, through a sequence of time steps, until the steady state solution is reached. Including the time dependent term in the governing equations for the cooling pond problem (2.18, 2.19, 2.20) gives

$$\frac{\partial \zeta}{\partial t} = \frac{1}{Re} \nabla^2 \zeta + \frac{1}{Fi^2} \frac{\partial \theta}{\partial y} - \left(u \frac{\partial \zeta}{\partial x} + v \frac{\partial \zeta}{\partial y}\right) \tag{3.1}$$

$$\frac{\partial \theta}{\partial t} = \frac{1}{Re\ Pr} \nabla^2 \theta - u \frac{\partial \theta}{\partial x} - v \frac{\partial \theta}{\partial y} \tag{3.2}$$

$$0 = \zeta + \nabla^2 \psi \tag{3.3}$$

Equations (3.1) and (3.2) are parabolic in time and, after linearising assumptions are made to their finite difference approximations, they can be solved by a single iterative scheme(3). Equation (3.3), however, remains of elliptic form and its numerical solution requires an iterative technique at each time step to determine the stream function ψ at that time. Hence the overall solution process is a double iterative procedure although only one inner iterative cycle is needed as compared with three for the solution of the steady state equations.

Mallinson and de Vahl Davis(16) reasoned that when the steady state solution is unique, and hence is independent of the transient approach to it, arbitrary transient terms may be added to the governing equations such that a steady state solution is reached with a minimum of computational effort. They used this false transient method to study natural convection in a cell and found that by suitable choice of the false transient terms the steady state solution was reached with at least an order of magnitude less computer effort than had been possible with previous techniques.

Preliminary experiments performed by the author suggested that the steady state solution to the cooling pond problem was unique but the approach to steady state was slow. Hence by using the false transient solution technique it was thought that a numerical solution could be obtained within reasonable computer time. The false transient method has also been successfully applied to various three-dimensional problems (17), and hence could be used to solve the three-dimensional cooling pond problem.

3.2 The False Transient Equations

The false transient method (described in Reference 16) transforms equation (3.3) into parabolic form by the addition of a transient term to the left hand side. The time derivatives of (3.1) and (3.2) are given modified coefficients. The false transient equations for the cooling pond problem are

$$\frac{1}{\alpha_\zeta}\frac{\partial \zeta}{\partial t} = \nabla^2 \zeta + \frac{Re}{Fi^2}\frac{\partial \theta}{\partial y} - Re\left(u\frac{\partial \zeta}{\partial x} + v\frac{\partial \zeta}{\partial y}\right) \tag{3.4}$$

$$\frac{1}{\alpha_\theta}\frac{\partial \theta}{\partial t} = \nabla^2 \theta - Re\ Pr\left(u\frac{\partial \theta}{\partial x} + v\frac{\partial \theta}{\partial y}\right) \tag{3.5}$$

$$\frac{1}{\alpha_\psi}\frac{\partial \psi}{\partial t} = \nabla^2 \psi + \zeta \tag{3.6}$$

where the values of α_ζ, α_θ and α_ψ are used to control the relative rate of advancement between equations. By suitable choice of these parameters the convergence to the steady state solution can be optimised.

3.3 Numerical Solution of the Equations

3.3.1 Solution Region

The false transient equations (equations (3.4) to (3.6)) and the boundary conditions are approximated using finite differences and solved at the nodes of a mesh superimposed on the

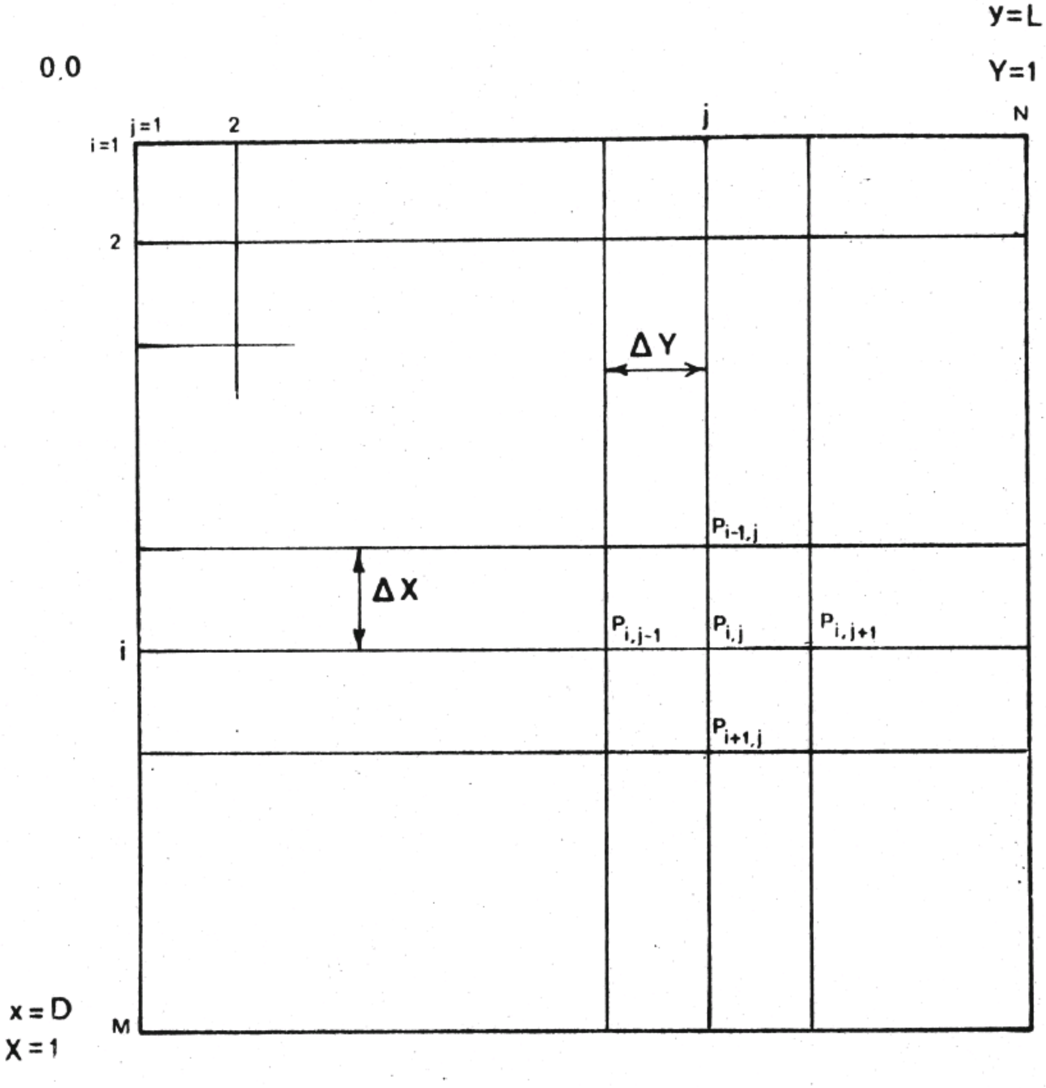

<u>Figure 3.1</u> Mesh notation for the transformed solution region R*.

solution region $R(x,y)$. A non-uniform mesh was employed to obtain greater resolution near the boundaries without the use of a prohibitively fine mesh. Hence, a new solution region $R^*(X,Y)$ can be defined in which a rectangular mesh is employed, and the space variables (x,y) within R^* are defined as

$$x = x\ (X)$$
$$y = y\ (Y) \tag{3.7}$$

The mesh notation used over the region R^* is defined in Figure 3.1.

The transformation employed for the x direction was

$$x = x(X) = D \left| A(e^{nX} - 1.0) + (1.0 - 2A(e^{n/2} - 1.0))X \right|$$

for $\quad 0 < X \leq 0.5$

and $\quad (1 - x) = x\ (0.5 - X) \qquad (3.8)$

for $\quad 0.5 < X < 1.0$

where D is the non-dimensional depth of the pond, and

A and n are constants;

and a similar transformation in the y direction. The form of the transformation is shown in Figure 3.2 for various values of A and n.

3.3.2 Finite Difference Equations

The false transient equations (equations (3.4) to (3.6) are all a special case of the more general equation

$$\frac{\partial \phi}{\partial t} = A\ \left(\frac{\partial^2 \phi}{\partial x^2} + \frac{\partial^2 \phi}{\partial y^2}\right) + B\ \frac{\partial \theta}{\partial y} - C\ \left(u\ \frac{\partial \phi}{\partial x} + v\ \frac{\partial \phi}{\partial y}\right) \tag{3.9}$$

and the finite difference approximation to this general equation will be illustrated here. A full set of finite difference

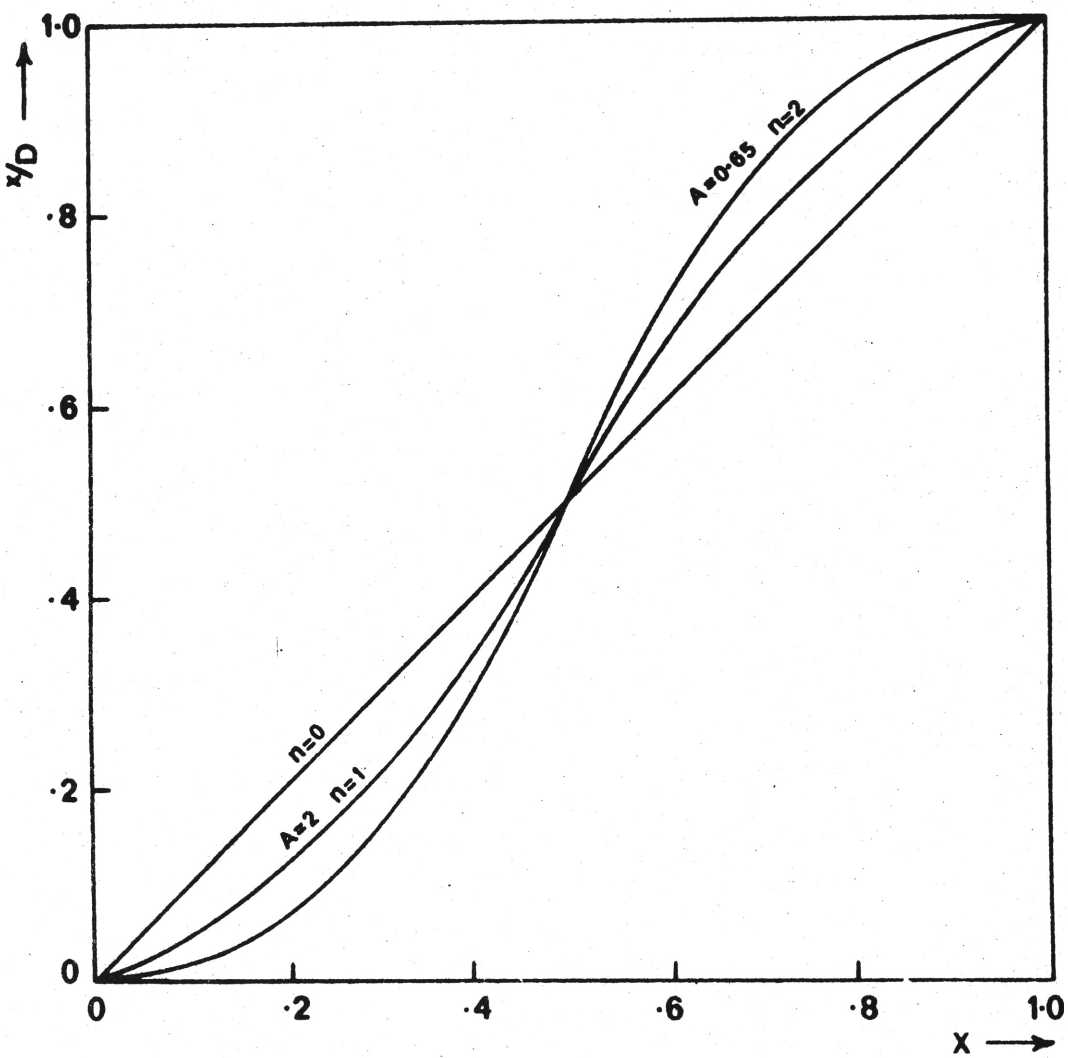

Figure 3.2 Transformation

$x = D/A\ (e^{nX} - 1.0) + (1.0 - 2A(e^{n/2} - 1.0))\ X/$

for various values of A and n.

approximations to the governing equations are given in Appendix A.

Equation 3.9 may be rewritten in terms of the new solution region (R*) defined by equation 3.7 as

$$\frac{\partial\phi}{\partial t} = A \left| X' \frac{\partial}{\partial X}\left(X' \frac{\partial\phi}{\partial X}\right) + Y' \frac{\partial}{\partial Y}\left(Y' \frac{\partial\phi}{\partial Y}\right)\right| \qquad (3.10)$$

$$+ B\, Y' \frac{\partial\theta}{\partial Y} - C \left| X'u \frac{\partial\phi}{\partial X} + Y'v \frac{\partial\phi}{\partial Y}\right|$$

where $X' = \frac{\partial X}{\partial x}$ and $Y' = \frac{\partial Y}{\partial Y}$

Using the notation defined in Figure 3.1 the derivatives on the R.H.S. of equation 3.10 can be represented for the $P_{i,j}$ node using a central differencing approximation(4).

Hence,

$$Y' \frac{\partial\theta}{\partial Y} = \frac{Y'_j}{2\Delta Y}\left(\theta_{i,j+1} - \theta_{i,j-1}\right) \qquad (3.11)$$

The advection term

$$X'u \frac{\partial\phi}{\partial X} + Y'v \frac{\partial\phi}{\partial Y}$$

may be rewritten in conservative form by utilising the continuity equation as

$$X' \frac{\partial}{\partial X}(u\phi) + Y' \frac{\partial}{\partial Y}(v\phi)$$

the latter form guaranteeing conservation of ϕ in the finite difference approximation(16).

The central difference approximation to the advection term becomes

$$X' \frac{\partial}{\partial X}(u\phi) + Y' \frac{\partial}{\partial Y}(v\phi) = X_i' \frac{\left(u_{i+1,j}\,\phi_{i+1,j} - u_{i-1,j}\,\phi_{i-1,j}\right)}{2\Delta X}$$

$$+ Y'_j \frac{(v_{i,j+1}\,\phi_{i,j+1} - v_{i,j-1}\,\phi_{i,j-1})}{2\Delta Y} \tag{3.12}$$

The diffusion term may be approximated by expressing each differential by a central difference approximation over half one mesh interval.

Hence,

$$X' \frac{\partial}{\partial X}(X' \frac{\partial \theta}{\partial X}) = X' \frac{\partial}{\partial X} \left| \frac{X'_i\,(\phi_{i+\frac{1}{2},j} - \phi_{i-\frac{1}{2},j})}{\Delta X} \right|$$

$$= X'_i \left| \frac{X'_{i+\frac{1}{2}}\,(\phi_{i+1,j} - \phi_{i,j})}{\Delta X^2} \right|$$

$$- \frac{X'_i \left| X'_{i-\frac{1}{2}}\,(\phi_{i,j} - \phi_{i-1,j}) \right|}{\Delta X^2} \tag{3.13a}$$

and similarly,

$$Y' \frac{\partial}{\partial Y}(Y' \frac{\partial \phi}{\partial Y} = Y'_j \left| \frac{Y'_{j+\frac{1}{2}}\,(\phi_{i,j+1} - \phi_{i,j})}{\Delta Y^2} \right|$$

$$- Y'_j \left| \frac{Y'_{j-\frac{1}{2}}\,(\phi_{i,j} - \phi_{i,j-1})}{\Delta Y^2} \right| \tag{3.13b}$$

Abbreviating the foregoing finite difference equation by the notation

$$\delta_x\,\phi_{i,j} = \frac{X'_i}{2\Delta X}\,(\phi_{i+1,j} - \phi_{i-1,j}) \tag{3.14}$$

and

$$\delta_x{}^2\,\phi_{i,j} = \frac{X'_i}{\Delta X^2} \left| X'_{i+\frac{1}{2}}\,(\phi_{i+1,j} - \phi_{i,j}) \right|$$

$$- \frac{X'_i}{\Delta X^2} \left| X'_{i-\frac{1}{2}}\,(\phi_{i,j} - \phi_{i-1,j}) \right| \tag{3.15}$$

the finite difference approximation to the R.H.S. of equation 3.9 is

$$\frac{\partial}{\partial t}\phi_{i,j} = A \left| \delta_x^2 \phi_{i,j} + \delta_y^2 \phi_{i,j} \right| + B\delta_y\theta_{i,j} - C \left| \delta_x(\phi u)_{i,j} + \delta_y(\phi v)_{i,j} \right| \tag{3.16}$$

3.3.3 Solution of the Finite Difference Equation

To obtain a solution to equation 3.16 the linearising assumption is made that it is an equation in ϕ only, all other variables being constants known from their most recent estimate in their respective equations.

The solution to equation 3.16 can be advanced through one time interval by using the Implicit Alternating Direction (A.D.I.) method(4). Essentially this method is to employ two difference equations to progress through one time step. The first is implicit in the x direction and explicit in the y direction to progress the solution through one half of the time step. The second is explicit in the x direction and implicit in the y direction to progress the solution through the other half of the time step.

Introducing the notational superscript n to indicate the time t_1 and (n + 1) the time at $(t_1 + \Delta t)$ (where t is the time step), and hence $(n + \frac{1}{2})$ is the time at $(t_1 + \frac{\Delta t}{2})$, the A.D.I. method may be written for equation 3.16 as

$$\frac{\phi_{i,j}^{n+\frac{1}{2}} - \phi_{i,j}^{n}}{\Delta t/2} = A \left| \delta_x^2 \phi_{i,j}^{n+\frac{1}{2}} + \delta_y^2 \phi_{i,j}^{n} \right| + B\delta_y\theta_{i,j}^{n}$$

$$- C \left| \delta_x \left(\phi^{n+\frac{1}{2}} u^n\right)_{i,j} + \delta_y \left(\phi^n v^n\right)_{i,j} \right| \tag{3.17}$$

for the first half time step, and

$$\frac{\phi_{i,j}^{n+1} - \phi_{i,j}^{n+\frac{1}{2}}}{\Delta t/2} = A \left| \delta_x^{\,2} \phi_{i,j}^{\;n+\frac{1}{2}} + \delta_y^{\,2} \phi_{i,j}^{\;n+1} \right| + B\delta_y \theta_{i,j}^{\;n}$$

$$- C \left| \delta_x \left(\phi^{n+\frac{1}{2}} u^n\right)_{i,j} + \delta_y \left(\phi^{n+1} v^n\right)_{i,j} \right| \tag{3.18}$$

for the second half time step. The value of $\phi_{i,j}^{n+\frac{1}{2}}$ is found from the first equation (3.17) and the values of θ^n, u^n and v^n are the most recent estimates of these variables at time t_1.

Rearranging equation 3.17 with the unknowns on the L.H.S. gives

$$\frac{2}{\Delta t} \phi_{i,j}^{n+\frac{1}{2}} - A\delta_x \phi_{i,j}^{n+\frac{1}{2}} + C\delta_x \left(\phi^{n+\frac{1}{2}} u^n\right)_{i,j}$$

$$= \frac{2}{\Delta t} \phi_{i,j}^{\;n} + A\delta_y^{\,2} \phi_{i,j}^{\;n} + B\delta_y \theta_{i,j}^{\;n} - C\delta_y \left(\phi^n v^n\right)_{i,j} \tag{3.19}$$

Applying this equation to the jth column in the solution region, incorporating the given boundary conditions, gives the matrix equation

$$|D| \{\phi_i\}_j^{n+\frac{1}{2}} = |E| \{\phi_i\}_j^n + F$$

$$= \{G\} \tag{3.20}$$

the L.H.S. of which is known and can be evaluated. $|D|$ is a tridiagonal matrix and can be inverted by the Thomas algorithm(4) to give the new estimate of ϕ at the half time step as

$$\{\phi_i\}_j^{n+\frac{1}{2}} = |D|^{-1} \{G\} \tag{3.21}$$

Repeating this process for the (N-2) unknown columns gives the new field of $\phi_{i,j}$ over the solution region for the first half of the time step.

A similar procedure is then applied to equation 3.18 using the values of $\phi_{i,j}^{n+\frac{1}{2}}$ as the known values on the L.H.S. of equation 3.20 to obtain the new values of $\phi_{i,j}^{n+1}$ at the end of one complete time step.

The A.D.I. technique is found to be stable for all values of Δt when applied to a single linear equation. Mallinson and de Vahl Davis(16) found, however, that when solving a system of equations, the coupling between the equations imposes an upper limit on the usable time step. For an even mesh spacing they found the stability ratio $DT = \Delta t/\Delta x^2$ to have an upper limit of 0.8 when the parameters α had a value of unity. This criteria was used as an upper limit on the time interval Δt. The time interval for the transformed mesh is given by

$$\Delta t = DT/2 \left| \frac{1}{\Delta x^2} + \frac{1}{\Delta y^2} \right| \tag{3.22}$$

where DT is the stability ratio ($DT \leq 0.8$), and

Δx and Δy are the true mesh spacings.

3.3.4 Finite Difference Approximation to the Boundary Conditions

The derivative boundary conditions (section 2.4) were approximated using a forward (or backward) differencing scheme which gave a second order approximation to the particular boundary condition.

For example, on the vertical non slip boundary $1 < x < D$, $y = 0$, the vorticity boundary condition is

$$\zeta = - \frac{\partial^2 \psi}{\partial y^2}$$

Applying Taylor's expansion to the ith point along this boundary

$$\psi_{j+1} = \psi_j + h\,\psi_j' + \frac{h^2}{2!}\,\psi_j'' + \frac{h^3}{3!}\,\psi_j''' + O(h^4) \qquad (3.23)$$

where $O(h^4)$ is the order of magnitude of the error associated with neglecting the remaining terms in the expansion, and

h is the actual mesh size next to the boundary, i.e.

$$h = y_{j+1} - y_j$$

Similarly,

$$\psi_{j+2} = \psi_j + k\,\psi_j' + \frac{k^2}{2!}\,\psi_j'' + \frac{k^3}{3!}\,\psi_j''' + O(k^4) \qquad (3.24)$$

where $\qquad k = y_{j+2} - y_j$

Multiplying equation 3.23 by $\frac{k^3}{h^3} = r^3$ and subtracting equation 3.24 from the result gives, after implementing the velocity boundary condition ($u_j = 0$),

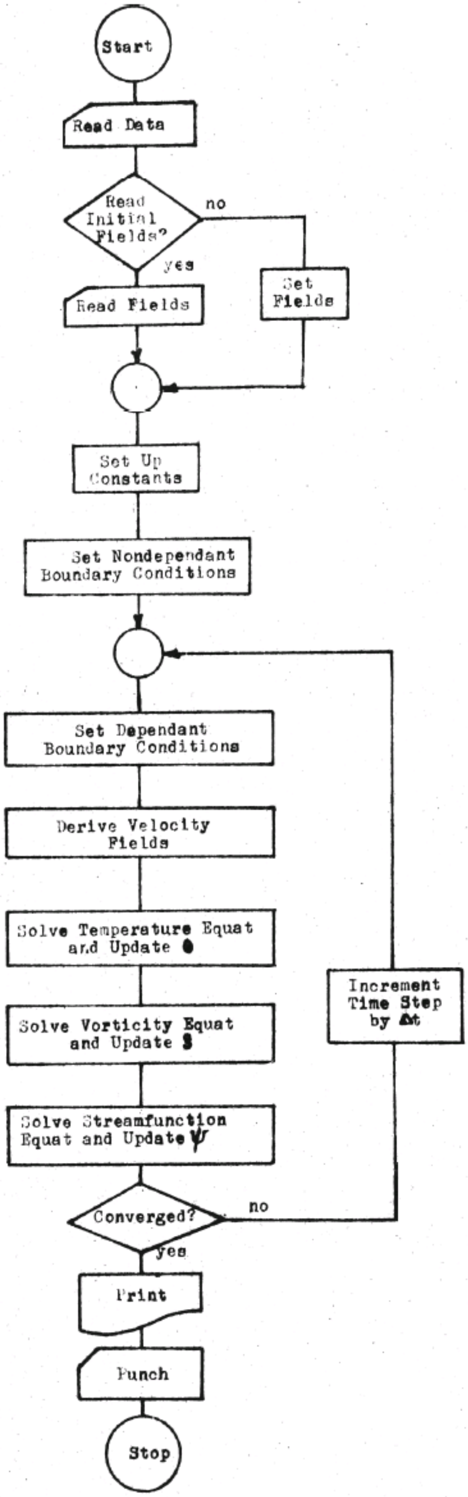

<u>Figure 3.3</u> Simplified flow chart for the solution of the finite difference equations to the cooling pond problem.

$$\zeta_{i,1} = -\psi''_{i,1} = \frac{-2}{k^2(r-1)}\left| r^3\,\psi_{i,2} - \psi_{i,3} - (r^3-1)\psi_{i,1}\right| \qquad (3.25)$$

where $r = \frac{k}{h}$

A complete set of finite difference approximations to the derivative boundary conditions shown in Table 2.1 is given in Appendix B.

3.4 The Overall Solution Procedure

The overall solution procedure is described here in step by step form and the resultant computer procedure used is shown in flow chart form in Figure 3.3 -

(a) The initial values of temperature, vorticity and stream functions are set up either as zero, or from the results of a previous solution.

(b) The non-variant boundary condition and co-ordinate transformations are determined.

(c) The boundary conditions which depend upon the most recent values of ψ, θ and ζ are determined.

(d) The velocity field is set up from $u = \frac{\partial\psi}{\partial y}$ and $v = -\frac{\partial\psi}{\partial x}$.

(e) The temperature equation is incremented by one time step using the A.D.I. technique and the most recent estimate of the temperature field is updated.

(f) Step (e) is repeated for the vorticity equation and stream function equation respectively.

(g) Steps (c) to (f) are repeated, advancing the solution through time until the steady solution has been reached.

The test for convergence to the steady state solution was that proposed by Mallinson and de Vahl Davis(16). The solution was assumed to have converged to the steady state solution when the average rate of change of each of the solution fields, relative to the maximum function value of that field, was less than some pre-determined value ε, where ε was in the range 10^{-4} to 10^{-6}. For example, it was assmmed that a steady state solution for the temperature field had been attained when

$$\sum_{i=1}^{M} \sum_{j=1}^{N} \left| \frac{\theta_{i,j}^{n+1} - \theta_{i,j}^{n}}{(\theta_{i,j}^{n+1})_{max}} \right| \leq M.N\ \alpha_{\theta} \frac{\Delta t}{\Delta Z^2} \varepsilon \tag{3.27}$$

where ΔZ is the smallest mesh interval.

Similar criteria were applied to the vorticity and stream function equations. The solution was assumed to have converged when all three equations satisified this criteria.

4. NUMERICAL RESULTS AND DISCUSSION

The solution of the finite difference equations was carried out initially on the IBM 360/50 computer at the University of New South Wales and later using the State Electricity Commission of Victoria's IBM 370/155 computer.

4.1 Stability, Convergence and Consistency

For any numerical technique to be successful in solving a system of partial differential equations, the procedure should be stable, consistent and convergent. The finite difference approximation to the partial differential equations are

(a) stable if, as the solution progresses through time, the errors associated with the finite difference approximation remain bounded;

(b) consistent with the partial differential equations if, as the time step and mesh size decreases, (i.e. as the number of mesh points increases) the finite difference approximation approaches the partial differential equations;

(c) convergent if, as the time step and mesh size approach zero, the solution to the finite difference equations approaches the solution to the partial differential equations.

It can be shown for a linear partial differential equation that if the consistent finite difference approximation is stable then it is convergent, and vice versa. However, no similar theory is available for non-linear partial differential equations and, with the added difficulty of coupling between equations, the ultimate proof of convergence lies in the comparison of the solution with experimental results.

Consistency is dependent upon the finite difference approximation used. Examination of the errors associated with the finite difference approximation derived in Chapter 3 indicates that these equations are consistent with the partial differential equations.

The stability of the solution is dependent upon the equations and the method used to solve the equations. Previous workers(15) have found the A.D.I. technique used here to be inherently stable, and hence the limitation on the allowable time step reported here was attributed to the coupling between the equations.

4.2 Modifications to Solution Procedure

In using the false transient method to solve the governing equations it was assumed that the steady state solution was unique and therefore independent of the initial conditions and the transient approach to the steady state. This assumption was questioned in the solution of the cooling pond problem, as it was

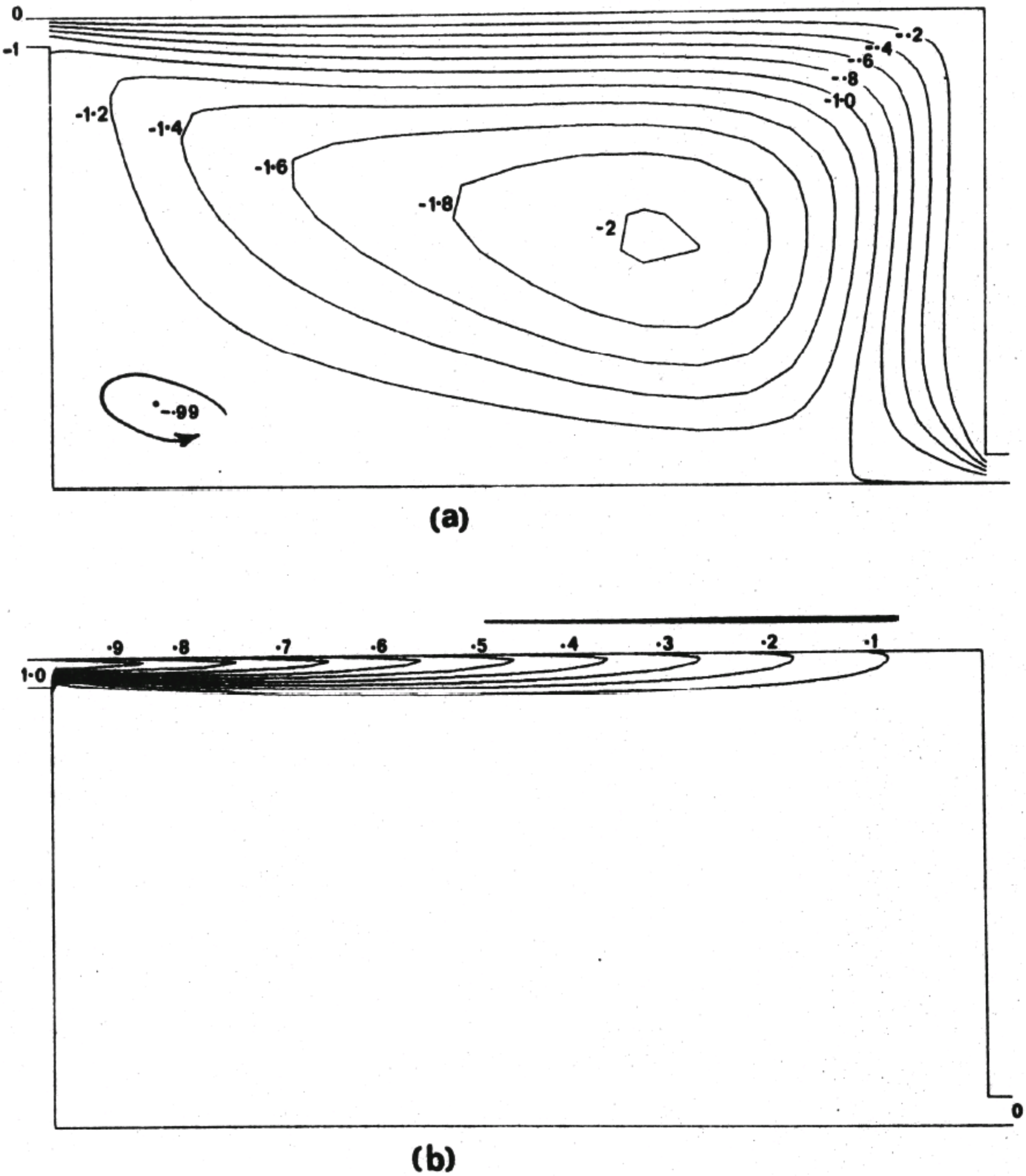

<u>Figure 4.1</u> Numerical Solution -

(a) Streamlines and (b) the assumed isotherm contours for Re=10, Fi^2=1.2, D=16, L=32 using a 31x31 mesh.

found that some initial conditions from which a solution was attempted resulted in numerical instability regardless of the time step used. This instability was traced to the temperature field being convected into the body of the solution region by the developing flow field. The flow field, in response to the buoyancy, tended to move towards the top surface to form what has been termed the surface layer. The heat transfer away from the top boundary caused this fluid to become cooler than the underlying fluid. Consequently, convective cells were set up within the body of the pond to rectify this anomaly and the rapidly changing temperature and vorticity fields caused the solution field to become unstable.

A similar effect to that described above could be produced in the experimental rig, described in Chapter 5, by increasing the heat transfer away from the surface of a previous steady state experiment. Consequently, the effect was a real one and cannot be attributed to a lack of uniqueness or inconsistency in the finite difference approximations.

This problem was overcome by assuming a temperature field in the surface layer and solving the vorticity and stream function equations for this assumed temperature field until the characteristic flow pattern (see Figure 4.1) was established. The temperature equation could then be incorporated in the solution and, provided that the heat transfer coefficient was less than that which would give the assumed temperature distribution, the normal solution procedure resumed.

4.3 Results

The geometric configuration of the solution region was limited to the dimensions defined by the experimental rig so that a direct comparison could be drawn between the numerical and experimental results. The upper limit of the Reynolds Number for which solutions could be obtained depended upon the length of the cooling pond. A Reynolds Number based on the cooling pond length (Re_l) can be expressed in terms of the inlet Reynolds Number (Re) by -

$$Re = Re_l \times L \qquad (4.1)$$

where $L = \frac{l}{hi}$ is the non-dimensional length, and provided $Re_l < 1500$ stable solutions could be obtained.

A solution region of dimensions L = 2D was used with a non-dimensional depth (D) (as fixed by the allowable adjustment of the inlet depth in the experimental rig) of 16. In order to represent the boundary conditions at the inlet and outlet over as many mesh points as possible and at the same time keep the number of mesh points within reasonable limits to conserve computer effort, the transformation given by equation 3.8 was employed with the constants A = 0.65 and n = 2. For a 31 x 31 mesh, this

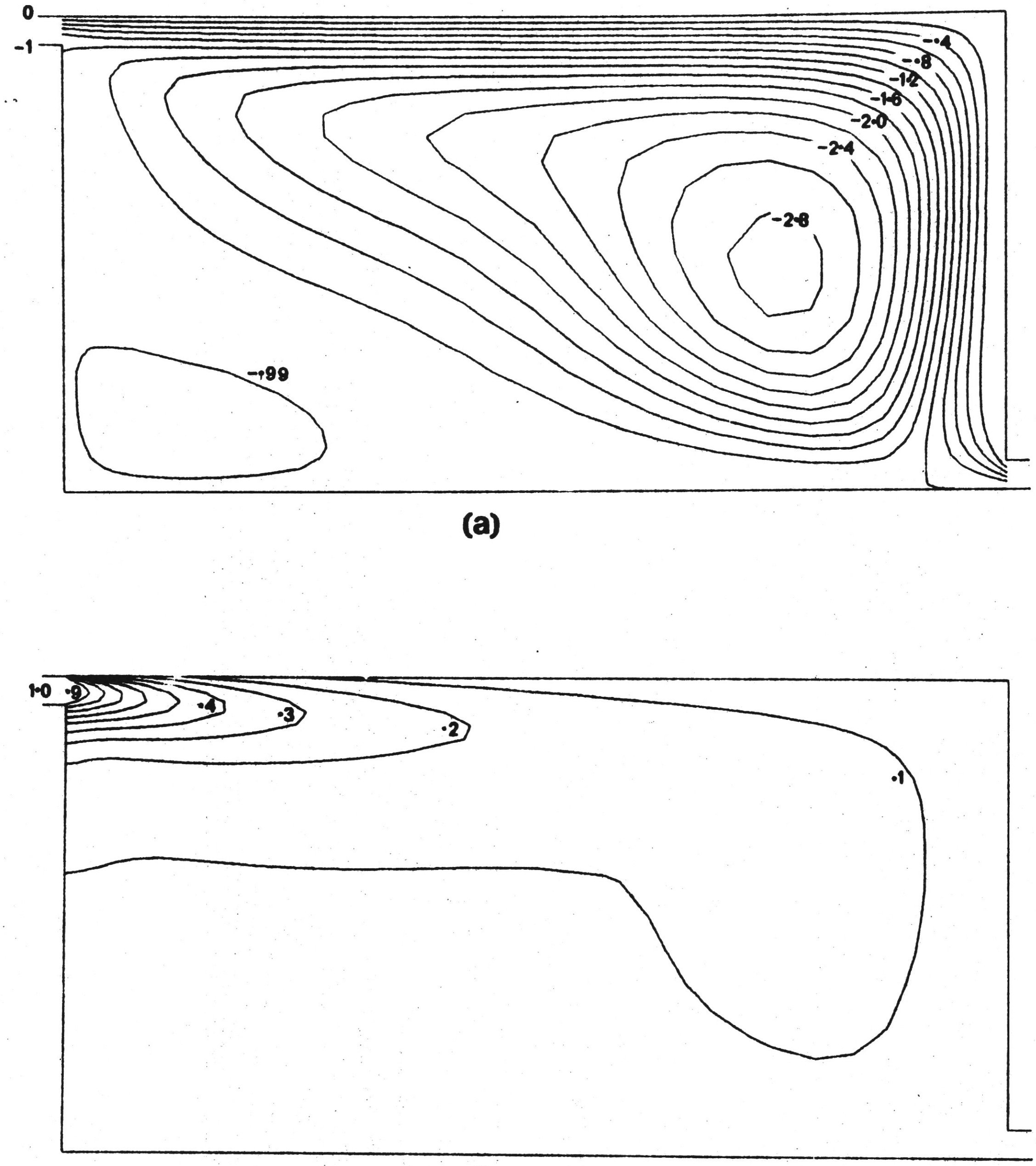

<u>Figure 4.2</u> Numerical Solution -

(a) Streamlines and (b) isotherm contours for $Re=10$, $Fi^2=1.2$, $Pr=1.0$, $Nu=100$, $D=16$, $L=32$ using a 31x31 mesh.

gave 6 mesh points over which the inlet and outlet boundary conditions were represented and a maximum mesh spacing of L/15 at the centre of the solution region.

Figure 4.2 shows the stream function and temperature fields obtained by using, as a starting condition, a previously converged solution (see Figure 4.1) where the temperature field was assumed and the temperature equation excluded from the solution procedure. The non-dimensional variables for these solutions were Re = 10, $F_i^2 = 1.2$, Pr = 1.0, Nu = 100.

Before the temperature equation was included in the solution procedure, the flow consisted of the surface layer flowing along the top surface, in response to the buoyancy forces, and flowing down the end wall and through the outlet. A primary eddy was generated under the surface layer and a very weak secondary eddy was apparent in the corner under the inlet (Fig. 4.1). When the temperature equation was included in the solution procedure, the buoyancy forces, resulting from the convection of the temperature field into the lower portion of the solution region, lifted the reverse flow from the base, distorting the primary eddy and increasing the strength of the secondary eddy. Eventually the temperature field became uniform below the interface and the stream function resumed its previous form (Figure 4.2) with a slight increase in the strength of both the primary and secondary eddies.

The rate of convergence to the steady state solution was governed by the choice of the false transient coefficients and the stability ratio (DT). With $\alpha_\psi = \alpha_\theta = \alpha_\zeta = 1$ the value of DT required to prevent instability in the solution fields was prohibitively small (DT < 0.1). By decreasing the value of α_ζ and α_ψ, the response of the vorticity and stream function fields to the varying temperature field was reduced enabling a larger value of DT to be used, with a considerable saving in computer effort. With $\alpha_\psi = 0.5$ and $\alpha_\zeta = 0.1$ it was found that a stability ratio of 0.3 could be used in the initial stages of the solution, without introducing instability, and gradually increased as the steady state solution was approached. The computer effort required to obtain the steady state solution (see Table 4.1) was large and prevented a wider range of parameters being investigated. Some improvement might have been achieved by further reducing α_ζ and optimising the stability ratio. However, the main contributing factor was thought to be the slow rate at which thermal balance was achieved in the model (this was also a characteristic of the experimental investigation) and the sensitivity of the flow form below the surface layer to small temperature changes convected into this region during the transient approach to steady state. These factors prevented the full benefits of the false transient method being utilised (see Ref. 16).

TABLE 4.1

COMPUTER EFFORT FOR Re = 10, Pr = 1.0, Fi = 1.2, Nu = 100

$\alpha_\theta = 1.0$, $\alpha_\psi = 0.5$, $\alpha_\zeta = 0.1$ and a 31 x 31 MESH

COMPUTATIONS PERFORMED ON IBM 370/155 COMPUTER

Run No.	Initial Conditions	No. of Iterations	Computer Time (min)	Temp. Solution	DT
1	Zero*	400	8.5	No	0.3
2	Run 1	400	8.5	No	0.5
3	Run 2	300	9	Yes	0.3
4	Run 3	300	9	Yes	0.4
5	Run 4	300	9	Yes	0.6
6	Run 5	200	6	Yes	0.8
			Total 50		

* - Solution fields zero.

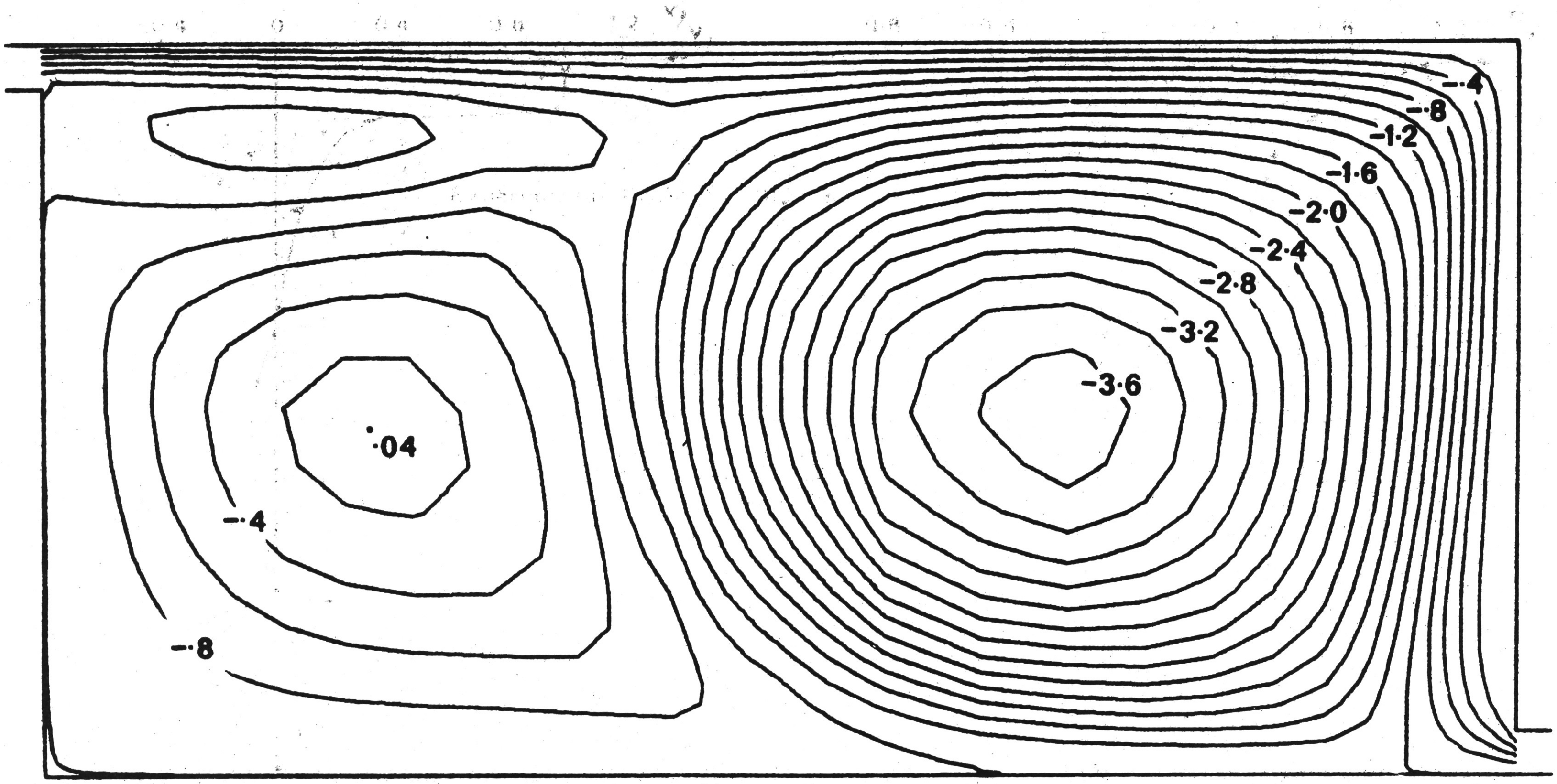

Figure 4.3 Streamlines for Re=40, Fi^2=1.2, D=16, L=32 using a 31x31 mesh and using the temperature fields shown in Fig. 4.1(b).

Differences between the true temperature field and the assumed temperature field had only small effects on the overall flow pattern once steady conditions had been achieved. Hence, solutions at higher Reynolds Numbers were obtained by assuming the temperature distribution and solving only the vorticity and stream function equations.

Increase in the Reynolds Number increased the strength of both the primary and secondary eddies. Figure 4.3 shows the stream function field for Re = 40. The secondary eddy has grown and dominates the flow form under the inlet, while the primary eddy has moved downstream towards the end wall and a third eddy has formed between the secondary eddy and the surface flow.

Experimental results were obtained using the experimental rig described in Chapter 5 for similar geometry and inlet conditions but with Re = 180. The experimental velocity profiles obtained at y/hi = 10 and y/hi = 20 are shown in Figure 4.4 together with the velocity profiles derived from the stream function field of the numerical solution for Re = 40.

The experimental results show a similar primary eddy under the inlet (Figure 4.4a) although it is not as strong as that predicted by the numerical solution, and is lower down in the solution region. The velocity profiles varied considerably

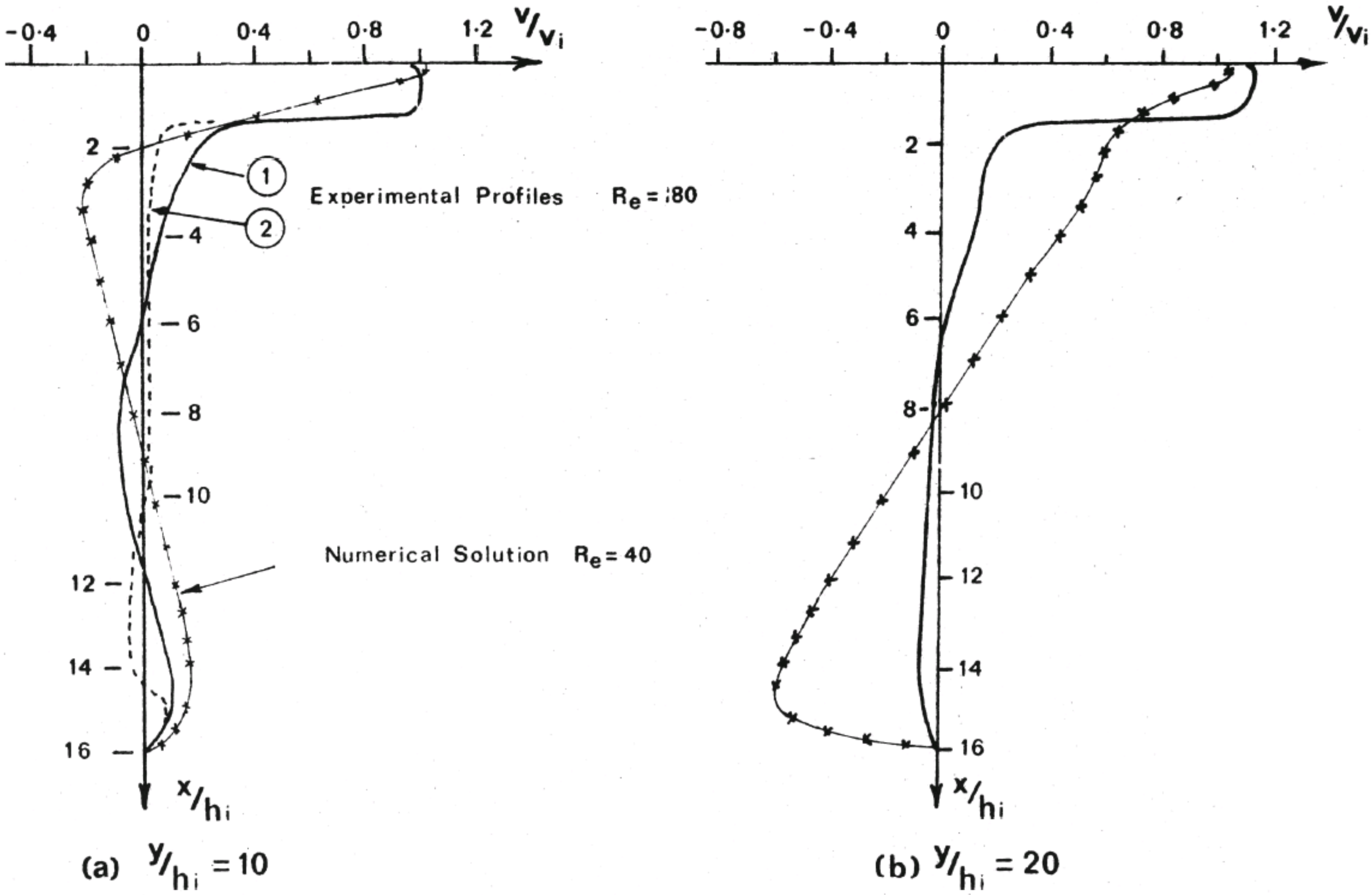

Figure 4.4 Comparison between the vertical profiles of velocity given by the experimental results (Test 17) and that given by the numerical solution (Figure 4.3).

with time in this portion of the flume over the duration of the experiment, velocities dropping to almost zero at some stages (see profile 2, Figure 4.4a). Dye injected into the lower portion of the flume, and observed over a period of time, show that the primary and secondary eddies were separated as shown by the stream function field in Figure 4.3, but the extent of the secondary eddy varied with time. The primary eddy periodically joined up with the third eddy forcing the secondary eddy back into the lower corner of the flume. From this and subsequent experiments (see Chapter 6) it was concluded that the flow below the surface layer was unsteady. Oscillations in the solution fields were also observed in the numerical solution and, although some oscillation is characteristic of the solution technique during the transient approach to steady state(13), the convergence rate would be impaired by any oscillations characteristic of the problem.

The velocity field at $y/hi = 20$ was obtained through a vertical section near the core region of the secondary eddy. The numerical results predict a stronger secondary eddy than that obtained in the experiments (Figure 4.4b) and, as it was found that the strength of the secondary eddy increased as the Reynolds Number increased, the numerical results presented would be an underestimate of the secondary eddie's strength if a solution could be attained at Re = 180.

The secondary eddy is driven by viscous forces originating from the surface flow and from the subsequent flow down the end boundary towards the outlet. Increase in the Reynolds Number results in an increase in the vorticity generated at the flow boundaries,and since in the experimental investigation the flow was turbulent in these regions this vorticity would be diffused through the fluid, whereas the laminar flow assumption of the numerical model results in the vorticity being convected through the solution by the flow field. This would explain some of the discrepancy between the numerical and experimental results. The assumption was made in formulating the governing equations of the mathematical model that the flow was two-dimensional. This implies a solution region of infinite width. In the experimental investigation the side boundaries have an influence on the resulting flow form. Mallison(17A) found, in the investigation of the flow induced in a cube by a sliding lid, that the two-dimensional assumption resulted in an over-estimate if the velocity field. For high Reynolds Number the velocities given by the two-dimensional solution were approximately double those given at the centre plane of the three-dimensional solution, the difference being due to the third dimension's boundaries. The side walls of the flume in the present case would have an even greater influence since the width of the flume was only 1/3 of the depth (D). Mallinson's results suggest that the two-dimensional assumption over-estimates the velocity field obtained in the three-dimensional solution by a factor which is inversely proportional to the width to depth ratio. In the present case this would result in a solution whose velocity field was approximately six times that measured in the experimental investigation. This effect is apparent in the flow region below the interface (Figure 4.4b).

4.4 Conclusions

The numerical technique employed to solve the laminar equations of motion for the two-dimensional cooling pond problem was successful in predicting the flow form within the cooling pond. It is believed that good quantitative agreement with the experimental results would have been obtained if the experimental rig had been of sufficient width to justify the two-dimensional assumption.

The coupling between the governing equations and the inherent instability of the cooling pond problem limited the time step which could be incorporated in the solution. Consequently, the savings in computational effort which can be gained by using the false transient technique could not be fully utilised. The slow convergence to the steady state solution was found to be a general property of the problem and indicated the sensitivity of the flow below the interface to any perturbation from the steady state.

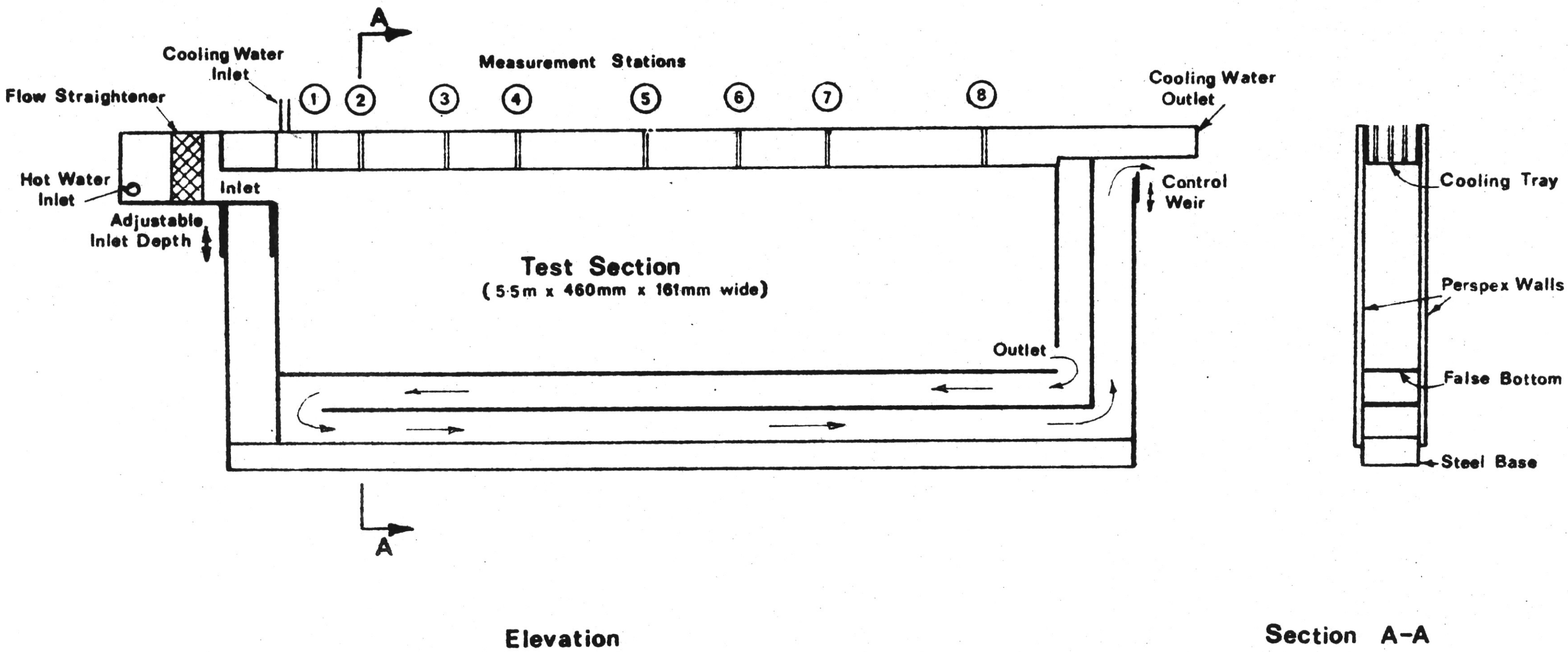

Figure 5.1 Layout of the test flume.

5. EXPERIMENTAL INVESTIGATION

5.1 Experimental Apparatus

The experiments were carried out in a flume 6.4 m long, 760 mm deep and 161 mm wide located at the University of New South Wales Water Research Laboratories. Details of the test flume are shown in Figure 5.1. The walls of the flume were constructed of perspex 19 mm thick bolted to a steel base and supporting frame. A horizontal inlet structure, which could be adjusted to give an inlet depth of up to 50 mm from the free surface, was incorporated in one end of the flume and the outlet was located at the base of a false wall inserted in the other end of the flume. To minimise heat transfer from the test section to the steel base of the flume, a false bottom was inserted so that water from the outlet flowed back under the test section before flowing to waste over a weir. The weir was used to control the free water surface level in the test section.

Significant heat transfer away from the water surface was achieved by placing a cooling tray flush with the water surface and circulating cool water over the tray to act as a heat sink. Access for inserting measuring instruments into the test section was provided by soldering copper tubes to the base of the cooling tray at various intervals along its length.

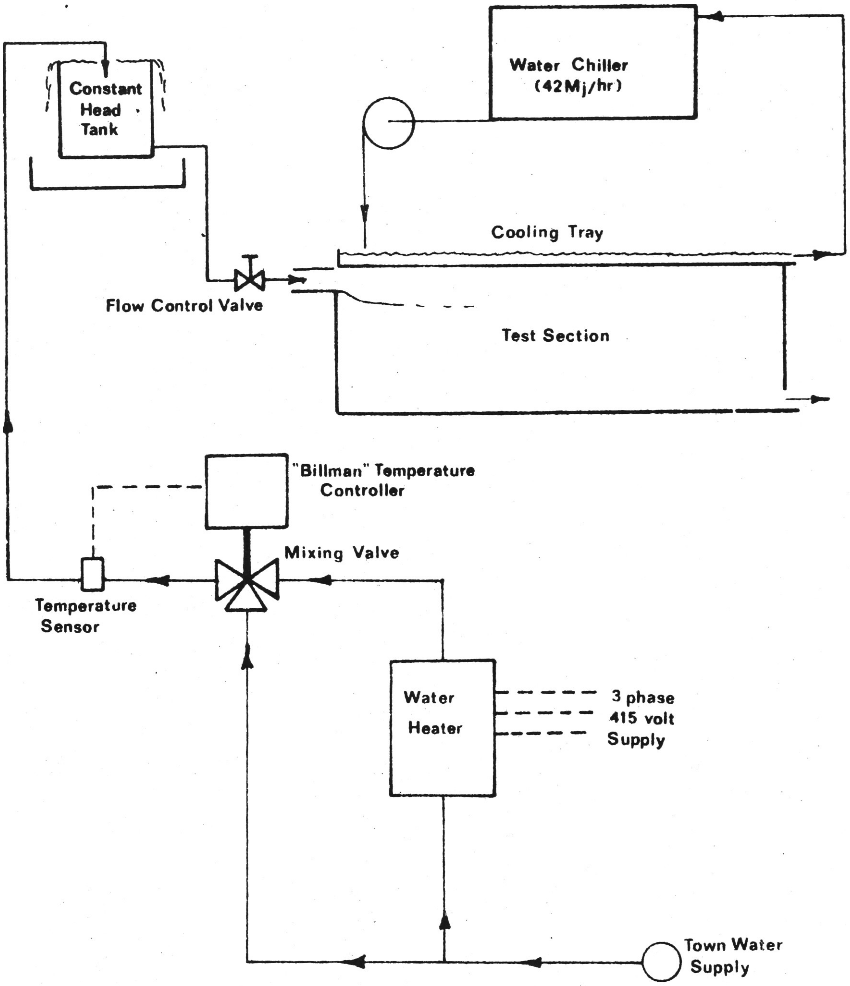

Figure 5.2 Flow circuit and related controls external to the test flume.

The water flowing into the test section was heated by a mains pressure three phase (415 V) electrical heater. Fluctuations in the outlet temperature from the heaters due to variations in the electrical system loading and the town water pressure were found to cause up to 20% fluctuations in the inlet Densimetric Froude Number. This variation was reduced to within 2% of the mean by incorporating an electronically controlled "Billman" mixing valve to control the water temperature and by using a constant head tank to control the flow rate. The temperature and flow control system is shown in Figure 5.2.

Heat loss from the side walls was found to be a problem in earlier experiments (not reported here) when water at ambient temperature ($16^{\circ}C$) was used as the heat sink and the temperature of the water flowing into the flume was raised to approximately $35^{\circ}C$ to obtain a significant temperature drop over the length of the flume. A vertical temperature gradient occurred below the interface and the fluid "snaked" backwards and forwards, in response to this temperature gradient, as it progressed towards the outlet. This problem was overcome by using refrigerated water at approximately $5^{\circ}C$ as the heat sink and dropping the inlet temperature so that the desired temperature difference across the interface was obtained when the water below the interface was at approximately ambient air temperature.

The cooling water for the heat sink was recirculated through a commercially available water chiller (rated at 42 Mj/h) at approximately ten times the rate of the hot water flow. The water chiller was on/off controlled by a pen thermostat resulting in a $2^{o}C$ cyclic variation in the temperature of the water supplied to the cooling tray. The oscillation period of the cooling water temperature was approximately one-quarter of the residence time of the hot water in the surface layer and consequently the variation in the mean heat transfer away from the hot water surface was less than 5%, resulting in a maximum of $0.4^{o}C$ variation in the hot water outlet temperature.

5.2 Measuring Equipment

The variables required to characterise the flow are -

(a) the vertical distribution of temperature;

(b) the vertical distribution of velocity;

(c) the interfacial depth;

(d) the cooling water temperature.

The interfacial depth has been defined as the depth where the density gradient is a maximum. It can, therefore, be determined from the vertical profile of temperature.

5.2.1 Temperature Measurement

Four resistance thermometer units were used to measure the temperature of the hot and cold water at the inlet and outlet.

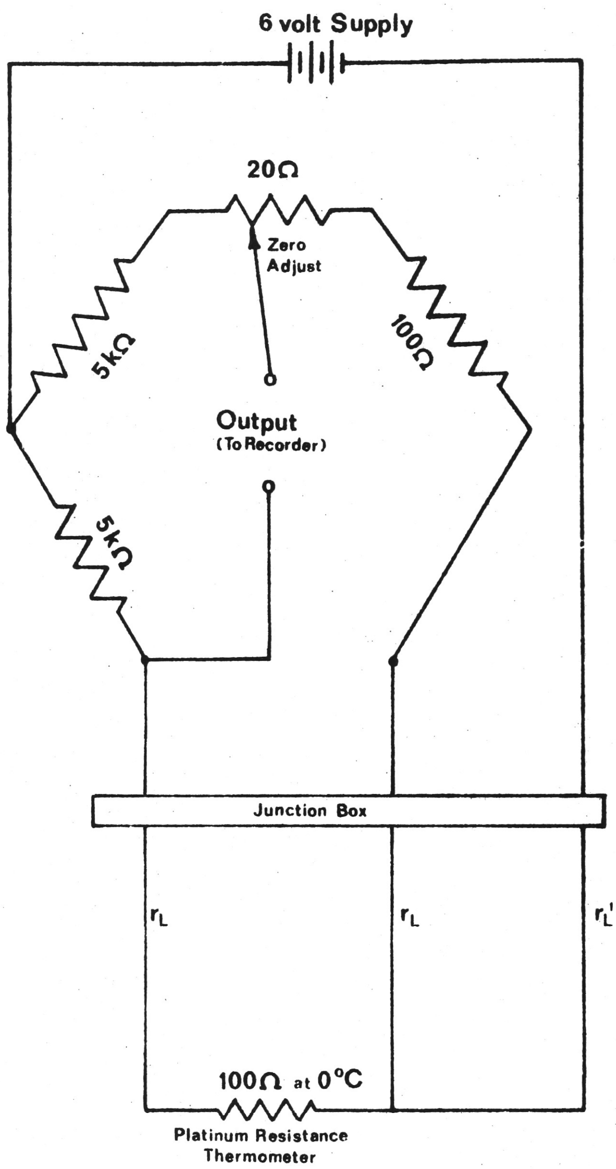

Figure 5.3 Circuit diagram of the platinum resistance thermometer unit (24).

Each unit consisted of a platinum resistance thermometer probe, having a resistance of $100\Omega \pm 0.077\Omega$ at $0^{\circ}C$ and a temperature coefficient of $0.385\Omega/^{\circ}C$, connected via a three wire lead to a bridge network, the third wire (r_L') providing compensation for changes in lead resistance due to temperature variation. Figure 5.3 shows a circuit diagram for a single bridge including lead resistance compensating facilities. A constant voltage E applied across the bridge and through a 5 KΩ resistor defines a current in the thermometer which is independent of temperature(24). Any change in temperature at the probe results in a proportionate change in voltage across the output. The output from each bridge was recorded on one channel of a four channel pen recorder and the output signal calibrated against pen movement by disconnecting the probe from the bridge network and replacing it with resistors whose values corresponded to $5^{\circ}C$, $20^{\circ}C$ and $25^{\circ}C$.

Vertical profiles of temperature were obtained in the test section using a thermistor attached to a motorised traversing mechanism. The rate of travel of the traversing mechanism was controlled by varying the voltage supply to the driving motor, the output speed of which was further reduced by a gear train before driving the main traversing screw. Provision was made in this gear train to reverse the direction of travel of the probe. The thermistor was wired into one arm of a bridge network (see (Figure 5.4), and the output from the bridge recorded on one channel of a two channel pen recorder. The vertical position of the

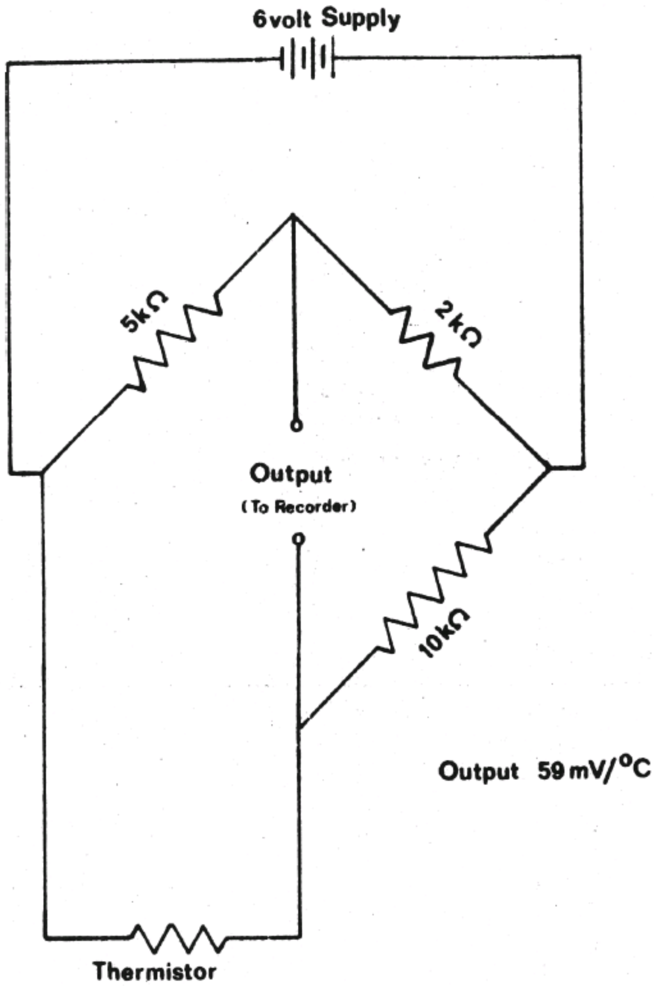

Figure 5.4 Circuit diagram of the thermistor unit used to measure temperature profiles.

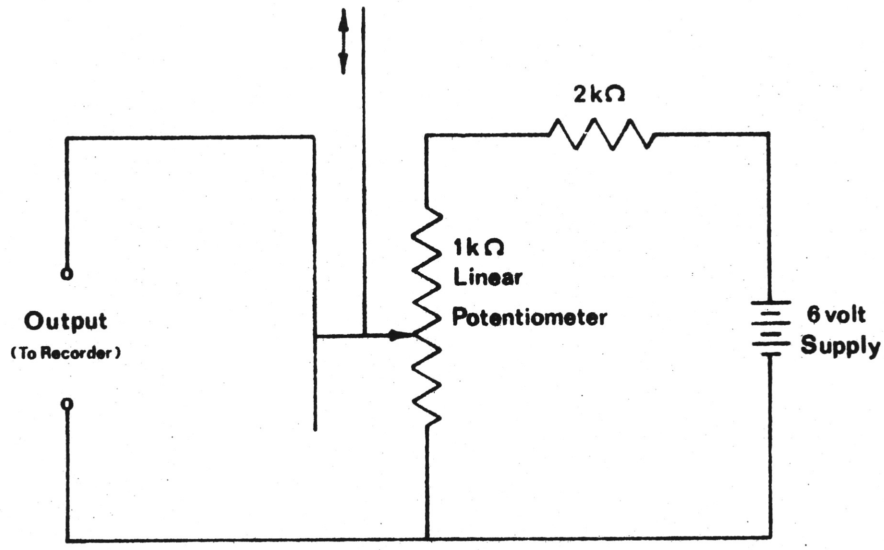

Figure 5.5 Circuit diagram of the linear potentiometer unit used to relate the measured temperature to the depth of traverse.

probe at any given time was obtained by driving the sliding arm of a voltage divider from the traversing mechanism and connecting the variable voltage output of the voltage divider to the second channel of the pen recorder. Hence, by directly calibrating the pen movement against probe travel and correlating the two at some reference depth, the temperature profile could be ascertained from the chart recording. The circuit diagram for the voltage divider is shown in Figure 5.5.

5.2.2 Velocity Measurement

Velocity measurements in laboratory-scale stratified flows are difficult because of the small velocities involved. Typical velocities in the surface layer for the experiments reported here range from 60 mm/sec down to 1 mm/sec. Velocities in the underlying flow are an order of magnitude lower. Instruments suitable for measuring velocities in stratified flow are discussed by Feitz(8) and Wilkinson(23). However, the selection of a suitable technique for the experiments reported here was governed by the convective motion in the surface flow due to the heat transfer away from the surface, and the resulting longitudinal temperature gradient.

Three techniques to determine the velocity profile at a vertical section were tried.

1. Hydrogen bubble technique

A similar technique as that used by Wilkinson(23) was experimented with but it was found that the convective motion in the surface layer dispersed the bubbles before profiles could be obtained.

2. Suspended particles

By choosing small particles whose buoyancy is neutral with respect to the fluid, velocity profiles may be obtained by photographing the particles over a known time interval. Neutrally buoyant particles were, however, caught in the convective motion of the surface layer and tended either to lodge against the cooling tray or to be caught in the boundary layer at the interface. Those particles that survived this condition initially, soon found themselves surrounded by denser fluid (due to the longitudinal temperature gradient) and floated towards the cooling tray.

3. Dye Streaks

This method was found to be the most successful of the three. Dye streaks were generated by dropping crystals of potassium permanganate into the test flume. Velocity profiles were obtained by photographing the position of the dye streak at the beginning and end of a known time interval. The turbulence in the surface layer was found to quickly disperse the dye generated from a single crystal but it was found that by dropping a number of crystals into the flume the dye remained visible for 10 to 15 seconds. This period was sufficient to enable velocity profiles to be obtained. The flow below the interface was laminar and hence this method was found to be quite successful in obtaining representative velocity profiles in this region. However, as discussed later, the velocity distribution across the flume was not uniform below the interface and hence the mean flow in the surface layer could not be checked by a mass balance through a vertical plane.

The dye traces were recorded on colour film against a white background illuminated by six 500 watt photoflood lamps. A green filter was used on the camera lens to improve the contrast between the red dye and the background. Distortion in the photographs due to the relatively short focal length of the camera lens (§ 1.4) was corrected in the analysis of results by reference to a grid marked on the perspex walls of the flume.

The velocity distribution in the surface layer obtained by this method varied considerably from profile to profile. However, the mean velocity measured by integrating the velocity profile over the depth to the interface were reasonably consistent. The centreline velocity distribution in the surface layer was assumed to be representative of the velocity across the flume and although the walls must exert some influence, results suggested that the horizontal velocity profile was typical of turbulent flow between parallel plates. The mean velocity in the surface layer obtained from any one profile was within 10% of the mean calculated from a number of profiles.

5.3 Experimental Procedure

The inlet and outlet temperatures of the cooling water and the hot water were recorded continuously to ensure that steady state conditions were maintained during each test. Temperature and velocity profiles were recorded under steady state conditions.

Thermal steady state was said to have been achieved when a constant hot water outlet temperature was reached and no vertical temperature gradients were discernible below the interface. This usually took 2 - 3 hours from the start of each test run with a further 2 - 3 hours before the flow below the interface responded and became consistent.

Temperature profiles were recorded while traversing in both directions at each measuring station. On each traverse the recording chart was marked when the thermistor had reached a known depth, this being used as the reference level for determining the interfacial depth when analysing the results.

Two velocity profiles were taken on the centreline of each measuring station. To check the two-dimensional nature of the flow, additional velocity profiles were taken 50 mm either side of the centreline for at least two measuring stations in each test.

At the conclusion of each test the inlet hot water was dyed and the flow at the inlet photographed to ascertain whether the inlet was inundated or an internal hydraulic jump formed.

The hot water and the cooling water flow rates were measured at the start and end of each test by weighing a sample collected over a known time interval.

Table 5.1 gives a summary of the physical and non-dimensional variables for each test.

TABLE 5.1

SUMMARY OF TEST CONDITIONS

Test No.	Inlet Depth h_i (mm)	Inlet Temp. (^oC)	Outlet Temp. (^oC)	Inlet Velocity V_i (mm/sec)	Surface Heat Transfer Coefficient $k \times 10^5$ m/sec	Inlet Densimetric Froude No.	Inlet Reynolds Number	Flow Conditions at the Inlet
10	36.1	25.6	16.7	18.8	6.7	0.719	768	Inundation.
11	40.6	25.6	18.1	21.7	6.16	0.869	1000	Inundation.
12	40.6	24.6	19.0	26.6	6.62	1.195	1200	Inundation.
13	22.9	24.2	18.5	46.6	6.25	2.875	1158	Int. Hyd. Jump.
14	17.6	23.9	19.1	57.2	5.33	4.25	1085	Int. Hyd. Jump.
15	31.1	24.4	17.7	23.6	5.58	1.11	810	Inundation.
16*	29.0	21.0	18.2	9.5	6.15	0.73	279	Inundation.
17*	13.6	22.5	17.3	13.1	7.0	1.1	188	Inundation.

NOTE: * - Flume length reduced to 950 mm.

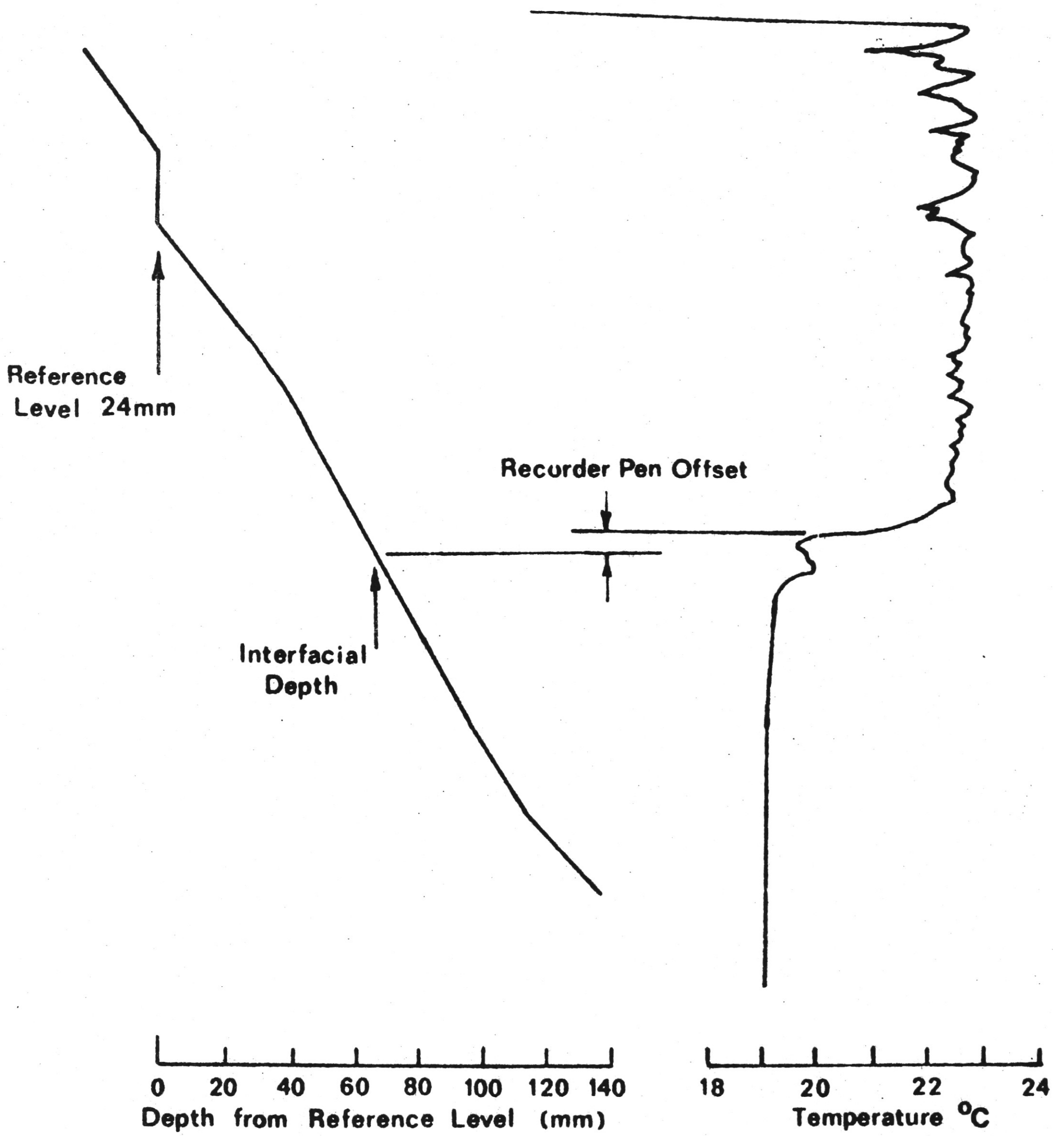

Figure 6.1 Experimental results - typical chart recording of the temperature profile (taken at the third measuring station in Test 12).

6. EXPERIMENTAL RESULTS AND DISCUSSION:

The experimental results are presented in two parts -

(a) the flow above and including the interface (referred to as the surface flow), and

(b) the secondary flow below the interface.

6.1 General Description of the Flow

(a) Surface Flow

Experiments were carried out for Densimetric Froude Numbers at the inlet ranging from 0.7 to 4.5. In all cases the downstream controls were such that either the inlet was inundated or an internal hydraulic jump occurred just downstream of inlet (Tests 13 and 14).

The flow in the surface layer was influenced greatly by the heat transfer away from the surface. A parcel of fluid near the cooling tray cooled to a stage where it was heavier than its surroundings and hence dropped towards the interface where its vertical motion was retarded by the presence of the denser sub-interfacial fluid. Hence, an overall convective motion was imparted to the fluid in addition to the normal turbulence associated with the flow.

The convective motion is reflected in the fluctuations in the temperature profiles (Figure 6.1). The fluctuations decrease in magnitude with increase in depth, indicating that the temperature difference between a descending parcel of fluid and its surroundings is reduced by diffusion of heat.

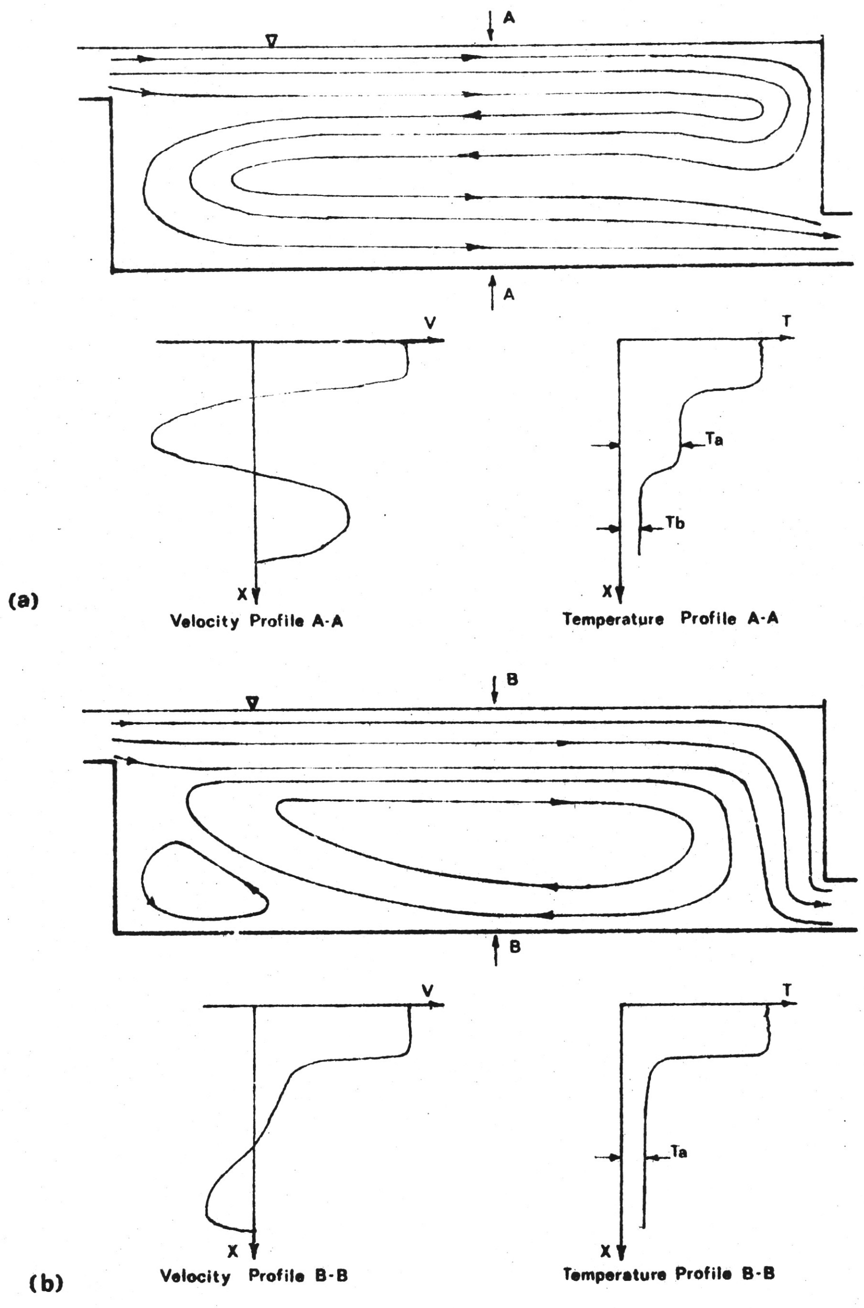

Figure 6.2 Typical flow pattern during (a) the transient approach to steady state and (b) after steady state conditions had been achieved.

In the absence of heat transfer from the surface the interface was disturbed by long waves travelling along it as described by Sherenkov et. al(19) for equivalent values of the stability parameter ($\bar{\theta} = 200 \rightarrow 500$). However, in the presence of heat transfer the interface was irregular with bulge-like depressions protruding through it. This additional disturbance is attributed to the convective motion within the surface layer.

As the surface flow approached the end of the flume the density difference across the interface was reduced and the interface became more disturbed. Just before the end wall parcels of fluid passed through the interface and remained below it, contributing to the general turning effect of the flow at the end wall. Determination of the mean velocity and interfacial depth became more difficult in this region.

(b) Secondary Flow

During the transient approach to the steady state the flow field below the interface changed from a "snaking flow" (where the flow oscillated backwards and forwards until it reached the bottom of the flume and passed through the outlet) to a vertical recirculation eddy under the interface. These two types of flow are represented diagrammatically in Figure 6.2. The transient flow pattern was accompanied by a vertical temperature gradient below the interface and although this gradient was small ($Ta - Tb \simeq 0.2^{o}C$) it was sufficient to affect the form of the flow pattern. Once the temperature below the interface became uniform, the flow changed to the recirculation eddy shown in Figure 6.2(b) and the net volume flow below the interface diminished as the outlet flow was drawn from the subsiding surface layer.

6.2 The Surface Layer

The experimental results have been non-dimensionalised in the following form:

(a) Temperature

$$\theta = \frac{T - Tcw}{Ti - Tcw} \qquad (6.1)$$

where Ti is the water temperature at the inlet to the test section,

T is the mean temperature of the surface flow at a cross-section, and

Tcw is the mean cooling water temperature in the cooling trays.

(b) Interfacial Depth

$$H = \frac{h}{hi} \qquad (6.2)$$

where hi is the depth of the inlet.

(c) Flow Rate/Unit Width

$$VH = \frac{vh}{vi\ hi} \qquad (6.3)$$

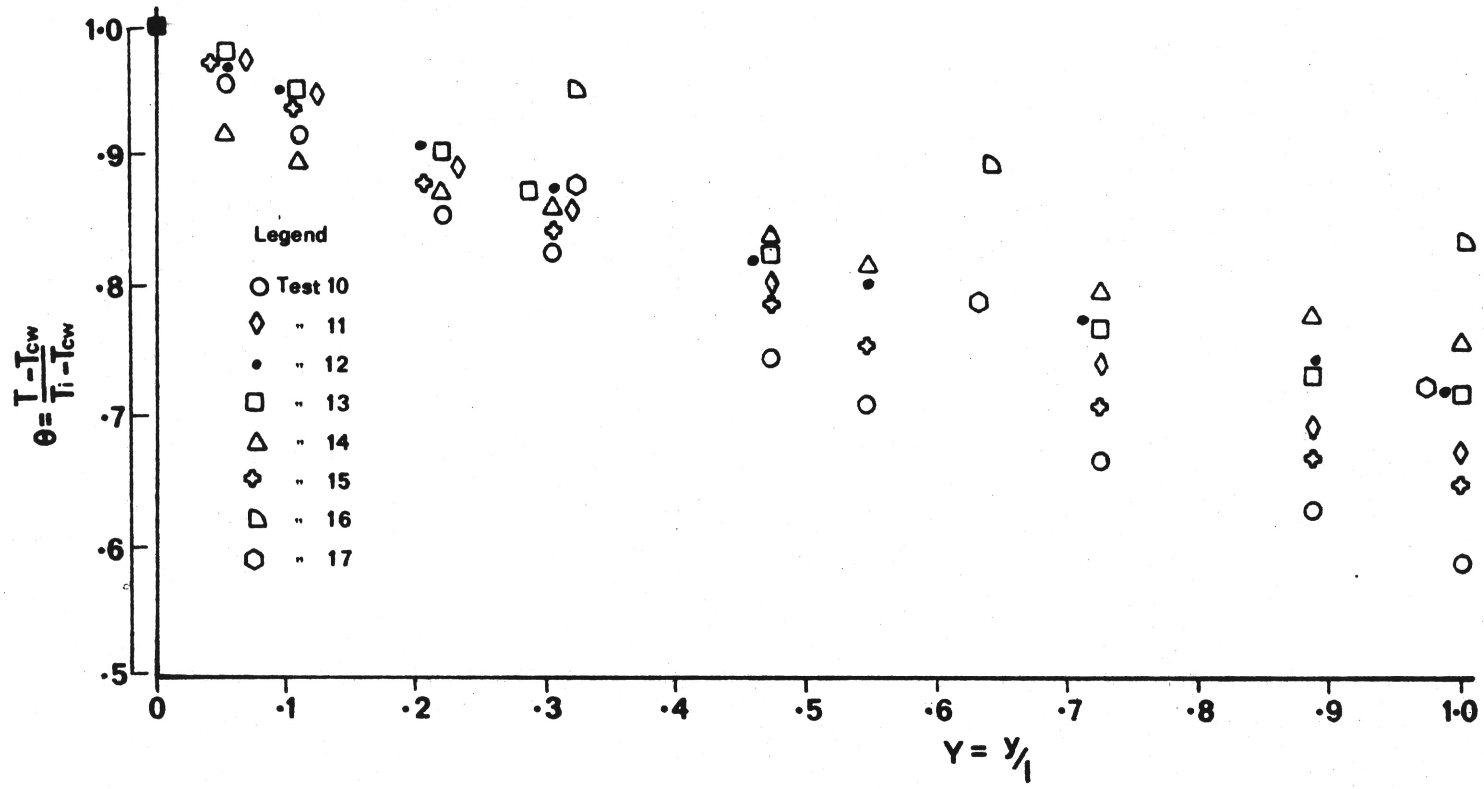

<u>Figure 6.3</u> Experimental results - dimensionless temperature versus the dimensionless distance from the inlet.

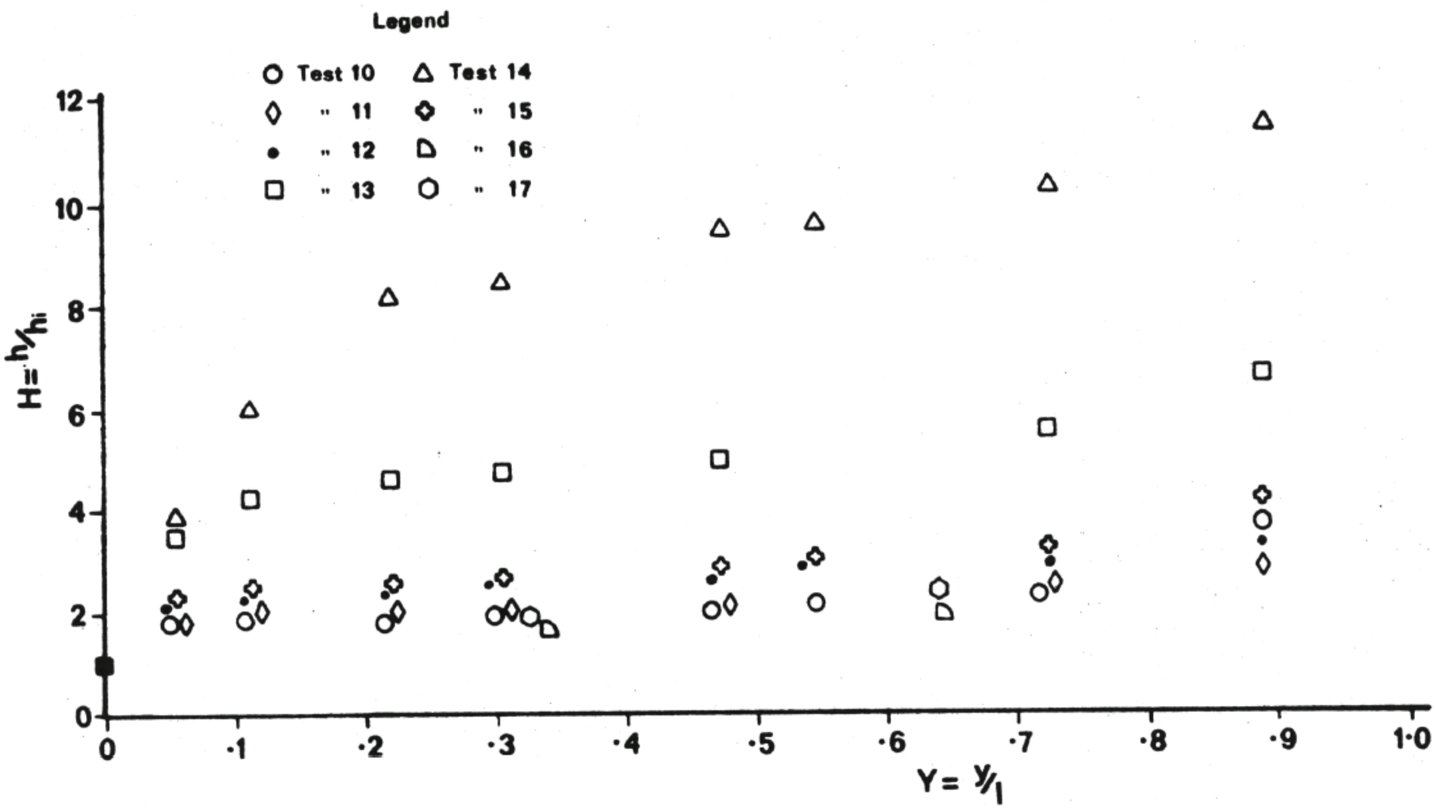

Figure 6.4 Experimental results - dimensionless interfacial depth versus the dimensionless distance from the inlet.

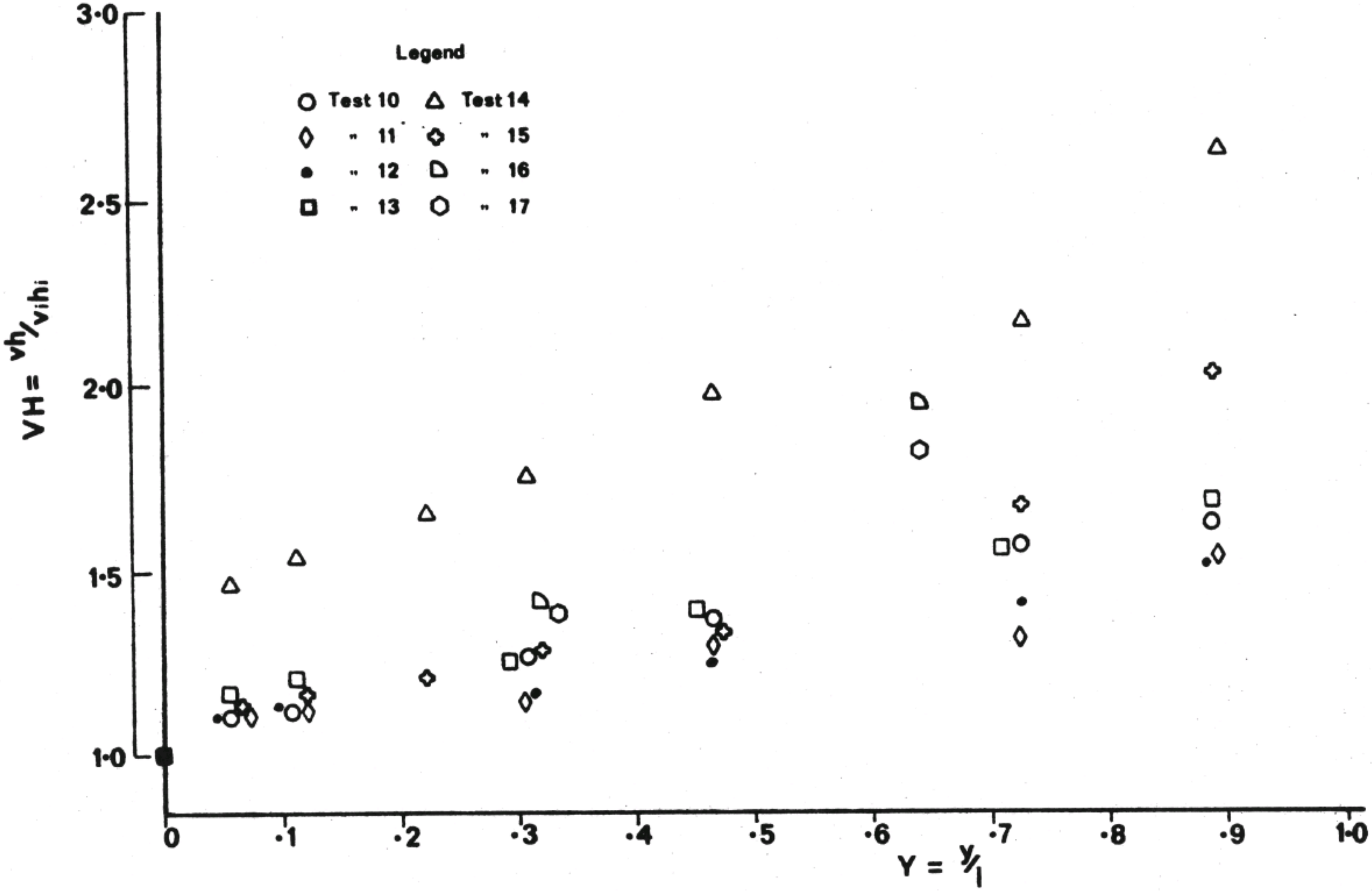

Figure 6.5 Experimental results - increase in the dimensionless surface flow per unit width with the dimensionless distance from the inlet.

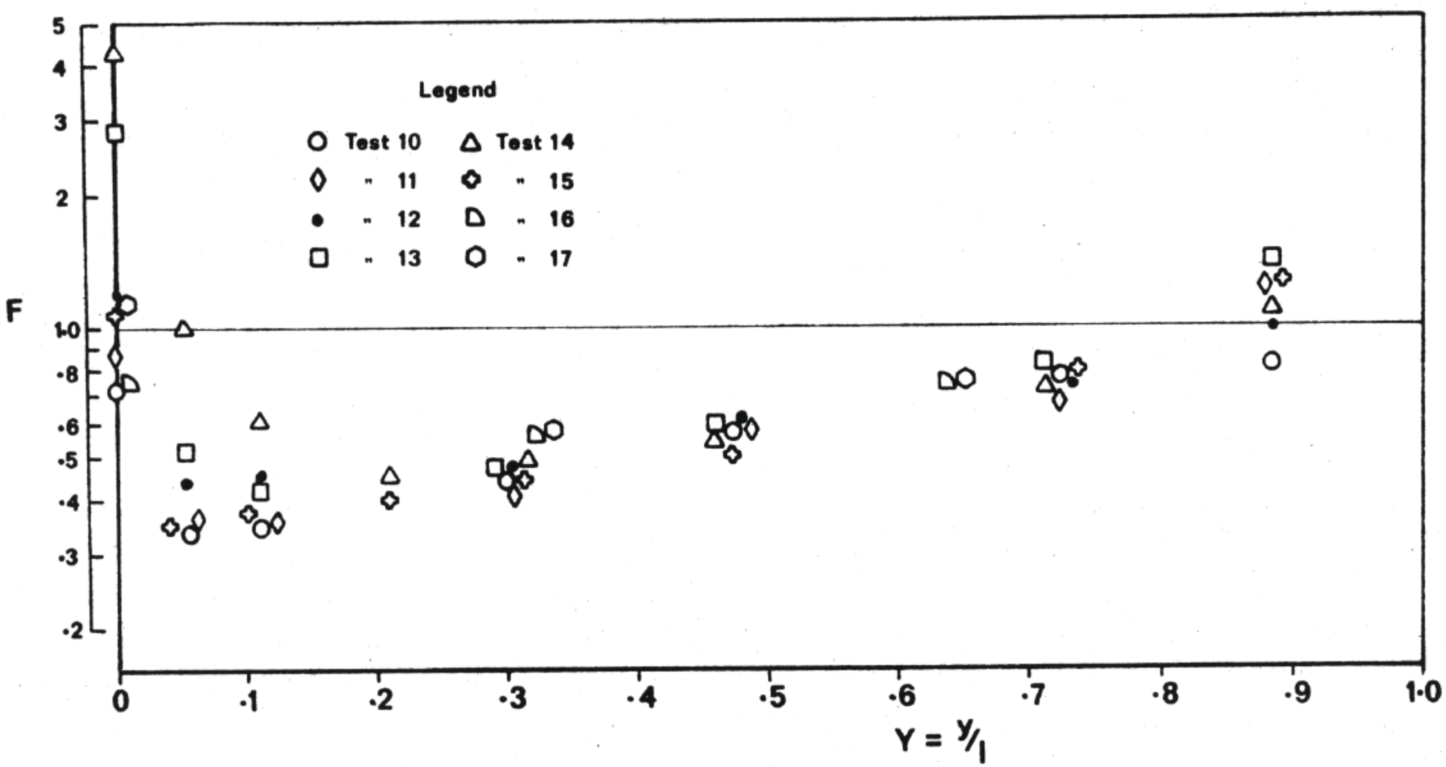

Figure 6.6 Experimental results - Densimetric Froude Number as a function of the dimensionless distance from the inlet.

where vi is the mean inlet velocity to the test section.

These parameters are shown in Figures 6.3 - 6.5 plotted against Y, the non-dimensional distance downstream from the inlet. The Densimetric Froude Number for the surface layer has been derived from these results and is shown in Figure 6.6.

In Tests 13 and 14 an internal hydraulic jump occurred downstream from the inlet. Photographs of dye injected into the surface layer indicate that in Test 13 the roller region of the jump extended from the inlet to a point approximately 300 mm (Y = 0.05) downstream from the inlet. The back flow associated with the roller region occurred above the interface and hence reduced the mean velocity of the surface layer in this region. In Test 14 the inlet Densimetric Froude Number was far higher and consequently the roller region of the jump was located further downstream, extending from a point just beyond the first measuring station (Y = 0.05) to just beyond the third measuring station (Y = 0.22). Velocity profiles obtained at the first three measuring stations indicated an initial large increase in volume flow and then a decrease at the fourth measuring station (Y = 0.3) spuriously suggesting de-entrainment at the end of the roller region. The back flow associated with the roller region was accounted for in determining the mean flow. The error in the mean flow obtained in the vicinity of the roller region is attributed to the velocity profiles being taken over a length of approximately 200 mm in which relatively high horizontal velocity gradients existed (this length is the distance between the initial and final photographed positions of the dye trace). Accordingly, the mean surface flow determined in the vicinity of the roller region was not the true mean at a vertical section. The internal hydraulic jump was associated with a significant drop in temperature (Figure 6.3) due to entrainment of ambient fluid, and this enabled a more realistic estimate of the mean flow to be calculated by performing a heat balance over a control volume bounded by the interface, the surface and two consecutive measuring stations. This approximation is derived in Appendix C and has been applied to the results presented for Test 14 in Appendix D.

6.2.1 Entrainment of Ambient Fluid into the Surface Layer

The volume flow per unit width increases with distance along the flume(Figure 6.5) indicating that although the Densimetric Froude Number was less than unity a significant amount of ambient fluid was being entrained from below the interface. The entrainment coefficient is defined as the ratio of the entrainment velocity (ve) to the mean velocity of the surface layer V, i.e.

$$e = \frac{Ue}{V} = \frac{1}{h}\frac{d(Vh)}{dy} \qquad (6.4)$$

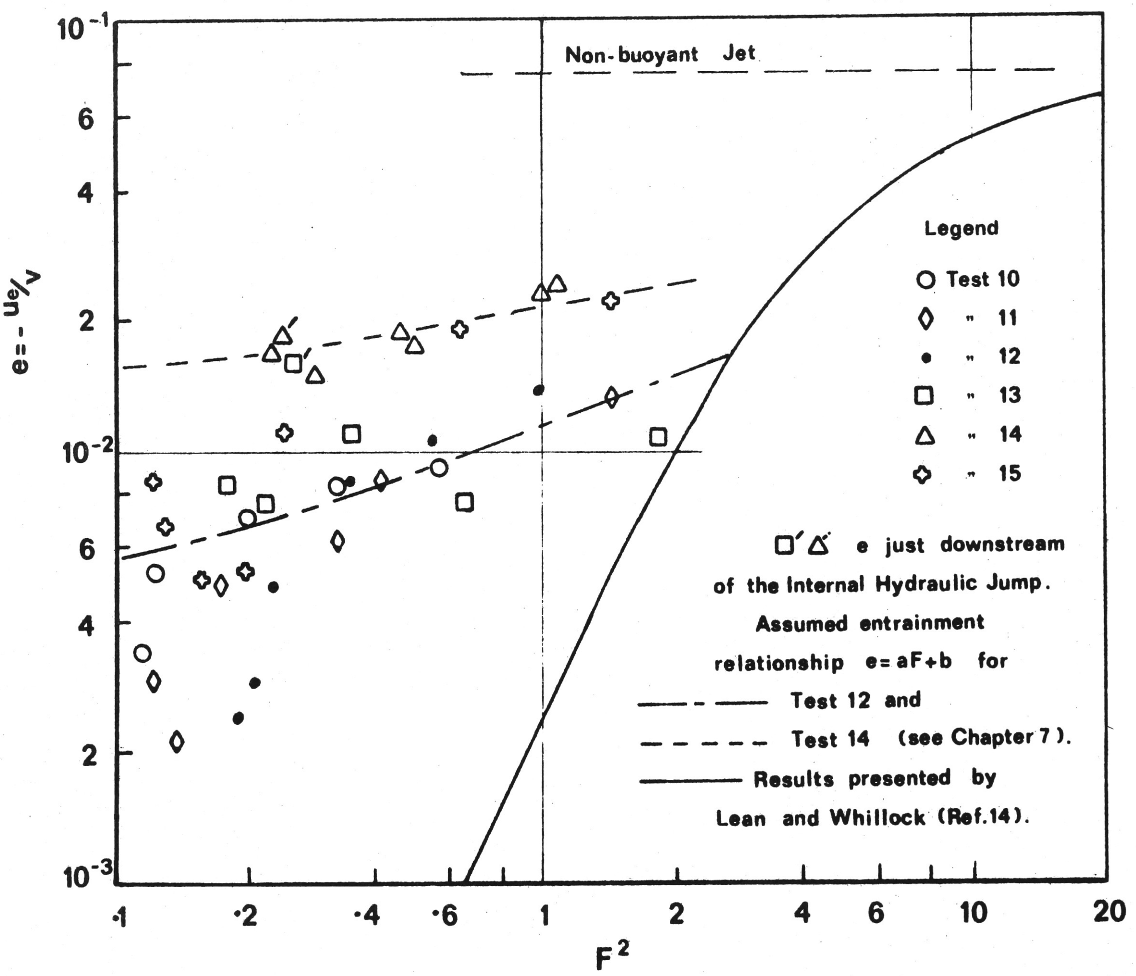

Figure 6.7 Experimental results - entrainment coefficient (e) versus the Densimetric Froude Number.

Values of e were determined from the experimental results by fitting a curve to each set of experimental values of VH shown in Figure 6.5 and measuring the gradient at the position of the known mean velocities. When the values of the entrainment coefficient are plotted against the Densimetric Froude Number (Figure 6.7) the values derived from the present investigation are seen to be generally greater than those implied by the results of Ellinson and Turner and of Lofquist as presented by Lean and Whillock(14). This marked increase in the entrainment coefficient is attributed to the convective action within the surface layer causing capture of ambient fluid from below the interface. No definite trend is apparent between tests although it appears that the entrainment coefficient is greater just downstream of the internal hydraulic jump than is the case for similar Densimetric Froude Numbers in the absence of a jump (Figure 6.7, Tests 13 and 14). Dornhelm et. al(5) found that for some inlet conditions the turbulence intensity in a buoyant three-dimensional jet increased to a maximum value and then decreased again with distance downstream from the inlet. This they attributed to some disturbance such as an internal hydraulic jump at the interface, although the existence of an internal hydraulic jump was not verified directly. The above results are consistent with these observations, with the increased turbulence resulting in a higher rate of entrainment of ambient fluid.

Vertical profiles of temperature obtained during field measurements on a cooling pond at Maitland, N.S.W.(6), showed the temperature gradient across the interface to be less than those obtained in the laboratory experiments, indicating that heat tends to diffuse across the interface. The relatively high entrainment coefficients found in the laboratory experiments are attributed to the convective motion in the surface layer being able to penetrate into this diffusion zone, capturing fluid and hence sharpening-up the interface. This phenomena could be absent at the lower heat transfer rates from the surface in full scale cooling ponds.

6.2.2 Temperature Distribution

The temperature distribution along the length of the pond is governed by the heat transfer away from the surface and by the entrainment of fluid into the surface layer. Entrainment of the cooler fluid into the surface layer results in a drop in the mean temperature and consequently reduces the rate of heat transfer away from the surface. This is illustrated by comparing the temperature distributions for Tests 14 and 15 (Figure 6.3) which have similar heat transfer coefficients. In Test 14 the temperature was initially decreased by the relatively larger entrainment of cooler fluid before the internal hydraulic jump (due to the high inlet Densimetric Froude Number) while Test 15 has a lower inlet Densimetric Froude Number and consequently the inlet was inundated. Although the inlet conditions were such that a density jump occurred in Test 13, a large decrease in the temperature excess similar to that in Test 14 was not observed. This is attributed to the entrainment zone of the density jump being suppressed by the roller region which was attached to the inlet.

6.2.3 Densimetric Froude Number

Within experimental accuracy the distribution of the Densimetric Froude Number with distance from the inlet (Figure 6.6) appear to lie on the same curve for Tests 10, 11, 12 and 15 in which the inlet was inundated. Where an internal hydraulic jump occurred (Tests 13 and 14) the distribution of the Densimetric Froude Number with distance from the inlet collapses onto the same curve downstream of the jump. This is not surprising since the flow at the inlet is governed by the downstream controls which, in this case, are the interfacial and wall shear stress (a function of the Reynolds Number), the heat transfer coefficient and, to some extent, the distance to the end wall. All of these factors were of the same order of magnitude for the abovementioned tests. Tests 16 and 17 were carried out in a shorter flume and at lower Reynolds Numbers with the result that the Densimetric Froude Number, for an equivalent non-dimensional distance downstream, was greater in magnitude.

The Densimetric Froude Number increases with distance downstream of the inundated inlet or of the internal hydraulic jump. Values calculated at the last measuring station ($Y = 0.89$) indicate that in some cases the Densimetric Froude Number becomes greater than unity as the downstream boundary is approached.

As $Y \rightarrow 1$,

$$\frac{\Delta\rho}{\rho} \rightarrow 0$$

$$V \rightarrow 0$$

and the interfacial depth $h \rightarrow \infty$.

Consequently the Densimetric Froude Number becomes indeterminate at the end wall. Experimental results indicate

$$F \rightarrow \infty$$

which could be the extrapolation from a buoyant to non-buoyant flow. The Densimetric Froude Number was found from -

$$F = \frac{Q}{\sqrt{\frac{\Delta\rho}{\rho} \; g \; h^3}} \tag{6.5}$$

where Q is the volume flow/unit width;

and the accuracy of determining the interfacial depth at the last measuring station was doubtful due to the instability of the interface and the low temperature differential across the interface. Assuming then that the interfacial depth was under-estimated at this point when the Densimetric Froude Number would be reduced and it could be postulated that as $Y \rightarrow 1$, $F \rightarrow 1$ which implies that the end wall acts as the control for the

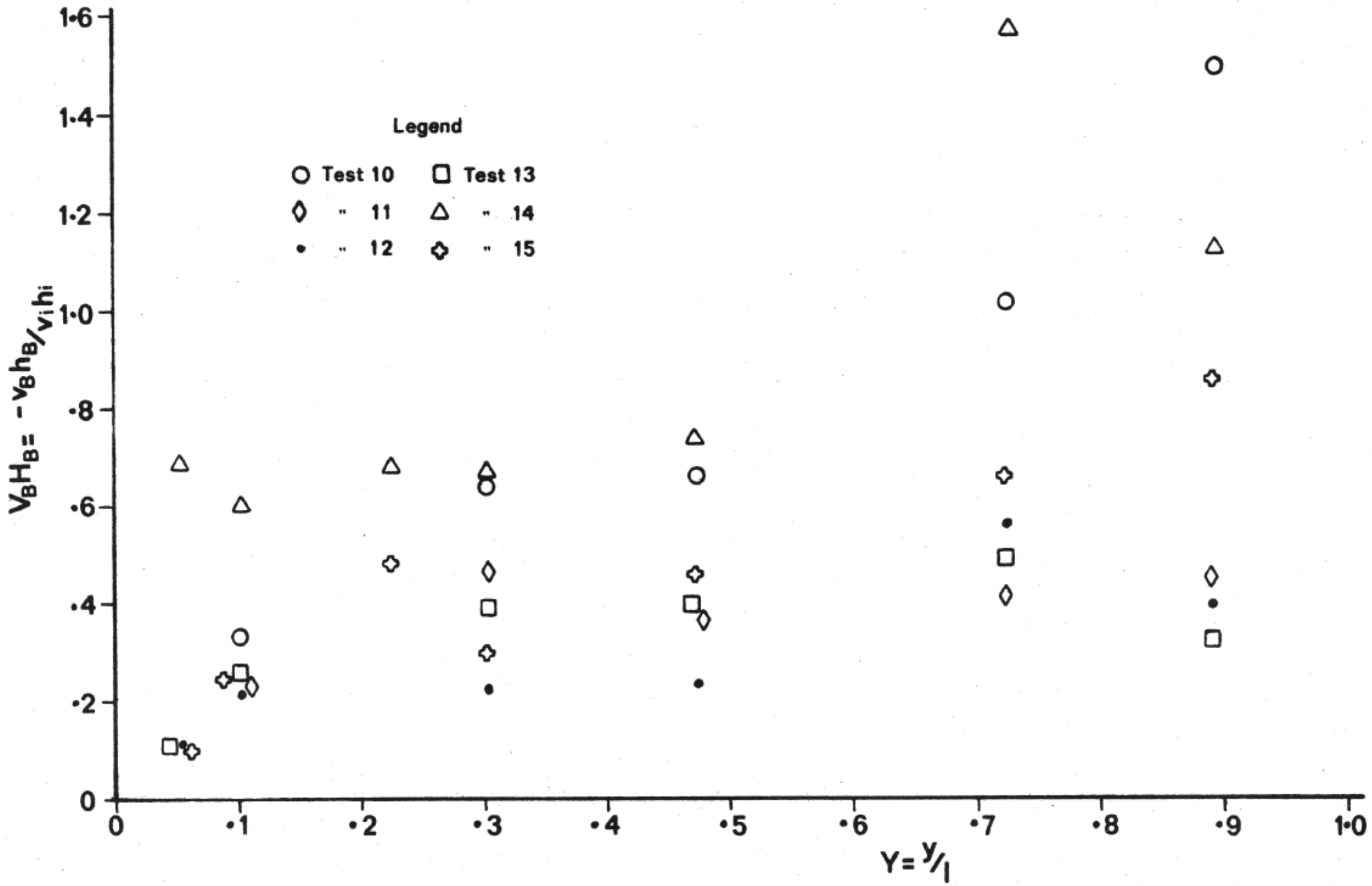

Figure 6.8 Experimental results - the dimensionless back-flow per unit width along the base of the flume versus the dimensionless distance from the inlet.

preceding flow. Both these interpretations seem possible in the light of the experimental results and will be pursued further in the following chapter.

6.3 Sub-Interfacial (Secondary) Flow

Once the thermal steady state had been achieved the flow below the interface formed the recirculating eddy shown diagrammatically in Figure 6.2(b). The surface layer, on reaching the end wall of the flume, flowed down towards the outlet where part of the flow passed out of the test section, the remainder flowing back along the base of the flume to form a recirculating eddy below the interface. The reverse flow along the base of the flume has been termed the "backflow" while the flow below the interface, but in the same direction as the surface flow, has been termed the "shear flow". The recirculating eddy is partly driven by the shear at the interface and partly by pressure gradients to provide replenishment of fluid entrained from the shear flow into the surface layer.

The shear flow and backflow were obtained by integrating the centre line velocity profile over the respective depths. They are shown plotted against the non-dimensional length in Figures 6.8 and 6.9. The absolute values of these flows should be viewed with caution since the flow in the recirculating eddy was not uniform across the flume. Figure 6.10 shows the profiles of vertical velocity taken at the centre of the flume's width and 50 mm either side of the centre for the fifth measuring station during Test 10. They

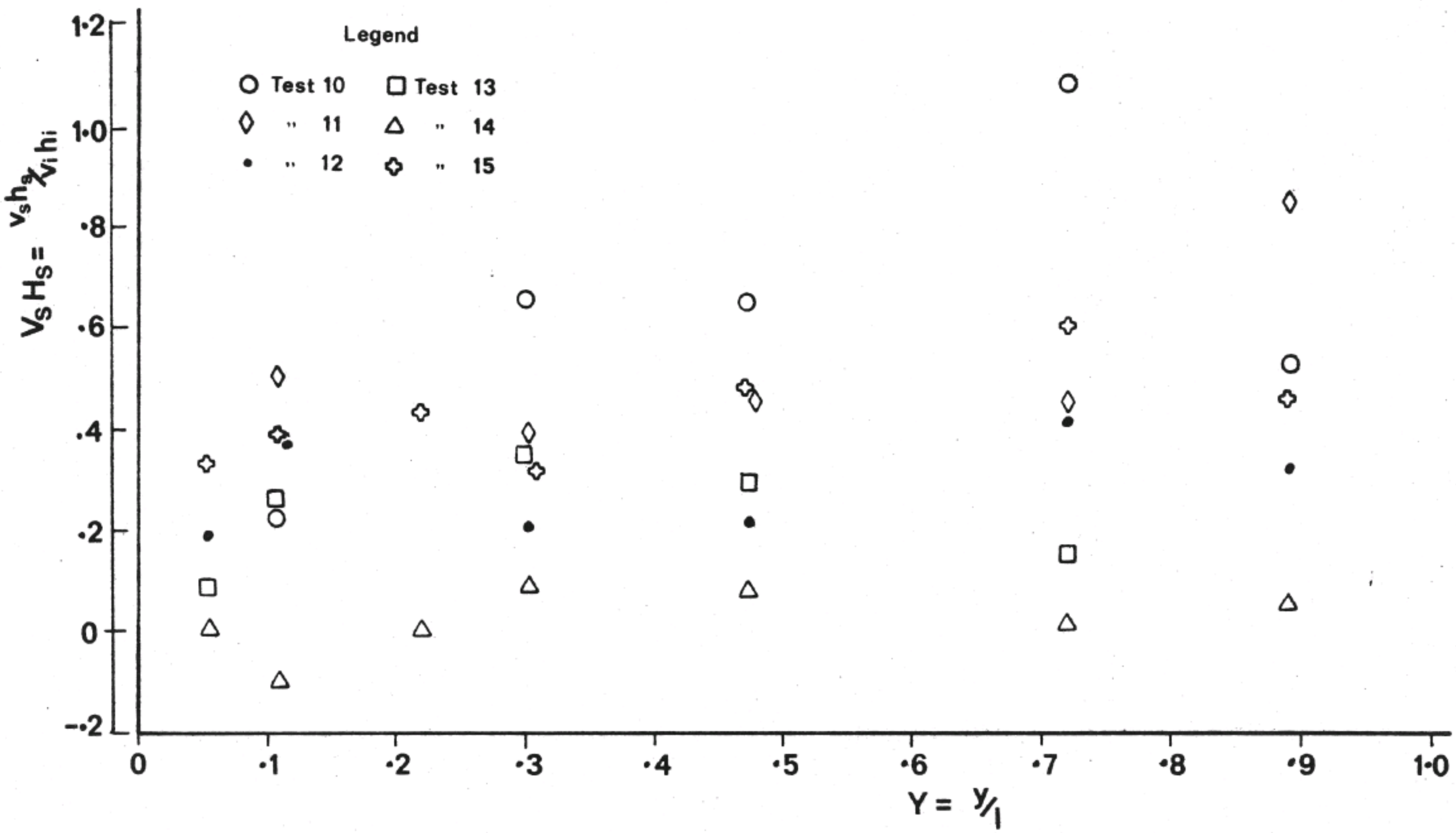

<u>Figure 6.9</u> Experimental results - dimensionless shear flow per unit width versus the dimensionless distance from the inlet.

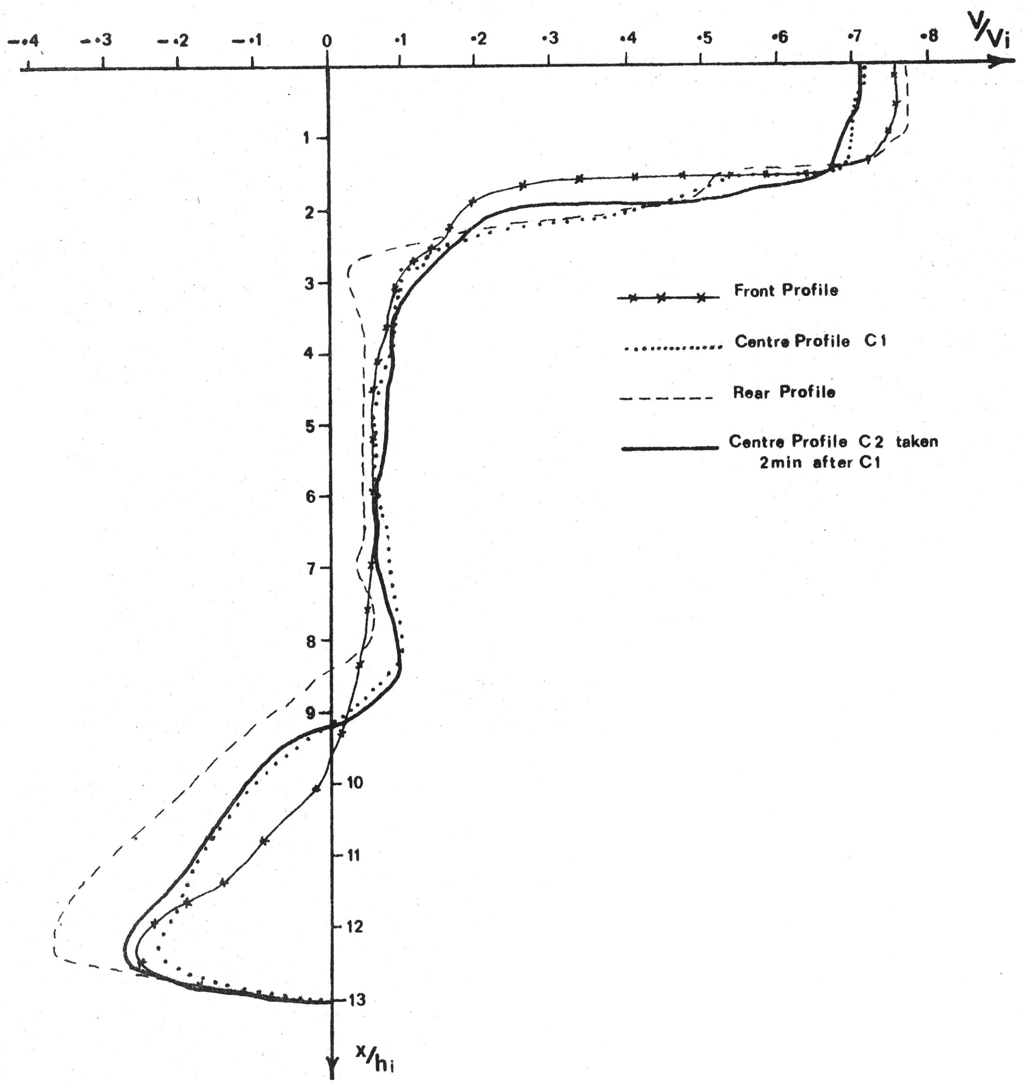

Figure 6.10 Experimental results - comparison of the vertical profiles of velocity measured at the centre of the flumes width and 50 mm either side of the centre. The profiles were taken at the sixth measuring station during Test 10.

show that the backflow was more pronounced along the rear wall and less pronounced towards the front wall, while the shear flow has the opposite tendency. The same trend was observed in all tests. The variation across the flume became more pronounced as the backflow approached the inlet end of the flume. This seems to suggest that it is a characteristic of the flow rather than a boundary effect.

The mean flow at any cross-section (calculated from the velocity profiles at that section) was found to be consistent from one profile to the next provided that the time interval between obtaining the profiles was small, but varied considerably when two profiles were obtained at a larger time interval. It was concluded that the flow below the interface was unsteady and varied according to the conditions dictated by the flow at the downstream end of the flume. The unsteadiness in the resultant sub-interfacial flow was also demonstrated by the intermittent appearance of a reverse eddy under the inlet. This eddy was detected in the velocity profiles obtained at the first two measuring stations.

The backflow decreases as it approaches the inlet end of the flume (Figure 6.8), the deficit in flow being transferred into the shear flow region. However, the shear flow does not reflect this gain with increase in distance from the inlet but remains reasonably constant (Figure 6.9) because of the entrainment of fluid from this region into the surface flow.

The high entrainment rate in the vicinity of the inlet for Test 14 is reflected in the increase in the backflow and a corresponding decrease in the shear flow. In one preliminary test run where the inlet Densimetric Froude Number was increased to 10 (as compared to 4.25 for Test 14) the entrainment volume required for the surface flow was so high that the shear flow disappeared altogether and the interface divided the surface layer from the backflow. Unfortunately, the turbulence in the surface layer prevented velocity profiles being obtained with the method used, and the test was abandoned. It would appear that in such situations (i.e. when the Densimetric Froude Number was high or the total depth of the flume reduced) the requirements of fluid to satisfy the entrainment at the inlet could generate additional shear at the interface and consequently act as an additional control on the surface flow. For example, the backflow in increasing the interfacial shear, would tend to cause the internal hydraulic jump to occur further upstream. This would result in a reduction in the fluid required for entrainment and the backflow would consequently be reduced. The process would eventually reach equilibrium. It is concluded therefore that under certain conditions the physical depth of a cooling pond would act as a control on the surface flow.

6.4 Experimental Errors

The main source of errors in the experimental investigation was the measurement of the mean velocity in the surface layer. It is estimated that the average flow per unit width determined from the velocity profiles is within 10% of the true flow per unit width when allowance is made for the boundary layer along the side walls.

The interfacial depth was obtained from the temperature profiles. To reduce the error introduced by the thermal inertia of the probe the interfacial depth was averaged from two profiles recorded while traversing in different directions. The interface, however, was disturbed by the convective action in the surface layer and consequently the average interfacial depth varied from profile to profile. This error is estimated to be in the order of ±3% where the temperature differential across the interface was large, and up to ±6% at the downstream end of the flume where the temperature differential was small and the interfacial disturbance high.

The Densimetric Froude Number was determined from Equation 6.5 and consequently is largely affected by the accuracy of the interfacial depth. The density difference $\Delta\rho$ was determined from the temperature difference across the interface and therefore was only dependent upon the relative accuracy of measuring instruments and not the absolute calibration. This error again becomes more pronounced as the temperature differential becomes smaller. An estimated error bound was 2% to 5% depending on the position along the flume. Consequently the error in the Densimetric Froude Number is quite large and could vary by 17% of the calculated value near the inlet to as high as 40% at the last measuring station. This could explain the variation between tests in the values of F calculated at the last measuring station ($Y = 0.89$) and throws some doubt on the implication that $F \rightarrow \infty$ as $Y \rightarrow 1$.

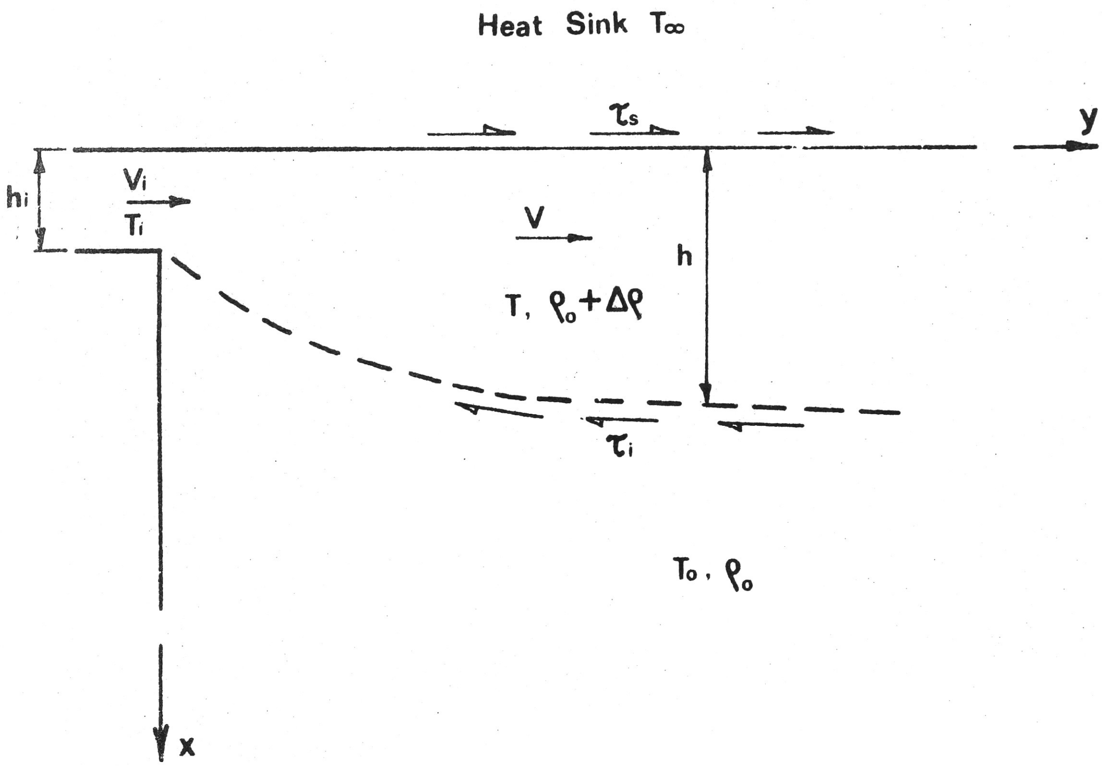

Figure 7.1 Surface buoyant jet model - definition sketch.

7. COMPARISON OF EXPERIMENTAL RESULTS WITH THE MATHEMATICAL MODEL PROPOSED BY KOH AND FAN:

7.1 Mathematical Model

7.1.1 Governing Equations

Koh and Fan(13) derived a mathematical model, including the effects of heat transfer from the surface, entrainment of ambient fluid and interfacial shear, for a two-dimensional surface buoyant jet. The model was reduced to a set of one-dimensional equations by assuming the form of the vertical distribution of velocity and temperature. The governing equations, expressed in terms of the co-ordinates defined in Figure 7.1, are -

Continuity

$$\frac{d}{dy}(Vh) = \frac{e}{\alpha} V \tag{7.1}$$

Momentum

$$\frac{d}{dy}(V^2h) = \alpha_1 \frac{d}{dy}(\Delta\rho h^2) - \alpha_2 (\tau_s - \tau_i) \tag{7.2}$$

Energy

$$\frac{d}{dy}(\Delta\rho hV) = -\alpha_2 H \tag{7.3}$$

where e is the entrainment coefficient,

τ_s is the surface shear stress,

τ_i is the interfacial shear stress and

H is proportional to the rate of heat loss from the surface.

α, α_1 and α_2 are constants derived from the assumed vertical distributions of velocity and temperature. The results from the experimental investigation (Chapter 6) indicate that the velocity and temperature distributions may be considered uniform across the jet with a step change at the interface. The numerical values of the α's are accordingly(13) -

$$\alpha = 1$$

$$\alpha_1 = \frac{-g}{2\rho_o}$$

$$\alpha_2 = 1$$

The density difference $\Delta\rho$ is a function of the temperature and may be expressed as -

$$\Delta\rho = \rho_o \beta \; (To - T) \tag{7.4}$$

where β is the coefficient of thermal expansion and

To is the ambient fluid temperature below the interface.

To obtain a solution to the governing equations it is necessary to specify e, τ and H as functions of the unknowns V, h and the temperature T. The relationship between these parameters and the unknowns differ from those used by Koh and Fan due to the boundary conditions imposed by the experimental rig. However, the general form of the relationship as used by them will be retained and the solution procedure remains the same.

7.1.2 The Entrainment Coefficient

Entrainment of ambient fluid into the surface layer was found to be significant in the sub-critical flow region $(F < 1)$ of the experimental investigation and hence some approximation was required to predict this entrainment rate in the model. It was assumed that the entrainment coefficient was a linear function of the Densimetric Froude Number for $F < 1$, i.e.

$$e = a\,F + b \tag{7.5}$$

The constants a and b were chosen to suit the experimental results.

The relationship proposed by Koh and Fan, from Ellison and Turners results, was used for the flow region where $F > 1$.

7.1.3 Surface Heat Transfer

The quantity H is defined as -

$$H = -D^1 \rho_o \beta \left.\frac{\partial T}{\partial x}\right|_{x=0}$$

where D^1 is the thermal diffusivity.

Substitution of 7.4 into the energy equation gives -

$$\frac{d}{dy}\,(ThV) = -D^1 \left.\frac{\partial T}{\partial x}\right|_{x=0}$$

The rate of heat transfer away from the surface can be expressed in terms of an overall heat transfer coefficient (k) such that -

$$D^1 \left.\frac{\partial T}{\partial x}\right|_{x=0} = \frac{k}{\rho_o C_p}\,(T - T_\infty) \tag{7.6}$$

where T_∞ is the temperature of the heat sink and

C_p is the specific heat of the fluid.

7.1.4 Shear Stress

In the experiments the motion of the surface layer was opposed by shear along the surface and side walls of the flume in addition to the shear at the interface. The combined shear stress can be expressed as -

$$\tau = \left[(1 + \frac{2h}{w})\ Cf_b + Cf_i \right] \frac{V^2}{2} \tag{7.7}$$

where Cf_b is the boundary shear stress coefficient and

Cf_i is the interfacial shear stress coefficient.

To estimate the relative magnitude of the boundary shear stress coefficient Blasius' smooth wall formulae for turbulent flow in conduits(18) was used -

$$Cf_B = \frac{0.079}{(NR)^{\frac{1}{4}}} \tag{7.8}$$

where the Reynolds Number (NR) was calculated using the hydraulic radius bounded by the solid boundaries and the interface. The interfacial shear stress coefficient was calculated using Harlemans formulation(1) -

$$Cf_i = \frac{11.3}{NR} \tag{7.9}$$

Koh and Fan assumed the shear stress to be of the form -

$$\tau i = \frac{\varepsilon V}{h} \tag{7.10}$$

where ε was the effective viscosity coefficient. This form was retained with ε being given from Equation 7.7 as -

$$\varepsilon = \left[(1 + \frac{2h}{w})\ Cf_b + Cf_i \right] \frac{Vh}{2}$$

Hence,

$$\varepsilon = \left[(1 + \frac{2h}{w}) \frac{0.079}{(NR)^{\frac{1}{4}}} + \frac{11.3}{NR} \right] \frac{Vh}{2} \qquad (7.11)$$

7.1.5 Non-Dimensional Equations for the Surface Jet of a Cooling Pond

Non-dimensionalising the equations with reference to the inlet conditions Vi, Hi and (Ti - To) such that -

$$v = \frac{V}{Vi}, \quad h^* = h/hi, \quad \theta = \frac{T - To}{Ti - To}$$

$$y^* = y/hi$$

and defining

$$Fi^2 = Vi^2/g \frac{\beta}{\rho_o} (Ti - To)hi, \quad R = \frac{hiVi}{\varepsilon} \quad \text{and}$$

$$K = \frac{k}{\rho_o C_p Vi} (1 - \frac{\theta\infty}{\theta})$$

the governing equations 7.1, 7.2 and 7.3 become, after dropping the superscript (*) -

$$\frac{d}{dy} (vh) = ev \qquad (7.12)$$

$$\frac{d}{dy} (v^2h) = - \frac{1}{2Fi^2} \frac{d}{dy} (\theta h^2) - \frac{1}{R} \frac{v}{h} \qquad (7.13)$$

$$\frac{d}{dy} (vh\theta) = - K\theta \qquad (7.14)$$

These equations are identical to those derived by Koh and Fan except that the effective viscosity coefficient (ε) and the non-dimensional heat transfer coefficient (K) are not constant over the solution field. Koh and Fan assumed that the fluid in the jet was eventually cooled to the temperature of the

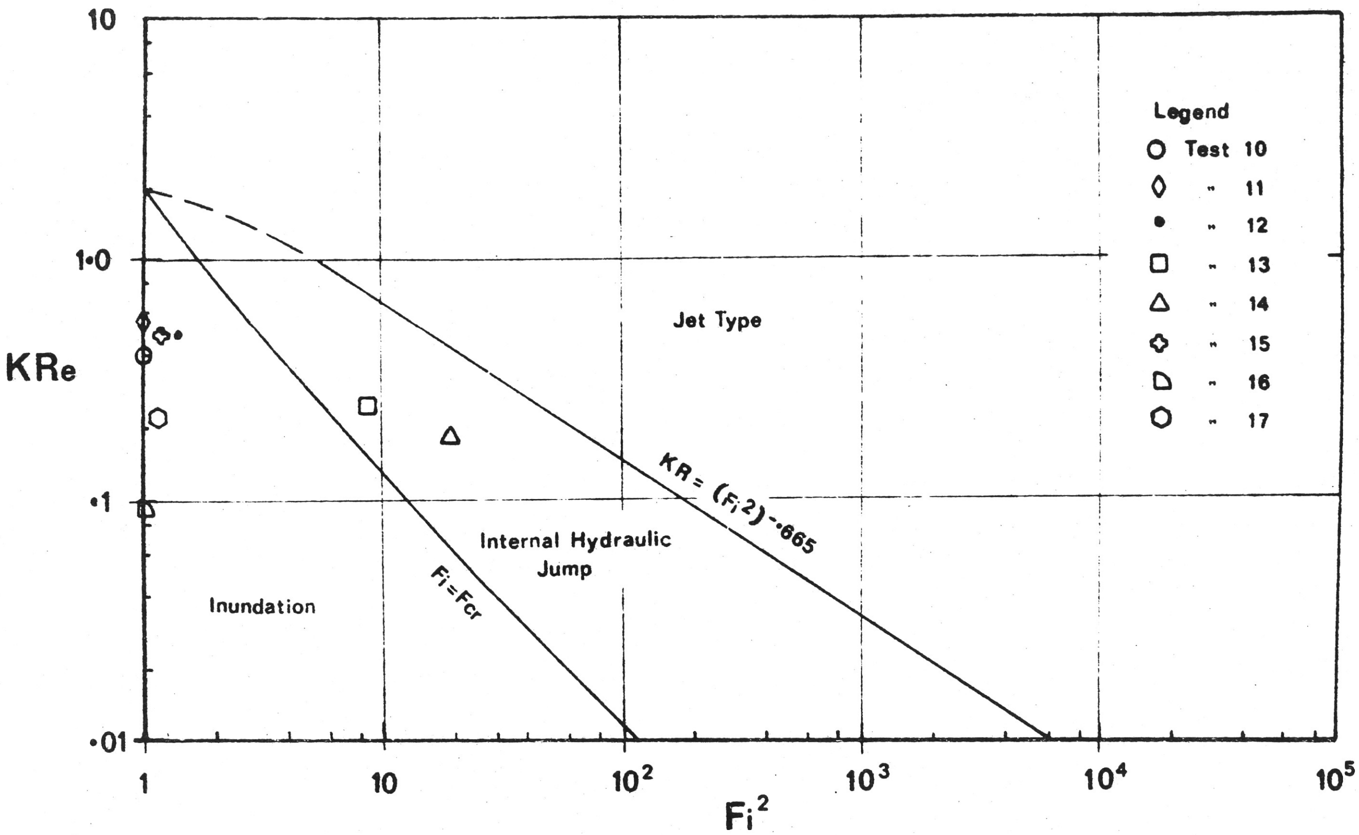

<u>Figure 7.2</u> The flow pattern expected in a surface buoyant jet as a function of the inlet parameters - Koh and Fan (13).

heat sink, and consequently the non-dimensional heat sink temperature ($\theta\infty$) was zero. This, in general, does not occur within the confines of a cooling pond.

Equations 7.12 to 7.14 can be rearranged to give -

$$\frac{d\theta}{dy} = -\frac{K\theta}{vh} - e\frac{\theta}{h} \tag{7.15}$$

$$\frac{dh}{dy} = \left[e(2 - 1/2\ Fi^2) - K/2\ Fi^2 v + 1/Rhv\right] \Big/ \left[1 - 1/Fi^2\right] \tag{7.16}$$

$$\frac{dv}{dy} = \frac{v}{h}\left[e - \frac{dh}{dy}\right] \tag{7.17}$$

and these equations can be solved numerically to give θ, h and v as a function of the distance from the inlet y.

7.2 Discussion of Koh and Fan's Solution

For $\theta\infty = 0$, $e = 0$ when $F^2 < 1$, and for ε and K constant over the region of solution, Koh and Fan found that three types of solution could exist, depending on the relative magnitude of Fi, R and K (see Figure 7.2).

(i) For -

$$KR > \left[Fi^2\right]^{-0.655}$$

A jet type solution would exist over the whole of the solution region.

(ii) For

$$\left[Fi^2\right]^{-0.655} < KR > F^2_{cr}$$

A jet type solution would exist up to some distance from the inlet where an internal hydraulic jump would form at $F = F_{cr}$ and the flow would become sub-critical.

(iii) For -

$$KR < F_{cr}^2$$

the inlet would be inundated and the resulting flow sub-critical.

On the assumption of zero entrainment within the internal hydraulic jump, the downstream conditions (y_2) after the jump can be expressed in terms of the conditions immediately upstream from the jump (y_1) by -

$$h_2 = \frac{h_1}{2}\left[\sqrt{1 + 8\,F_1^2} - 1\right]$$

$$v_2 = \frac{2v_1}{\sqrt{1 + 8\,F_1^2} - 1}$$

$$F_2^2 = \frac{8F_1^2}{\left[\sqrt{1 + 8F_1^2} - 1\right]^3}$$

$$\theta_2 = \theta_1 \tag{7.18}$$

Koh and Fan deduced from the solution to the governing equations in the sub-critical flow region (i.e. $e = 0$ and $F < 1$) that the internal hydraulic jump would occur when the Densimetric Froude Number just downstream from the jump was less than the critical Densimetric Froude Number, i.e.

$$F_2 < F_{cr}$$

where the critical Densimetric Froude Number was given by -

$$F_{cr} = \left(\frac{4}{RK} - 1\right)^{-2} \tag{7.19}$$

This is a necessary but not sufficient condition to locate the position of the internal hydraulic jump and the further assumption was made that the jump occurred at the furthermost location from the inlet. This corresponds to the least possible increase in depth and consequently the least energy loss across the jump.

In arriving at the relationship for the critical Densimetric Froude Number two other observations were made for the sub-critical flow region -

(i) $\frac{dh}{dy} > 0$ i.e. the depth is always increasing in the sub-critical flow region.

(ii) $F^2 < 1$ the Densimetric Froude Number in the region downstream of the jump is always less than unity.

When the downstream controls are such that the inlet is inundated the sub-critical inlet conditions can be found from by $Fi = F_{cr}$.

7.3 Solution of the Equations to the Modified Model

The modified equations describing the surface flow in the experimental investigation differ from those proposed by Koh and Fan only in the functional form of e, R and K. The general conclusions from Koh and Fan's investigation should therefore be applicable to the present model although the critical Densimetric

Froude Number for determining the position of, and downstream conditions just after, the internal hydraulic jump will differ. The observed surface flow form in the experimental investigation all lie in the same regions as predicted by Koh and Fan's theory (Figure 7.2).

It is interesting to note that although the inlet Densimetric Froude Number was less than unit for Tests 10, 11 and 16 the inlet was inundated and intrusion of ambient fluid into the inlet did not occur as postulated by previous workers(9). If it is initially assumed that intrusion would occur and the calculated inlet depth reduced to give a Densimetric Froude Number of unity at the inlet, the downstream controls on the subsequent flow predict inundation (see Figure 7.2) to a depth greater than the inlet depth. Intrusion of ambient fluid into the inlet would not be expected until the predicted inundated depth calculated by this method was less than the inlet depth.

7.3.1 Determination of the Critical Froude Number

Deriving a relationship for the critical Densimetric Froude Number from the governing equations (as was derived by Koh and Fan) for the conditions in the sub-critical flow region is difficult because the entrainment is not negligible in this region and hence equation 7.12 can not be solved analytically. Some insight can be gained into the effect of the entrainment on the value of F_{cr} by examining equation 7.16 with the restriction that $\frac{dh}{dy} > 0$ for $F < 1$. Expressing the non-dimensional heat transfer coefficient as -

$$K = K' \left(1 - \frac{\theta}{\theta_\infty}\right) \tag{7.20}$$

where K' is the mean heat transfer coefficient and is assumed to be constant over the solution region, it can be shown that for $dh/dy > 0$ -

$$\left(\frac{\theta - \theta_\infty}{\theta}\right) \frac{K'}{v} > e(4F^2 - 1) + \frac{2F^2}{Rhv} \tag{7.21}$$

where, by definition, θ_∞ is negative for heat transfer from the surface of the jet.

If the downstream conditions are such that the inlet is inundated then for the inlet conditions $\theta = v = h = 1$ equation 7.21 reduces to

$$(1 - \theta_\infty)K' > e(4Fi^2 - 1) + \frac{2Fi^2}{R} \tag{7.22}$$

The effect of the entrainment of ambient fluid into the surface layer on the restriction that $\frac{dh}{dy} > 0$ depends upon the value of Fi -

(i) for $1 > Fi^2 > 0.25$ the entrainment coefficient decreases the allowable Densimetric Froude Number which satisfies Equation 7.22 and

(ii) for $0.25 > Fi^2$ the entrainment coefficient helps satisfy equation 7.22 and hence increases the limiting value of the Densimetric Froude Number.

Using the inundated inlet conditions for Test 12, equation 7.22 is satisfied if $Fi < 0.74$. This criterion was well satisfied by the experimental results ($Fi = 0.4$). The temperature term dominates the left-hand side of equation 7.21 and hence if the condition described by equation 7.21 is satisfied at the inlet, it will be satisfied for the whole of the sub-critical flow region.

The second requirement satisfied by Koh and Fan's solution was that $F < 1$ at any point downstream from the internal hydraulic jump. It can be shown(13) that $\frac{dF^2}{dy}$, for any point in the solution region, is given by -

$$\frac{dF^2}{dy} = \left[3e + \frac{6F^2}{(2F^2+1)Rvh} - \frac{K}{v}\right]\frac{F^2+1}{2h(1-F^2)} \qquad (7.23)$$

and therefore, in the sub-critical flow region, F increases or decreases according to whether -

$\frac{K'}{v}$ is less than or greater than

$$\left(3e + \frac{6F^2}{(2F^2+1)Rhv}\right)\frac{\theta}{\theta - \theta\infty}$$

In particular for $\frac{dF}{dy} > 0$ and $F < 1$

$$\frac{K'}{v} < \left(3e + \frac{6F^2}{(2F^2+1)Rhv}\right)\frac{\theta}{\theta - \theta\infty} \qquad (7.24)$$

The right side of 7.24 is dominated by the temperature term and consequently decreases as y increases -

$$(\theta \rightarrow 0 \quad \text{as} \quad y \rightarrow L)$$

If the inlet is inundated and equation 7.24 is satisfied at $y = 0$, two possible conditions occur as $y \to L$ -

(i) Equation 7.24 is always satisfied and F increases as $y \to L$.

(ii) The right-hand side of equation 7.24 approaches K'/v until $\frac{dF}{dy} = 0$ and F then decreases for further increases in y.

If the first condition (i) is satisfied then equation 7.24 implies that $\frac{d(F^2)}{dy} \to \infty$ as $F \to 1$. This solution would be valid provided $F < 1$ for $y < L$.

If $F = 1$ for $y < L$ then equation 7.23 implies a discontinuous solution (i.e. for $F \to 1$ $\frac{dF}{dy} < 0$) and a transition from sub-critical to super-critical flow would be expected via an internal hydraulic jump. This would be possible only if the boundary conditions transmitted additional energy to the flow, and hence, for the present case it is not a possible solution. Therefore, the initial sub-critical Densimetric Froude Number must decrease so that $F < 1$ always in the sub-critical flow region, the limiting case being $F \to 1$ as $y \to L$.

An upper bound on the critcal Densimetric Froude Number is therefore the maximum Densimetric Froude Number just downstream of the internal hydraulic jump (or at the inlet if inundation occurs) which gives $F < 1$ for the remainder of the surface flow. This condition also corresponds to the minimum energy loss across the jump.

7.3.2 Solution of the Equations

Koh and Fan's numerical program(13) was modified to incorporate the functional dependence of e, ε and K (equations 7.5, 7.11 and 7.20). The governing equations were then solved for the inlet conditions defined by the experimental investigation. Two typical solutions are presented here, Test 12 representing the condition where the inlet was inundated and Test 14 where an internal hydraulic jump formed downstream of the inlet.

(a) Test 12

The critical Densimetric Froude Number (F_{cr}) for the inundated conditions at the inlet was obtained by progressively reducing Fi from the critical value given by Koh and Fan's solution (equation 7.19, $F_{cr}^2 = 0.49$) until $F < 1$ for $0 < y < L$. Figure 7.3 shows the variation of the Densimetric Froude Number with increase in distance from the outlet for $Fi > F_{cr}$, $Fi = F_{cr}$ and $Fi < F_{cr}$. For $Fi > F_{cr}$, $\frac{dF}{dy}$ was greater than zero over the whole solution region resulting in $F = 1$ for $y < L$. For $Fi = F_{cr}$, F initially increased to a maximum value and then decreased, the decrease being caused by a rapid increase in the interfacial depth as the distance from the inlet increased. This general form of the distribution was retained for $Fi < F_{cr}$ but the maximum value of F attained decreased as Fi was decreased until equation 7.24 was not satisfied at the inlet and $\frac{dF}{dy} < 0$ for $0 < y < L$.

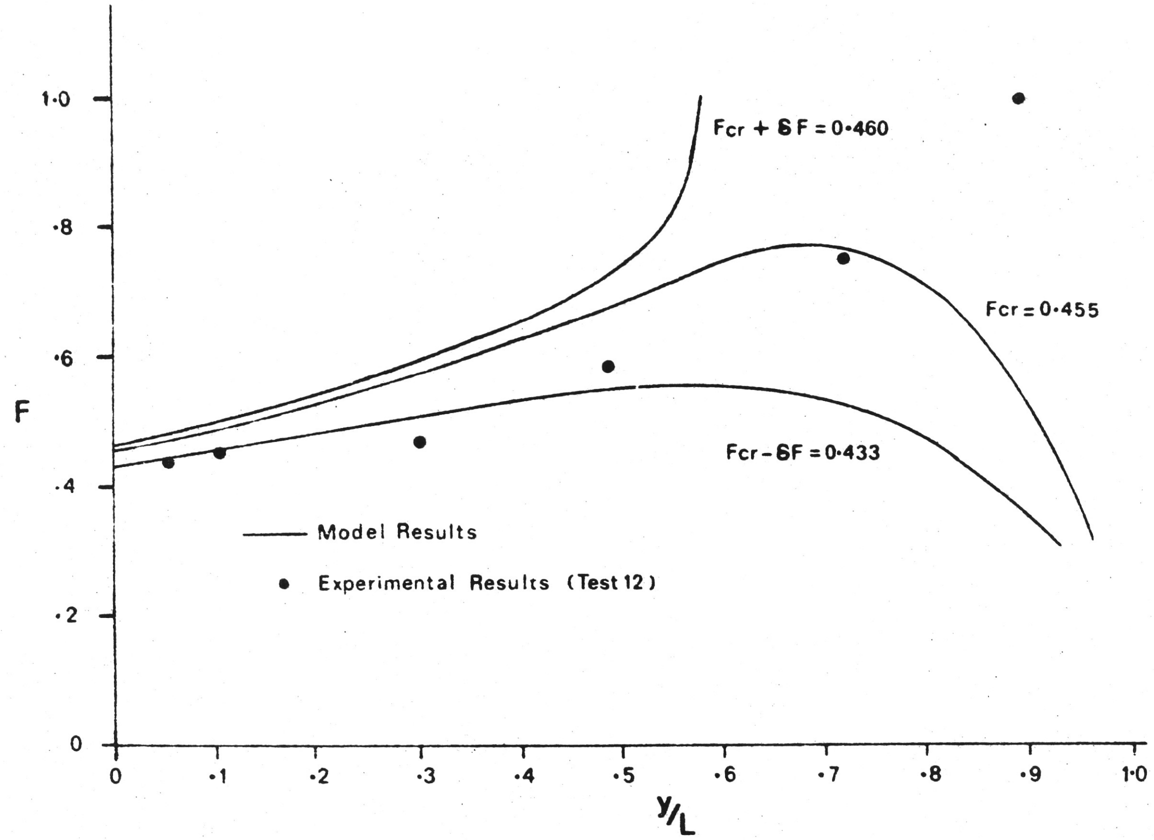

Figure 7.3 Surface buoyant jet model - Densimetric Froude Number versus the dimensionless distance from the inlet for Fi = Fcr, Fi = Fcr + δF and Fi = Fcr - δF. Fcr pertains to Test 12 where $e = (8.35\ F + 3) \times 10^{-3}$, $\theta_\infty = 2.46$, $k = 6.62 \times 10^{-5}$ m/sec, Re = 1200 and ε given by equation 7.11.

Variation in the assumed relationship giving e and ε only resulted in the magnitude of F_{cr} being altered, the general form of F versus y/L remaining the same as that shown in Figure 7.3.

The assumed form of the shear stress coefficient (equation 7.11) can not be justified from the experimental results. Blausius' formulae (7.8) was used as a first approximation to obtain the boundary shear stress coefficient. However, the Reynolds Numbers for the experimental investigation were low and therefore equation 7.11 could result in an under-estimate of the boundary shear stress. The interfacial shear stress was small in comparison with the boundary shear stress and the error in using the laminar flow interfacial shear stress coefficient proposed by Harleman (equation 7.9) would have little influence on the theoretical results.
It was found that the model gave better agreement with the experimental results when the total shear stress was increased by 30%, i.e.

$$\varepsilon_{actual} = 1.3\ \varepsilon \tag{7.25}$$

where ε was given by equation 7.11.

Figures 7.4, 7.5 and 7.6 show the longitudinal distribution of F, θ and h as calculated by the theory for the inlet conditions pertaining to Test 12. ε was calculated from

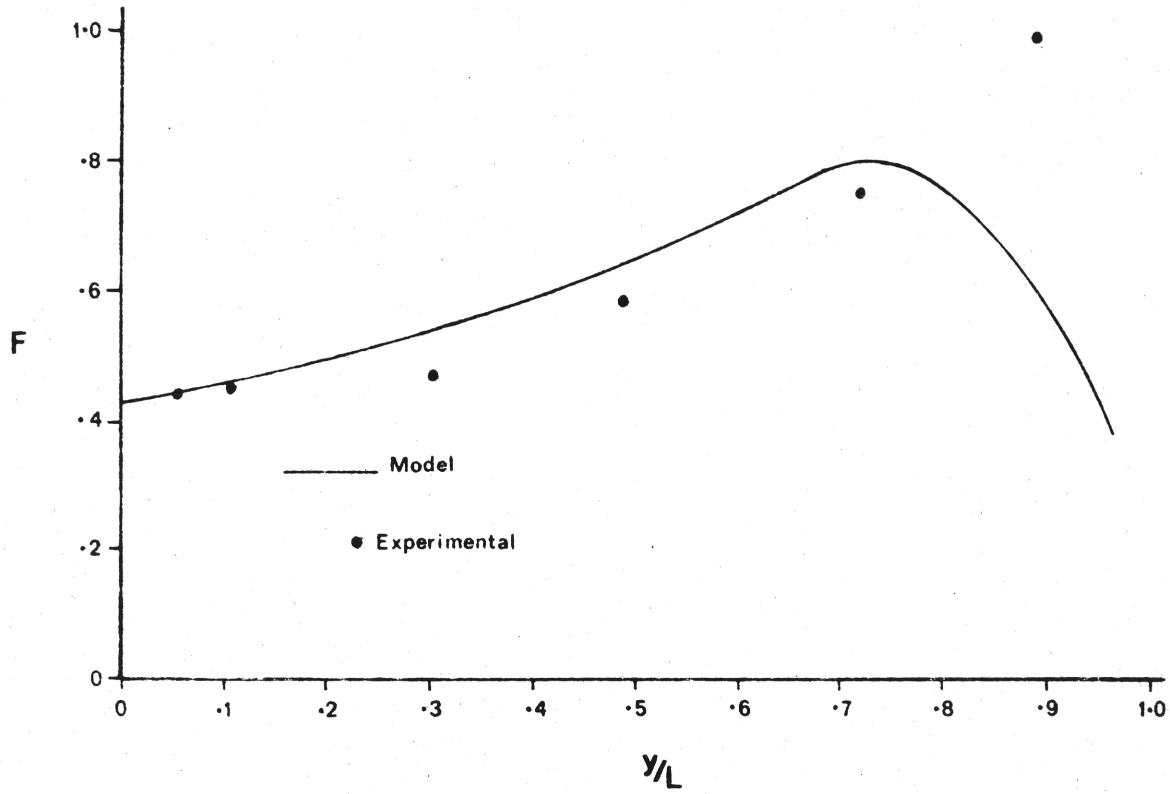

Figure 7.4 Densimetric Froude Number versus the dimensionless distance from the inlet. Comparison between the experimental results and the surface buoyant jet solution for Test 12. Solution parameters $e = (8.3F + 3) \times 10^{-3}$, $\theta_\infty = 2.46$, $k = 6.62 \times 10^{-5}$ m/sec, Re = 1200, $F_{cr} = .427$ and ε given by equation 7.25.

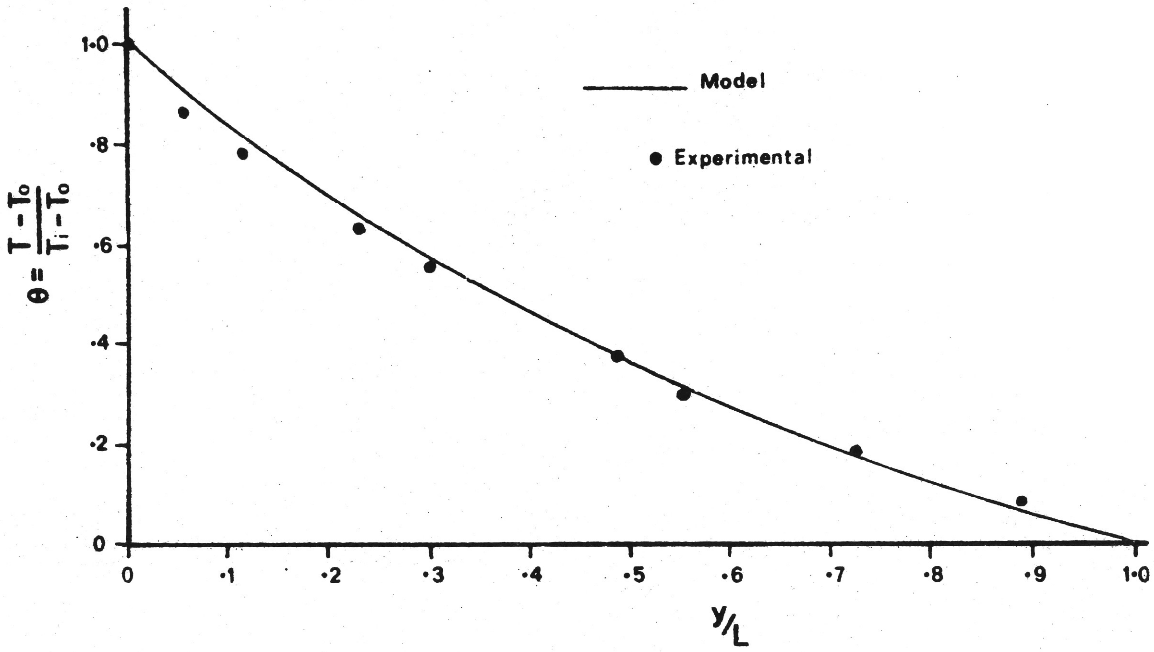

Figure 7.5 Dimensionless temperature versus dimensionless distance from the inlet. Comparison between the experimental results and the surface buoyant jet solution for Test 12. Solution parameters $e = (8.35F + 3) \times 10^{-3}$, $\theta_\infty = 2.46$, $k = 6.62 \times 10^{-5}$ m/sec, Re = 1200, Fcr = .427 and ε given by equation 7.25.

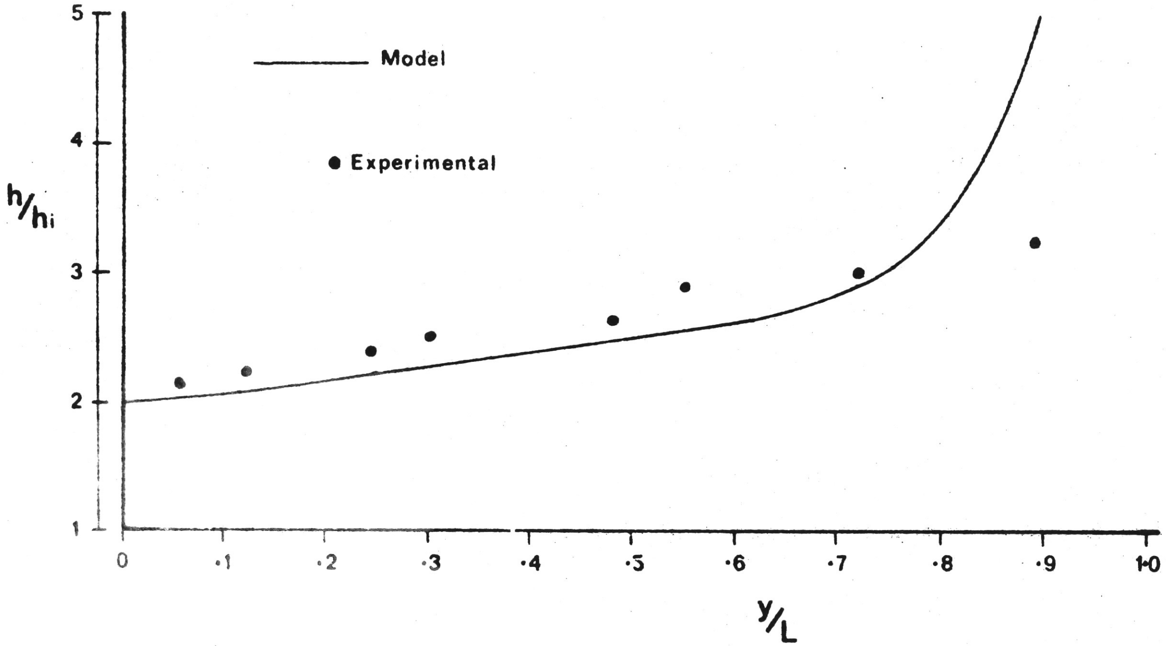

<u>Figure 7.6</u> Dimensionless interfacial depth versus the dimensionless distance from the inlet. Comparison between the experimental results and the surface buoyant jet solution for Test 12. Solution parameters $e = (8.35F + 3) \times 10^{-3}$, $\theta_\infty = -2.46$, $k = 6.62 \times 10^{-5}$ m/sec, Re = 1200, Fcr = .427, and ε given by equation 7.25.

equation 7.25 and the entrainment coefficient was given by -

$$e = (8.35\ F + 3) \times 10^{-3} \qquad \text{(see Figure 6.7)}$$

The theory shows good agreement with the experimental results with the exception of the interfacial depth, and consequently the Densimetric Froude Number, in the latter stages of the solution ($y/L > 0.75$). For h to remain bounded as $F \rightarrow 1$, the numerator of equation 7.16

$$\frac{K}{2F^2v} - e(2 - \frac{1}{2F^2}) - \frac{1}{Rhv}$$

must decrease as the denominator -

$$\frac{1}{F^2} - 1$$

decreases.

As $F \rightarrow 1$ and $\theta \rightarrow 0$

$$e(2 - \frac{1}{2F^2}) \rightarrow 1.5\ e$$

$$\frac{K}{2F^2v} = \frac{K'}{2F^2v}\left(\frac{\theta - \theta\infty}{\theta}\right) \rightarrow \infty$$

$$\frac{1}{F^2} - 1 \rightarrow 0$$

The entrainment coefficient (e) has an upper bound of 0.075 corresponding to a non-buoyant turbulent jet(7) and hence for h to remain bounded, $R \rightarrow 0$.

The local Reynolds Number is given by -

$$R = \frac{vh}{\varepsilon}$$

and since vh is increasing due to the entrainment of ambient fluid, for $R \to 0$, $\varepsilon \to \infty$, which implies (equation 7.11) that the resistance to flow increases as $y \to L$. Therefore the discrepancy between the models' predictions and the experimental results would be due to the influence of the end wall and to the underlying flow becoming the dominant controls on the surface flow as the influence of the inlet momentum decreases with increase in distance from the inlet.

The experimental results support the assumption that the critical Densimetric Froude Number is the maximum which gives $F < 1$ in the sub-critical flow region and hence corresponds to the minimum energy loss in the transition from super-critical to sub-critical flow.

(b) Test 14

In Test 14 the flow was initially of the jet type and transferred to a sub-critical flow by means of an internal hydraulic jump. The entrainment of ambient fluid into the surface flow was found to be higher in this test than in the tests where the inlet was inundated (see Figure 6.6). e was approximated by -

$$e = (8.35\ F + 13) \times 10^{-3} \qquad (7.26)$$

in the theoretical investigation. F_{cr} was obtained by calculating the Densimetric Froude Number that would be applicable

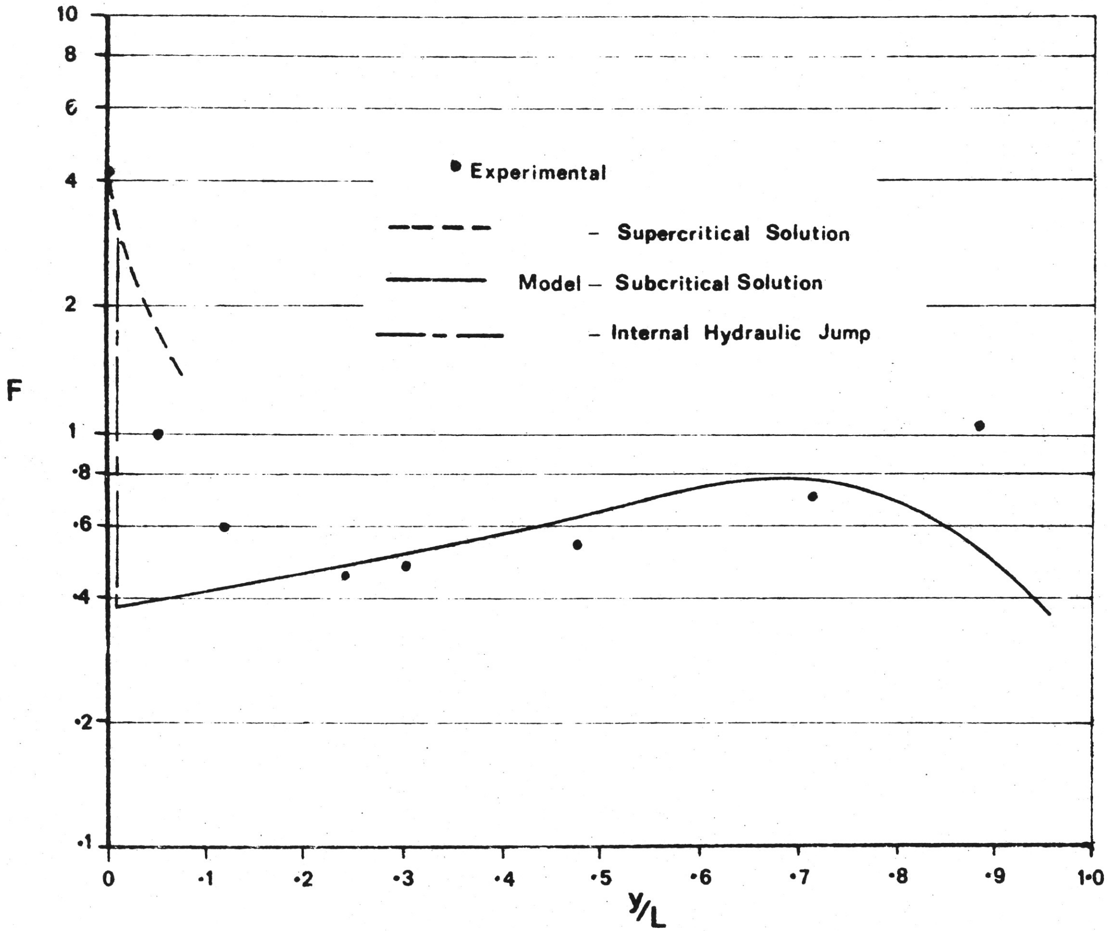

Figure 7.7 Densimetric Froude Number versus the dimensionless distance from the inlet. Comparison between the experimental results and the surface buoyant jet solution for Test 14. Solution parameters $e = (8.35F + 13) \times 10^{-3}$, $\theta_\infty = -3.05$, $k = 5.33 \times 10^{-5}$ m/sec, Re = 1085, Fi = 4.2 and ε given by equation 7.25.

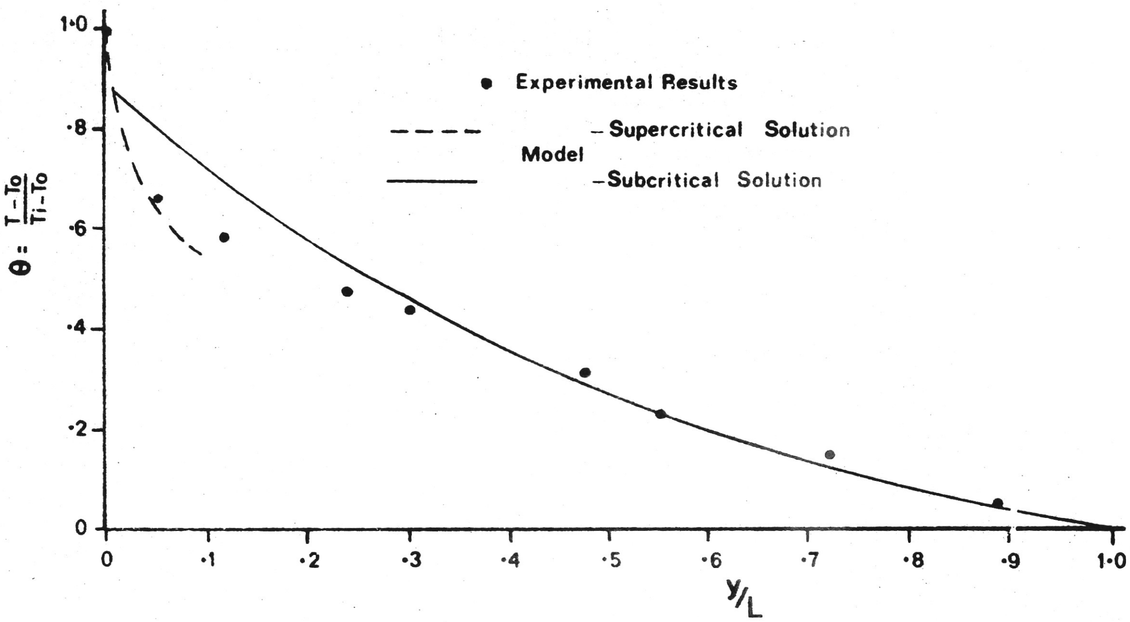

Figure 7.8 Dimensionless temperature versus the dimensionless distance from the inlet. Comparison between the experimental results and the surface buoyant jet solution for Test 14. Solution parameters $e = (8.35F + 13) \times 10^{-3}$, $\theta_\infty = -3.05$, $k = 5.33 \times 10^{-5}$ m/sec, Re = 1085, Fi = 4.2 and ε given by equation 7.25.

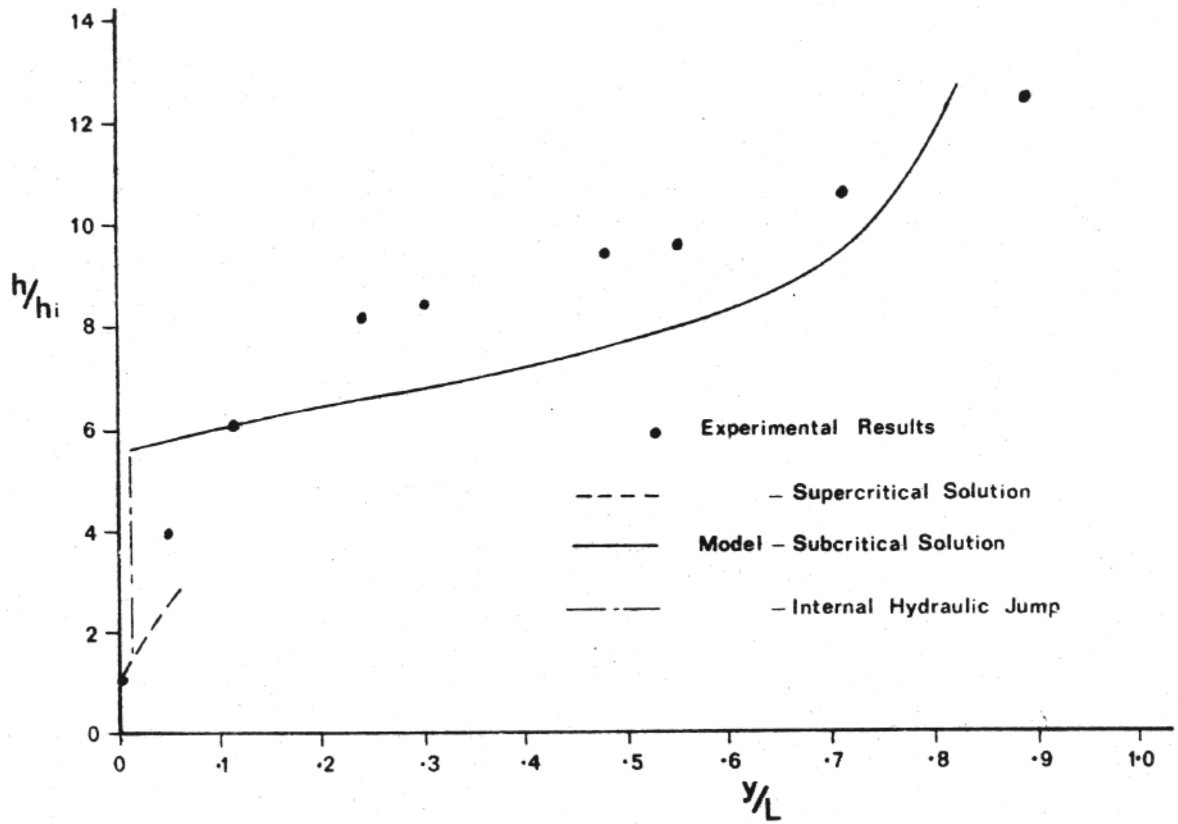

Figure 7.9 Dimensionless interfacial depth versus the dimensionless distance from the inlet. Comparison between the experimental results and the surface buoyant jet solution for Test 14. Solution parameters $e = (8.35F + 13) \times 10^{-3}$, $\theta_\infty = -3.05$, $k = 5.33 \times 10^{-5}$ m/sec, Re = 1085, Fi = 4.2 and ε given by equation 7.25.

downstream of the jump at each solution step in the super-critical flow solution, and using the values obtained at this assumed position of the jump ($y = yj$) as a separate starting condition for the sub-critical flow solution. The process was repeated until the condition $F > 1$ for $yj > y > L$ was just satisfied. The distribution of F, θ and h obtained are shown in Figures 7.7, 7.8 and 7.9 respectively.

The model considered the internal hydraulic jump to be an abrupt discontinuity in v, h and F whereas the experiments showed the transition to occur over a finite distance ($\Delta y \simeq 0.2L$). Consequently, more fluid was entrained than was indicated by the theoretical solution. Hence, the theoretical results show a higher temperature and a smaller interfacial depth downstream of the jump.

The general forms of the theoretically-derived parameters downstream of the jump are similar to those obtained in the experiments, up to the point where the end wall and the underlying flow became the dominant controls. With the inclusion of an adequate model of the internal hydraulic jump it is believed that the mathematical model would show good quantitative agreement with the experimental results.

8. CONCLUSIONS:

The inclusion of the heat transfer from the surface of the cooling pond enabled the stratified flow within the pond to be studied under steady-state operating conditions.

The numerical solution to the laminar equations of motion, presented in Chapter 4, showed that a primary eddy was formed under the surface flow and a secondary eddy, rotating in the opposite direction, formed in the bottom corner under the inlet as shown in Figure 4.2. The solutions obtained for higher Reynolds Numbers showed that part of the primary eddy, which separated the secondary eddy from the surface flow, became isolated and formed a third eddy, as shown in Figure 4.3. The existence of the primary and secondary eddies was confirmed by the experimental investigation although, due to the influence of the side walls, the strength of these eddies was not as great as that predicted by the theory. In the experiments, part of the reverse flow (backflow) in the primary eddy replenished the fluid entrained into the surface layer. The entrainment of fluid from a denser fluid to a less dense fluid is a turbulent flow phenomena and hence would not be represented by the laminar equations of motion solved in the theoretical investigation. The third eddy, predicted by the numerical solution, was diminished in the experiments by entrainment into the surface layer and only appeared intermittently. This fluctuation is thought to be the origin of the unsteadiness in the flow below the interface which was observed in the experiments.

The surface flow in the experimental investigation was turbulent, the turbulence being influenced by the convective motion superimposed on the flow by the relatively large temperature gradient which was imposed at the surface to achieve a significant heat transfer in the laboratory scaled experiments. This resulted in the mean horizontal velocity and the mean temperature tending to be uniform with depth within the surface layer. The observed entrainment coefficient was higher than the values previously reported for sub-critical flows (see Figure 6.7). The increased entrainment found in the experiments was attributed to the convective motion in the surface layer being able to penetrate into the thermal diffusion zone between the surface layer and the fluid below the interface and sharpen up the interface, a phenomena which could be absent at the lower heat transfer rates normally associated with full scale cooling ponds.

The mathematical model proposed by Koh and Fan, when modified to account for the finite length of the cooling pond, showed good agreement with the experimental results in the vicinity of the inlet when the inlet was inundated. For the condition where an internal hydraulic jump occurs downstream of the inlet, the model assumes that the transition from super-critical to sub-critical flow occurs as a discontinuity in the solution whereas the experimental results showed this transition to occur over a finite distance. The entrainment of ambient fluid within the region over which the internal hydraulic jump occurs is consequently under-estimated. This discrepancy results in an under-estimate of the downstream depth and an over-estimate of the downstream temperature. Wilkinson(23) found, in his experiments with no heat transfer away from the surface, that the entrainment in this roller region was negligible and hence it could be assumed that Koh and Fan's representation of the region might be more appropriate for conditions where the rate of heat transfer away from the surface was lower. The experimental results indicate that the internal hydraulic jump imposes its own disturbance on the flow downstream of the jump resulting in a higher rate of entrainment of ambient fluid in the sub-critical flow region (see Test 14, Figure 6.7).

The interfacial depth, and hence the Densimetric Froude Number, given by the modified mathematical model of the surface buoyant jet, deviated from the experimental results as the flow approached the downstream boundary of the cooling pond. Examination of the mathematical model showed that for the interfacial depth to remaim bounded in this region, as indicated by the experimental results, the resistance to the flow must become greater than that which could be attributed to the boundary shear stress. The deviation between the two results is attributed to the pressure field set up by the downstream boundary and the underlying flow becoming the dominant control on the flow in this region, an effect not accounted for by the mathematical model.

The accuracy of the experimental measurements were not sufficient to confidently characterise the surface flow parameters near the downstream boundary of the cooling pond. However, the analysis of Koh and Fan's mathematical model (Chapter 7) has indicated that the existance of an internal hydraulic jump and the position and flow conditions just downstream of that jump (or alternatively the flow conditions at an inundated inlet) are governed by the requirement that the Densimetric Froude Number in the downstream sub-critical flow region is always less than unity.

8.1 Suggested Fields for Further Research

The experimental apparatus proved successful in studying the two-dimensional cooling pond problem although the width of the flume used was not sufficient to justify the two-dimensional assumption in the flow below the interface.

Future investigations could be directed towards -

(a) determination of the influence of the heat transfer mechanism on entrainment of ambient fluid into the surface layer;

(b) determination of the influence of the depth of the cooling pond on the surface flow;

(c) development of a suitable model of the internal hydraulic jump for inclusion in Koh and Fan's model;

(d) determination of the influence of downstream boundaries and the underlying flow on the critical Densimetric Froude Number;

(e) determination of the influence of the internal hydraulic jump on the entrainment of ambient fluid downstream of the jump;

(f) study of the time transient behaviour of cooling ponds;

(g) extension of the study to three dimensions.

BIBLIOGRAPHY:

1. G. Abraham and W.D. Eysink — Magnitude of Interfacial Shear in Exchange Flow. Jour. of Hydraulic Research, 9 (1971), No. 2, pp. 125-151.

2. G.L. Bata — Frictional Resistance at the Interface of Density Currents. I.A.H.R., 8th Congress, Montreal (1959). Proc. Vol. 2, pp. 12-C-1, 16.

3. A. Cabelli — A Numerical Study of the Bernard Cell. Ph.D. Thesis, University of New South Wales (1970).

4. B. Carnahan, H.A. Luther and J.O. Wilks — Numerical Methods. Wiley & Sons Inc. (1969).

5. R. Dornhelm, M. Novel and R. Wiegel — Velocity and Temperature in a Buoyant Surface Jet, Report No. HEL 23-3, University of California, Berkely (July, 1970).

6. W.R. Ellis, R.A. Fookes, M.E. Gardner, J.A. Hope, N. Lamb, P. Van Louwersen and J.S. Watt — The Use of a Radio-active Tracer (Iodine 131) in the Investigation of a Power Station Cooling Pond at Maitland, N.S.W. Report No. AAEC/E.8 (1958) and AAEC/E.51. Australian Atomic Energy Commission, Reaearch Establishment, Lucas Heights, Sydney.

7. T.H. Ellison and J.S. Turner — Turbulent Entrainment in Stratified Flows. Jour. of Fluid Mech., Vol. 6, Part 3 (October, 1959), pp. 423-448.

8. T.R. Fietz — The Measurement of Characteristics of a Three-Dimensional Density Current. Report No. 85, Water Research Laboratory, University of New South Wales.

9. D.R.F. Harleman — Mechanics of Condensor Water Discharge from Thermal Power Plants. Chapter 5, Engineering Aspects of Thermal Pollution, F.L. Parker and P.A. Krenkel (Ed.) Vandenbilt Uni. Press (1968).

10. A.T. Ippen and D.R.F. Harleman — Steady State Characteristics of Subsurface Flows. Nat. Bureau of Standards (U.S.), Circular 521 (1952), pp. 79-93.

11. B.S. Jenkins — Density Currents and Turbidity Currents in Waste Disposal in the Ocean. Report No. 119, University of New South Wales (1970).

12A. G.H. Keulegan — Laminar Flow at the Inteface of Two Liquids. Nat. Bureau of Standards (U.S.), Jour. of Research, Vol. 32 (June, 1944), pp. 303-327.

12B. G.H. Keulegan — Interfacial Instability and Mixing in Stratified Flows. Nat. Bureau of Standards (U.S.), Jour. of Research, Vol. 43 (November, 1949), pp. 487-500.

13. R.C.Y. Koh and Loh-Nien Fan — Mathematical Models for the Prediction of Temperature Distributions Resulting from the Discharge of Heated Water into Large Bodies of Water. Water Pollution Control Research Series, U.S. Environmental Protection Agency, Report No. 16130 DWO (1970).

14. G.H. Lean and A.F. Whillock — The Behaviour of a Warm Water Layer Flowing Over Still Water. I.A.H.R., 11th Congress, Leningrad (1965). Proc. Vol. 2, Paper 2.9.

15. K. Lofquist — Flow and Stress Near an Interface Between Stratified Fluids. The Physics of Fluids, Vol. 3, No. 2 (March-April, 1960), pp. 158-175.

16. G.D. Mallinson and G. de Vahl Davis — The Method of the False Transient: Application to Fluid Mechanics. Aeronautical Research Laboratories, Melbourne, Report No. 331 (1971).

17. G.D. Mallinson and G. de Vahl Davis — The Method of the False Transient for the Solution of Coupled Elliptic Equations. Jour. of Computational Physics (to be published).

17A. G.D. Mallinson — Ph.D. Thesis, University of New South Wales, 1973.

18. H. Schlichting — Boundary Layer Theory, McGraw Hill (1960).

19. I.A. Sherenkov, A.D. Netjukhailo and E.D. Telezhkin — Research Investigation of Transfer Processes in Two-Dimensional Stratified Flow. I.A.H.R., 14th Congress, Paris (1971). Proc. Vol. 1, Paper A-26.

20. K.D. Stolzenbach and D.F.R. Harleman — An Analytical and Experimental Investigation of Surface Discharges of Heated Water. Report No. 135, Ralph M. Parsons Laboratory for Water Resources and Hydrodynamics, Massachusetts Institute of Technology (1971).

21. D.M. Thompson — Hazelwood Power Station: Data Collection and Analysis of Cooling Pond Performance. Proc. 4th Australasian Conference on Hydraulics and Fluid Mechanics (1971).

22. J.S. Turner — The Influence of Molecular Diffusivity on Turbulent Entrainment across a Density Interface. Jour. of Fluid Mechanics, Vol. 32, Part 4 (1968), pp. 639-656.

23. D.L. Wilkinson — Studies in Density Stratified Flows, Report No. 118, Water Research Laboratory, University of New South Wales (1970).

24. B. Ackland, J. Brown and G. Howell — Communique. Instrumentation Group. Herman Central Scientific Laboratory. State Electricity Commission of Victoria.

APPENDIX A

FINITE DIFFERENCE APPROXIMATIONS TO GOVERNING EQUATIONS

The finite difference approximations to the false transient equations in Section 3.2 using the notation of Figure 3.1, are -

(a) The vorticity equation

$$\frac{1}{\alpha_\zeta}\frac{\partial\zeta}{\partial t} = \frac{X_i^1}{\Delta X^2}\Big[X^1_{i+\frac{1}{2}}\,(\zeta_{i+1,j} - \zeta_{i,j})$$

$$- X^1_{i-\frac{1}{2}}\,(\zeta_{i,j} - \zeta_{i-1,j})\Big]$$

$$+ \frac{Y_j^1}{\Delta Y^2}\Big[Y^1_{j+\frac{1}{2}}\,(\zeta_{i,j+1} - \zeta_{i,j})$$

$$- Y_{j-\frac{1}{2}}\,(\zeta_{i,j} - \zeta_{i,j-1})\Big]$$

$$+ \frac{Re}{Fi^2}\left[\frac{Y_j^1}{2\Delta X}\,(\theta_{i,j+1} - \theta_{i,j-1})\right]$$

$$- Re\Big[\frac{X_i^1}{2\Delta X}\,(u_{i+1,j}\zeta_{i+1,j} - u_{i-1,j}\zeta_{i-1,j})$$

$$+ \frac{Y^1}{2\Delta Y}\,(v_{i,j+1}\zeta_{i,j+1} - v_{i,j-1}\zeta_{i,j-1})\Big]$$

(b) The energy equation

$$\frac{1}{\alpha_\theta}\frac{\partial\theta}{\partial t} = \frac{X_i^1}{\Delta X^2}\left[X^1_{i+\frac{1}{2}}\,(\theta_{i+1,j} - \theta_{i,j}) - X^1_{i-\frac{1}{2}}\,(\theta_{i,j} - \theta_{i-1,j})\right]$$

$$+ \frac{Y_j^1}{\Delta Y^2}\left[Y^1_{j+\frac{1}{2}}\,(\theta_{i,j+1} - \theta_{i,j}) - Y^1_{j-\frac{1}{2}}\,(\theta_{i,j} - \theta_{i,j-1})\right]$$

$$- \mathrm{RePr}\left[\frac{X_i^1}{2\Delta X}\left(u_{i+1,j}\theta_{i+1,j} - u_{i-1,j}\theta_{i-1,j}\right)\right.$$

$$\left. + \frac{Y_j^1}{2\Delta Y}\left(v_{i,j+1}\theta_{i,j+1} - v_{i,j-1}\theta_{i,j-1}\right)\right]$$

(c) The streamfunction equation

$$\frac{1}{\alpha_\psi}\frac{\partial\psi}{\partial t} = \zeta_{i,j} + \frac{X_i^1}{\Delta X^2}\left[X_{i+\frac{1}{2}}^1\left(\psi_{i+1,j} - \psi_{i,j}\right) - X_{i-\frac{1}{2}}^1\left(\psi_{i,j} - \psi_{i-1,j}\right)\right]$$

where $X^1 = \frac{\partial X}{\partial x}$ and $Y^1 = \frac{\partial Y}{\partial y}$

APPENDIX B

FINITE DIFFERENCE APPROXIMATIONS TO THE DERIVATIVE BOUNDARY CONDITIONS

The finite difference approximations to the derivative boundary conditions given in Table 2.1, using the notation of Figure 3.1, are -

(a) For the free surface $x = 0$, $0 < y < L$

$$\theta_{1,j} = \frac{1}{(r^2-1) + \frac{Nu}{L} k(r-1)} \left[r^2 \theta_{2,j} - \theta_{3,j} \right]$$

$$v_{1,j} = \frac{-1}{k(r^2-1)} \left[r^3 \psi_{2,j} - \psi_{3,j} \right]$$

where $k = x_3 - x_1$ and $r = \dfrac{x_3 - x_1}{x_2 - x_1}$

(b) For the vertical boundary $1 < x < D$, $y = 0$

$$\theta_{i,1} = \frac{1}{r^2-1} \left[r^2 \theta_{i,2} - \theta_{i,3} \right]$$

$$\zeta_{i,1} = \frac{-2}{k^2(r-1)} \left[r^3 \psi_{i,2} - \psi_{i,3} + (r^3 - 1) \right]$$

where $k = y_3 - y_1$ and $r = \dfrac{y_3 - y_1}{y_2 - y_1}$

(c) For the bottom boundary $x = D$, $0 < y < L$

$$\theta_{M,j} = \frac{1}{(r^2-1)} \left[r^2 \theta_{M-1,j} - \theta_{M-2,j} \right]$$

$$\zeta_{M,j} = \frac{-2}{k^2(r-1)}\left[r^3\psi_{M-1,j} - \psi_{M-2,j} + (r^3-1)\right]$$

where $k = x_{M-2} - x_M$ and $r = \dfrac{x_{M-2} - x_M}{x_{M-1} - x_M}$

(d) And for the vertical boundary at $y = L$

$$\theta_{i,N} = \frac{1}{(r^2-1)}\left[r^2\theta_{i,N-2} - \theta_{N-2}\right]$$

for $0 < x < D$

$$\zeta_{i,N} = \frac{-2}{k^2(r-1)}\left[r^3\psi_{i,N-1} - \psi_{i,N-2}\right]$$

for $0 < x < (D\text{-}Ho)$

where $k = y_{N-2} - y_N$ and $r = \dfrac{y_{N-2} - y_N}{y_{N-1} - y_N}$

APPENDIX C

CALCULATION OF ENTRAINMENT VOLUME INTO THE SURFACE LAYER IN THE VICINITY OF THE INTERNAL HYDRAULIC JUMP OF TEST 14

Consider a control volume bounded by the interface, the top surface and two consecutive measuring stations at y1 and y2 as shown in Figure C1. T1 and T2 are the temperatures of the surface flow into and out of the control volume, To is the temperature of the fluid below the interface, M1 is the surface mass flow into the control volume, Me is the entrainment mass flow across the interface and q is the rate of heat flow from the surface.

Assuming that heat is only convected across the boundaries a-b, b-c and c-d and is conducted across d-a, a heat balance on the control volume gives

$$M1CpT1 + MeCpTo = (M1+Me)\ CpT2 + q \qquad (C1)$$

where Cp is the specific heat of the fluid.

As Me approaches zero, q is given by

$$q = M1Cp\ (T1-T2).$$

An approximation to q can be obtained by using the temperature gradient downstream of the internal hydraulic jump, where Me $\rightarrow$ 0, to find an equivalent temperature drop due to heat transfer ΔTeq. The heat transfer rate from the control volume is given by

$$q = (M1 + \frac{Me}{2})\ Cp\Delta Teq \qquad (C2)$$

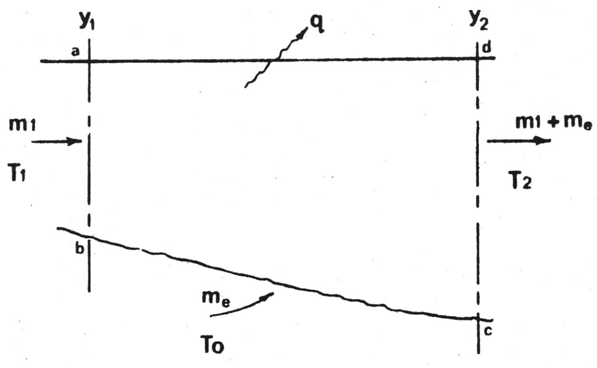

<u>Figure C1</u> Definition sketch.

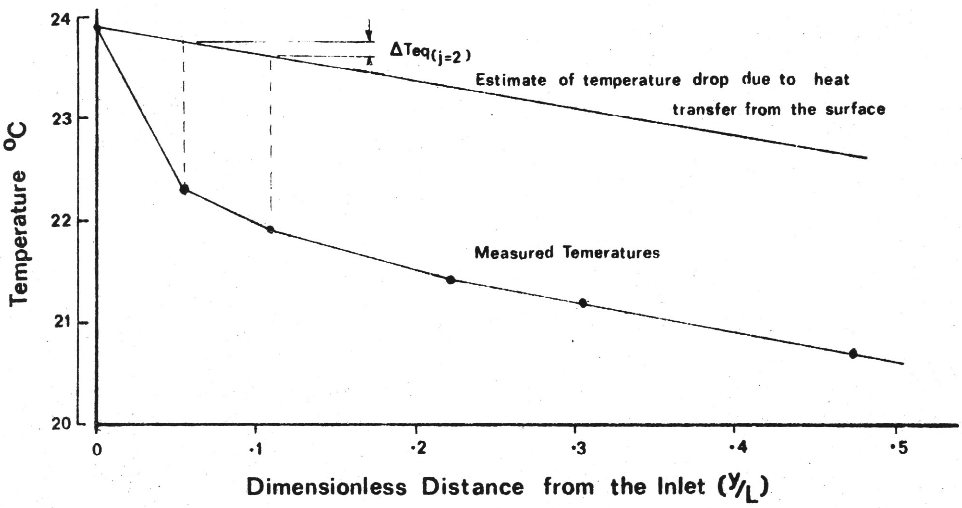

<u>Figure C2</u> Temperature versus dimensionless distance from the inlet in the region of the internal hydraulic jump for Test 14.

and hence the entrainment rate is

$$\frac{Me}{M1} = \frac{T1-T2-\Delta Teq}{T2-To+\frac{\Delta Teq}{2}} \tag{C3}$$

Under the approximations made, Equation (C3) is only valid in the region where the temperature drop in the surface layer due to entrainment is large compared to that due to heat transfer.

The mass flow at the jth measuring station is given from Equation (C3) as

$$M_j = M_{j-1}\left[1 + \left(\frac{T_{j-1}-T_j-\Delta Teq_j}{T_j-To+\Delta Teq_j/2}\right)\right] \tag{C4}$$

Equation (C4) has been used to estimate the mass flow rate in the region of the internal hydraulic jump from the known temperature distribution, shown in Figure C2, for Test 14.

APPENDIX D

EXPERIMENTAL RESULTS

Notation

Vh	flow per unit width (mm^2/sec).
h	interfacial depth (mm).
T	temperature ($^{\circ}C$).
y/l	non-dimensional distance from the inlet.
F	Densimetric Froude Number $\left(\dfrac{Vh}{\sqrt{g \frac{\Delta\rho}{\rho} h^3}} \right)$
l	length of test section (m).

Subscripts

i	inlet.
s	shear flow.
b	back flow.
o	outlet.
cw	cooling water.
	surface flow.

Notes

1. Flow rates were not measured at all measuring stations in some tests.
2. The shear flow and back flow were calculated from the centre line velocity profiles.
3. Results presented are the average from a number of measurements.

Test 10

F_i = 0.72

Vh_i = 677 mm^2/sec

h_i = 36.1 mm

T_i = 25.55°C

l = 5.5 m

T_o = 16.67°C

T_{cwi} = 3.89°C

T_{cwo} = 4.5°C

Inlet inundated

y/l	h	T	Vh	F	Vh_s	Vh_b
0.055	67.1	24.6	748	0.335	-	-
0.112	69.1	23.75	751	0.349	149	156
0.224	65.2	22.45	-	-	-	-
0.306	72.6	21.8	855	0.447	450	432
0.472	73.6	20.1	922	0.575	445	445
0.546	77.5	19.3	-	-	-	-
0.722	83.8	18.4	105	0.761	739	710
0.89	109.0	17.5	109	0.787	356	1020

Test 11

$F_i = 0.87$

$Vh_i = 883\ mm^2/sec$

$h_i = 40.6\ mm$

$T_i = 25.55^oC$

$l = 5.5\ m$

$T_o = 18.11^oC$

$T_{cwi} = 2.5^oC$

$T_{cwo} = 3.4^oC$

Inlet inundated

y/l	h	T	Vh	F	Vh_s	Vh_b
0.055	76.5	25.17	968	0.37	-	-
0.112	82.8	24.61	981	0.35	440	210
0.224	85.1	23.16	-	-	-	-
0.306	86.0	22.56	1013	0.42	342	405
0.472	87.4	21.06	1135	0.57	420	323
0.722	101.6	19.67	1158	0.65	410	366
0.89	116.8	18.5	1345	1.2	755	397

Test 12

$F_i = 1.2$

$Vh_i = 1080 \text{ mm}^2/\text{sec}$

$h_i = 40.6$ mm

$T_i = 24.56^\circ C$

$l = 5.5$ m

$T_o = 19.0^\circ C$

$T_{cwi} = 5.16^\circ C$

$T_{cwo} = 5.72^\circ C$

Inlet inundated

y/l	h	T	Vh	F	Vh_s	Vh_b
0.055	86.9	24.22	1200	0.44	193	116
0.112	91.0	23.56	1226	0.454	310	235
0.224	97.5	22.67	-	-	-	-
0.306	103.4	22.1	1265	0.476	217	237
0.472	107.0	21.1	1340	0.59	219	245
0.546	117.6	20.67	-	-	-	-
0.722	122.2	20.17	1523	0.75	452	606
0.89	132.0	19.6	1640	0.995	342	423

Test 13

$F_i = 2.88$

$Vh_i = 1065\ mm^2/sec$

$h_i = 22.9\ mm$

$T_i = 24.17^oC$

$l = 5.5\ m$

$T_o = 18.5^oC$

$T_{cwi} = 3.8^oC$

$T_{cwo} = 4.76^oC$

Internal hydraulic jump formed

y/l	h	T	Vh	F	Vh_s	Vh_b
0.055	64.6	23.72	1232	0.51	90	116
0.112	98.0	23.22	1284	0.423	270	268
0.224	104.0	22.22	-	-	-	-
0.306	108.5	21.56	1322	0.47	348	413
0.472	112.3	20.67	1484	0.59	297	512
0.722	126.5	19.56	1658	0.81	161	343
0.89	151.4	18.78	1768	1.36	-	-

Test 14

$F_i = 4.25$

$Vh_i = 1000\ mm^2/sec$

$h_i = 17.5\ mm$

$T_i = 23.9^\circ C$

$l = 5.5\ m$

$T_o = 19.1^\circ C$

$T_{cwi} = 4.17^\circ C$

$T_{cwo} = 4.94^\circ C$

Internal hydraulic jump formed

y/l	h	T	Vh	F	Vh_s	Vh_b
0.055	69.0	22.3	1450*	1.0	0	710
0.112	105.2	21.9	1535*	0.60	99	604
0.224	142.2	21.4	1652*	0.45	0	687
0.306	147.2	21.2	1755	0.485	92	672
0.472	165.4	20.67	2040	0.54	74	738
0.546	167.0	20.22	-	-	-	-
0.722	186.0	19.9	2160	0.70	13	1568
0.89	200.6	19.5	2612	1.04	57	1130

* - Calculated from heat balance.

Test 15

$F_i = 1.07$

$Vh_i = 735\ mm^2/sec$

$h_i = 31.1\ mm$

$T_i = 22.94^oC$

$l = 5.5\ m$

$T_o = 17.67^oC$

$T_{cwi} = 4.0^oC$

$T_{cwo} = 5.0^oC$

Inlet inundated

y/l	h	T	Vh	F	Vh_s	Vh_b
0.055	74.4	24.03	824	0.346	238	81
0.112	76.2	23.52	852	0.358	280	192
0.224	81.0	22.28	884	0.398	316	355
0.306	81.3	21.72	929	0.447	230	212
0.472	87.1	20.44	929	0.492	433	336
0.546	94.0	19.81	-	-	-	-
0.722	100.2	18.9	1226	0.796	439	482
0.89	129.8	18.07	1490	1.21	335	626

Test 16

$F_i = 0.73$

$Vh_i = 275\ mm^2/sec$

$h_i = 64.5\ mm$

$T_i = 21.0^oC$

$l = 0.95\ m$

$T_o = 18.1^oC$

$T_{cw} = 4.3^oC$

Inlet inundated

y/l	h	T	Vh	F
0.32	48.3	20.17	387	0.55
0.64	56.9	19.22	529	0.73

Test 17

$F_i = 1.1$

$Vh_i = 177\ mm^2/sec$

$h_i = 13.6\ mm$

$T_i = 22.5^{\circ}C$

$l = 0.95\ m$

$T_o = 18.1^{\circ}C$

$T_{cw} = 4.3^{\circ}C$

Inlet inundated

y/l	h	T	Vh	F
0.32	31.7	20.33	245	0.56
0.64	42.7	18.6	323	0.74